Universal scaling of elliptic and hexadecapole flow in Au+Au collisions at $\sqrt{s_{NN}} = 200$ GeV

A. Taranenko, Roy A. Lacey,

Chemistry Dept.
Stony Brook University,
Stony Brook, NY 11794-3400

Abstract

This note reports differential measurements for the even order flow coefficients $v_n, n = 2, 4$, for unidentified charged hadrons and several identified particle species in Au+Au collisions at $\sqrt{s_{NN}} = 200\,\text{GeV}$. The measurements are then used to (i) test the scaling predictions of both the hydrodynamic and recombination models and (ii) investigate the relationship between the even order flow coefficients for quarks (v_4^q and v_2^q), derived from the scaled coefficients for hadrons. We find evidence for robust universal scaling of v_n which gives further evidence for thermalization and transverse expansion dynamics compatible with the creation of a strongly coupled quark gluon plasma.

Contents

1 Introduction **2**

2 Data set, QA and general cuts **2**
2.1 Run selection 2
2.2 Event and track selection 3

3 Data Analysis **5**
3.1 CVS location of the codes and macros 5
3.2 Procedure 5
3.2.1 Reaction plane QA 5
3.2.2 Dispersion corrections for the reaction planes 12

4 Particle Identification in ToF East/West **18**
4.1 Fine tuning of the timing calibration for ToF East/West 18
4.2 Beam Shift and Momentum Scale Calibration 23
4.3 PID Functions 24

5 Results **29**
5.1 Elliptic flow of charged hadrons 29
5.2 Elliptic flow of identified charged hadrons 34
5.3 v_4 vs p_T of identified charged hadrons 35
5.4 v_4 vs KE_T of identified charged hadrons 35
5.5 Systematic Errors 39

6 Plots requested for Preliminary **41**

7 Elliptic flow of identified charged hadrons TOF/EMC **44**

8 Detailed check of PID functions **52**

1 Introduction

At RHIC energies, momentum anisotropy is believed to result from particle interactions [in the QGP] which drive pressure gradients in an initial "almond-shaped" collision zone, produced in non-central collisions. When these interactions are frequent enough, the collision zone is expected to achieve local equilibrium leading to hydrodynamically driven flow [**?**, **?**, **?**]. A central question of great current interest is the extent to which the QGP is thermalized and whether or not it is strongly coupled.

Anisotropic flow measurements provide an invaluable "tool" for validation tests of hydrodynamic behavior and hence, a link to the degree of thermalization and the strength of the coupling in the QGP. This is because the universal character of hydrodynamic flow leads to specific scaling predictions for the even order harmonic coefficients. Needless to say, local equilibrium is not a necessary condition for azimuthal anisotropy. However, incomplete equilibration breaks the scale invariance of hydrodynamics and this leads to deviations from the scaling predictions.

In earlier work, we have made initial tests which validate the predictions from perfect fluid hydrodynamics [**?**, **?**] for the scaling of the elliptic flow coefficient v_2 with eccentricity ϵ, system size and transverse kinetic energy $KE_T \equiv m_T - m$ (m_T is the transverse mass) [**?**, **?**, **?**]. A universal scaling of $v_2(KE_T)/n_q$, suggestive of quark-related degrees of freedom in the flowing medium, was also deomonstrated for a broad range of particle species [**?**, **?**, **?**].

The current analysis extends our earlier work via:

- detailed differential hexadecapole (v_4) and elliptic (v_2) measurements for unidentified charged hadrons and several identified particle species;
- detailed tests of the scaling predictions of both the hydrodynamic and recombination models and
- an investigation of the relationship between the even order flow coefficients for quarks v_4^q and v_2^q, obtained from the scaled coefficients for hadrons.

2 Data set, QA and general cuts

The present analysis was performed with Run7 minimum-bias Au+Au events from the pro.77 and pro.78 CWG Nano DST's. A total of $\simeq$ 2.6 B events were used subsequent to the rejection of "bad" runs based on QA studies, and a $\pm$ 30 cm BBC Z-vertex cut.

2.1 Run selection

Full field runs were analyzed; they include both the (+-) and the (-+) field configurations. In what follows, we give a summary of the criteria for identifying "bad" runs, as well as a list of the runs so rejected;

- Zero field runs (7) : 229545, 231156, 236137, 238530, 238531, 238971, 239312

- (++) field runs (15) : 235889, 235890, 235891, 235892, 235893, 235894, 235895, 235900, 235901, 235902, 236004, 236005, 236007, 236008, 236009

- Converter runs (9) : 238682, 238683, 238684, 238698, 238843, 238845, 238846, 238847, 238848

- Bad centrality runs: for each run the the χ^2/ndf was calculated for fits to the centrality distributions with a constant (p0). Fig. 1(b) shows these χ^2/ndf as a function of run number. A large variation in χ^2/ndf as a function of run number is evident. An extensive study showed that small deviations from the expected flat distributions ($5 < \chi^2/ndf < 80$) did not affect the extracted values for v_2 and v_4, see Figs. 22 and 25. Consequently, runs with $\chi^2/ndf > 80$ were rejected. (27) : 232996, 233475, 235570, 235613, 235659, 235684, 235686, 235696, 235794, 235796, 235798, 235801, 235805, 235809, 233474, 235032, 235572, 235658, 235660, 235685, 235690, 235699, 235795, 235797, 235800, 235802, 235807

- Runs with "bad" reaction planes; these include runs with distributions which are not flat, runs with reaction plane resolution far from the average value for a given centrality: 228259; Runs with all reaction planes missing; bad mpc plane: 229790, 229793, 229794, 229796, 229799, 229800, 232377, 232378, 232379, 235656, ...

- Missing West Arm: 232377,232378, 232379

- Runs with bad timing resolution for TOF (East/West): 228341, 228405, 228407, 228408, 228477, 228640, 228832, 230935, 230937, 234175, 234202

- Runs with small average number of pions/event detected in TOF East/West: .....

- Runs with number of events < 400 k

For PID hadron v_2 and v_4 analysis, 605 runs were used. The final list of these runs, which takes account of additional detailed studies of the reaction plane (Appendix A) and PID QA for the TOF East and TOF West detectors (Appendix B), is summarized in the appendix.

2.2 Event and track selection

Event and track selection are listed below:
Event selection:

- Centrality range: 0-70%

- | bbcz | < 30 cm - BBC vertex cut (PHGlobal::getBbcZVertex())

- Use combined (BBC, MPC, RXN) south and north eventplane.

Track selection:

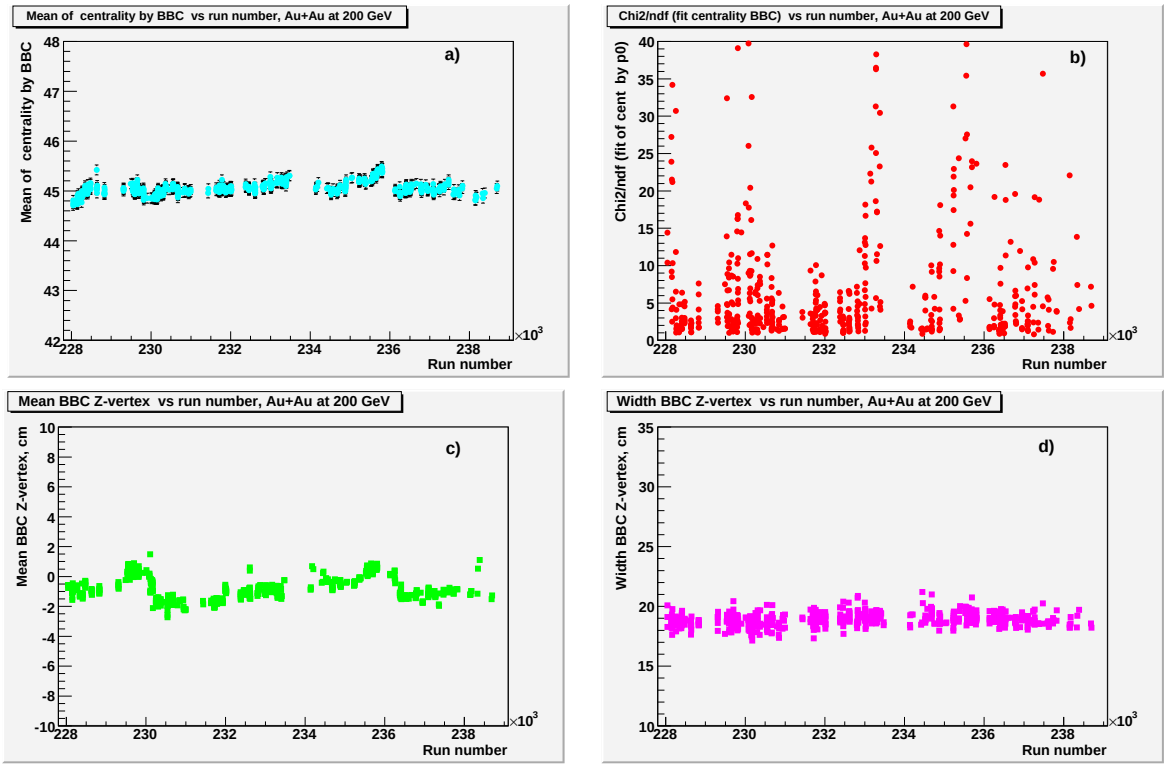


Figure 1: (a) Mean centrality obtained from the BBC distribution, as a function of run number (b) χ^2/ndf of the fit to the centrality by clock distribution as a function of run number; (c) mean value of the BBC z-vertex as a function of run number; (d) width of the BBC z-vertex as a function of run number.

- Momentum cut: 0.2-4 GeV/c
- DCH Track Quality: 31 or 63
- | zed | < 75 cm
- 2 σ "radial" matching cut on TOF + PC3
- TOF East: $etof > 0.000193 + 0.001357\beta^2$, where etof is the energy loss in the TOF East scintillator, and β = v/c = pltof/(ttof c)
- TOF West: $60 < qtof < 600$.
- 2σ PID cut for π, K, p selection (+ 3 sigma PID veto cut) in order to reduce the contamination of other particles

3 Data Analysis

3.1 CVS location of the codes and macros

The MasterRecalibrator was used to recalibrate the data. The analysis code location in CVS is:
1) CVS:/offline/AnalysisTrain/MakeEmcToFv2 *- compact picoDST's with Global, Track, TOF East and West PID information produced by Taxi 78*

3.2 Procedure

The reaction plane method of analysis of azimuthal anisotropy for different particle species, is not only straightforward, it is commonly used in many PHENIX analyses. It involves the determination of the azimuth Ψ of the reaction plane followed by the construction of an event-averaged azimuthal distribution for particles relative to it ($\phi - \Psi$). A subsequent Fourier analysis of this distribution gives the even order coefficients $v_2^{raw} = \langle cos\,[2(\phi - \Psi)]\rangle$ and $v_4^{raw} = \langle cos\,[4(\phi - \Psi)]\rangle$, which are an estimate of the raw elliptic $v_2^{raw}$and hexadecapole v_4^{raw} flow respectively. A requisite correction of this azimuthal anisotropy for reaction plane dispersion leads to an estimate of the "true" azimuthal anisotropy.

3.2.1 Reaction plane QA

In order to extract robust values of v_2 and v_4, special attention was given to detailed QA checks related to the flatness of the reaction planes (BBC, MPC and RXN) used in the analysis. Fig. 2 shows a representative example of flat reaction plane distribution; Fig. 3 shows one which is not. The flatness of the reaction plane obtained with the BBC, MPC and the RXN detectors, were carefully studied as a function of run number. Figs. 4, 5 and 6 show the anisotropic coefficients (nominal value of 0 for a flat reaction plane) as a function of run number, obtained via fits to the reaction planes; they indicate that for most runs, the reaction plane is flat. However for runs from (-+) field run group (runs $>$ 236000) the reaction planes were not fully flat by the time of analysis Taxi 78, because the reaction calibration was done only using 300 k events of each run from this group, see as an example Fig **??**. As the statistics are crutual for the present analysis we re-flat the reaction planes for runs from (-+) field run group. Fig 7 shows an example of different reaction plane distributions for a single run from (-+) field group before and after additional re-flatering.

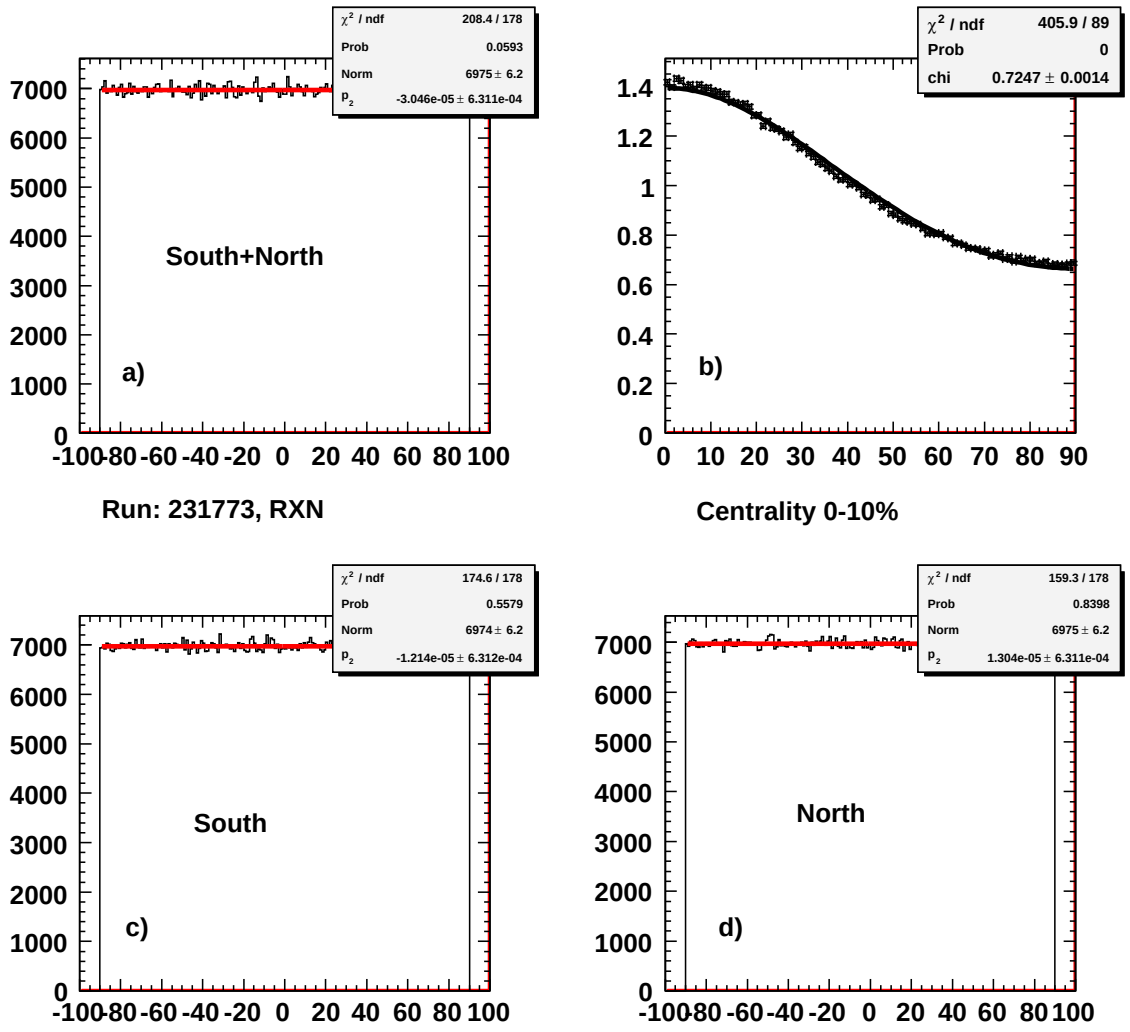


Figure 2: Representative example of a flat reaction plane obtained with the full statistics of a run. Reaction planes are shown for Sourh + North (a), South (c) and North (d). Panel (b) shows the distribution of the dispersion of the reaction plane.

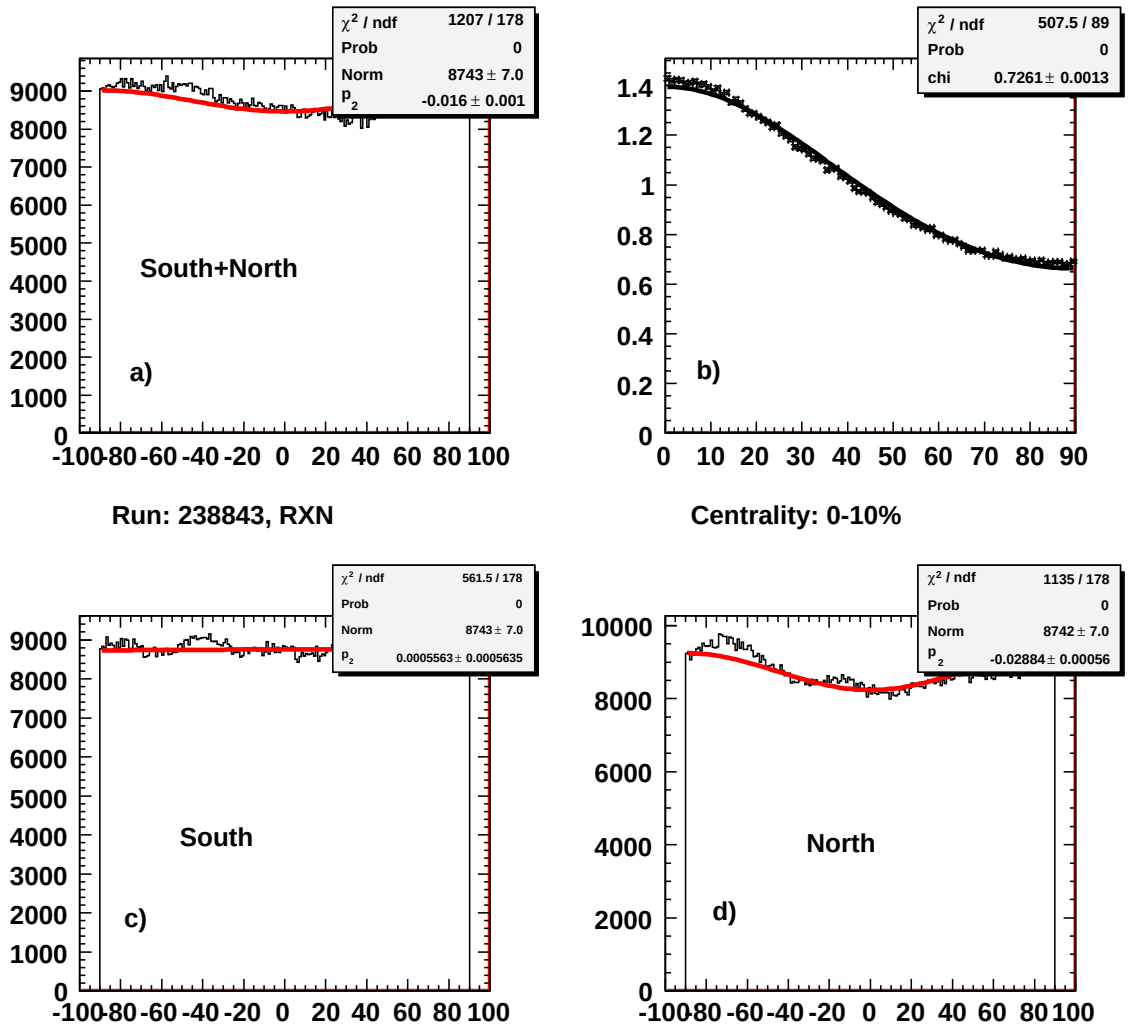


Figure 3: Representative example of a distorted reaction plane obtained with the full statistics of a run. Reaction planes are shown for Sourh+North (a), South (c) and North (d). Panel (b) shows the distribution of the dispersion of the reaction plane.

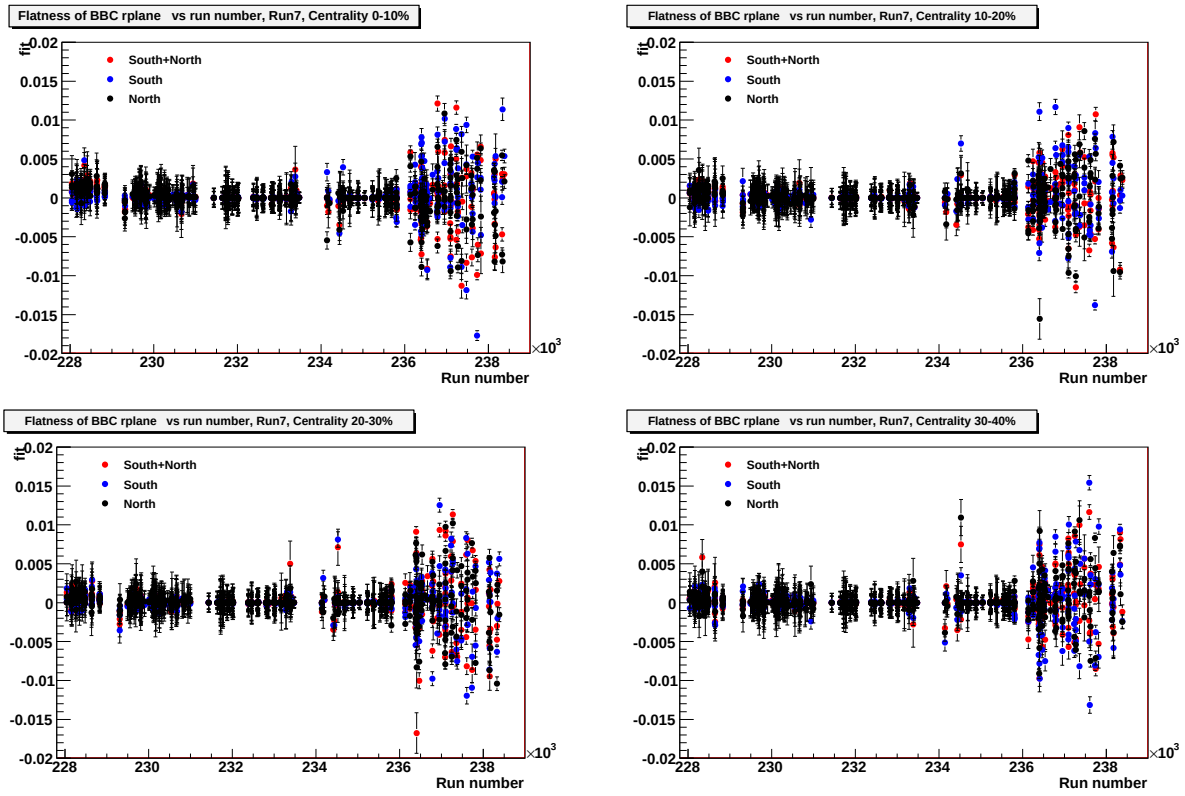


Figure 4: Anisotropic coefficient vs run number for the BBC reaction planes. Results are shown for South+North, South and North respectively, for several centrality selections as indicated.

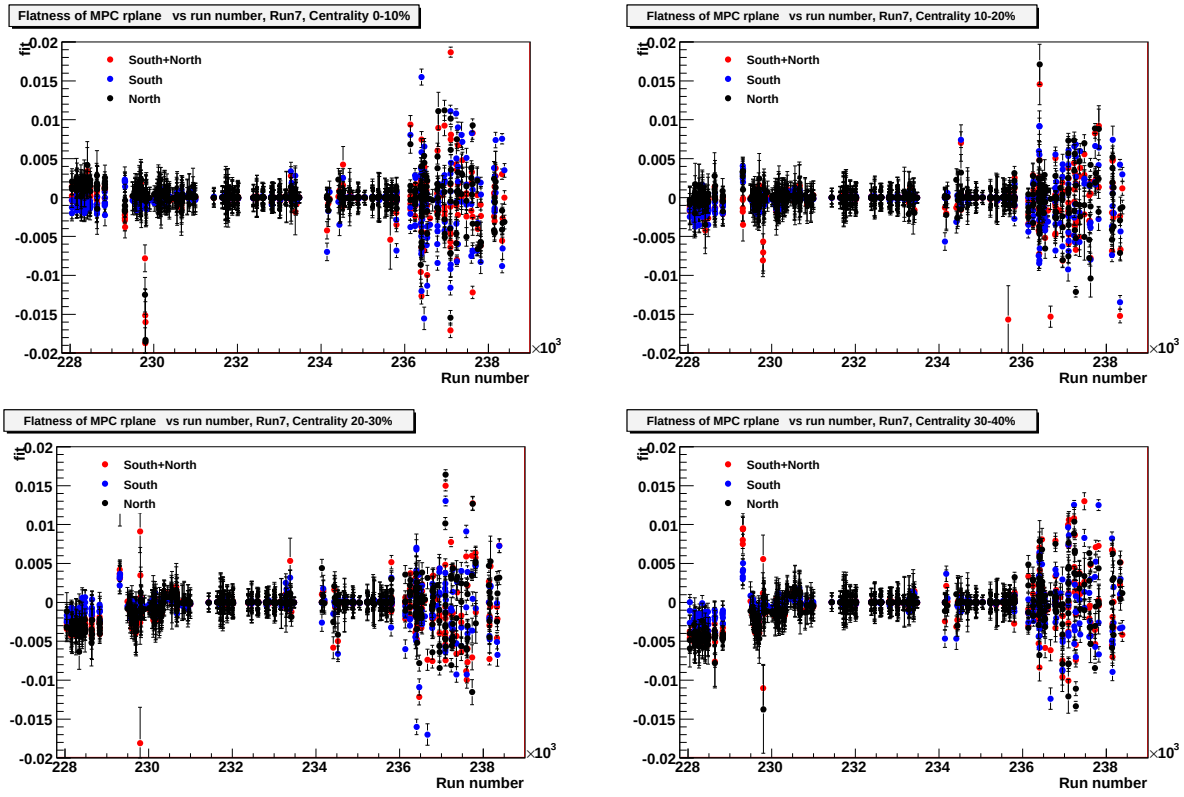


Figure 5: Anisotropic coefficient vs run number for the MPC reaction planes. Results are shown for South+North, South and North respectively, for several centrality selections as indicated.

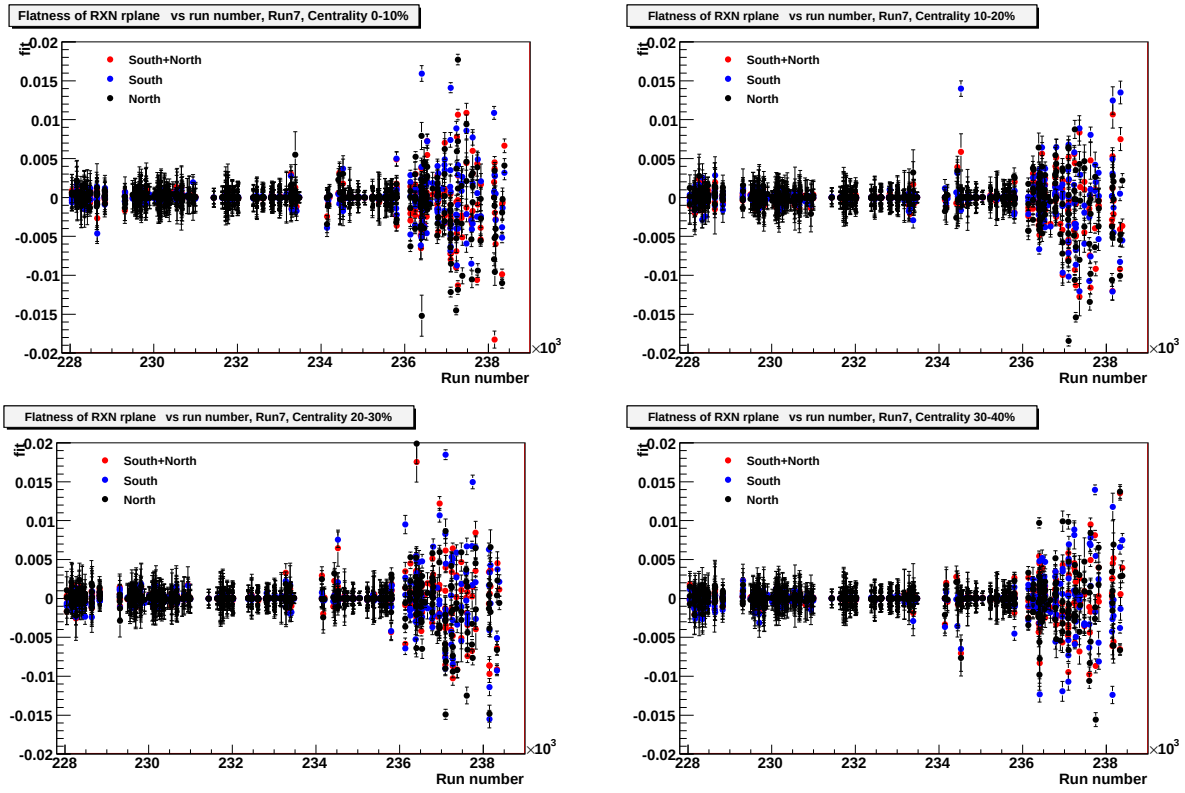


Figure 6: Anisotropic coefficient vs run number for RXN reaction planes. Results are shown for South+North, South and North respectively, for several centrality selections as indicated.

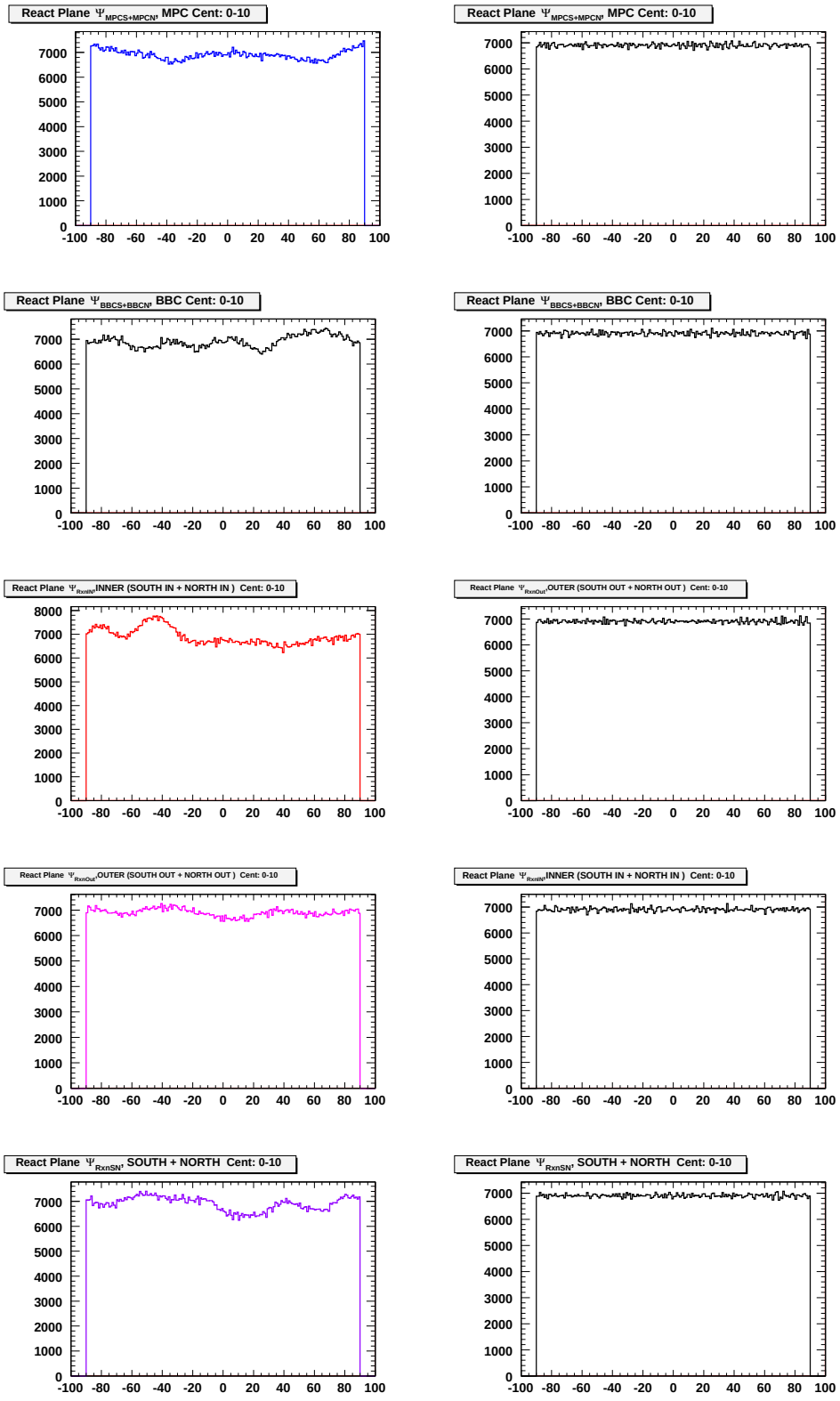


Figure 7: An example of distributions of the azimuth of the (MPC, BBC, RXN) reaction planes for a single run from (-+) field group with "old" (left panel) and new rp calibration (right panel).

3.2.2 Dispersion corrections for the reaction planes

To obtain the dispersion correction factors, a detailed study the reaction plane dispersion was also carried out following the the Ollitrault-Voloshin [**?**, **?**] fit method, the sub-event plane method. This was achieved via measurements of the distribution of the relative angle between sub-events $\Delta\phi_R = \Psi_N - \Psi_S$, where Ψ_N and Ψ_S are the azimuth of the reaction plane determined in the north and south respectively. The resolution parameter χ_I, and the corresponding dispersion factor σ_{RP}, were obtained via fits to these distributions with Eq. 1;

$$\frac{dN}{d\Delta\phi_R} = \frac{e^{-\chi_I^2}}{2}\left[\frac{2}{\pi}(1+\chi_I^2) + z(I_0(z)+L_0(z)) + \chi_I^2(I_1(z)+L_1(z))\right], \tag{1}$$

where z=$\chi_I^2 cos(\Delta\phi_R)$ and L_0 and L_1 are modified Struve functions, see [**?**] for details.

The dispersion corrections to all order n can then be calculated as follows [9]:

$$\langle\cos(n(\Psi_m - \Psi_r))\rangle = \frac{\sqrt{\pi}}{2}\chi\exp(-\chi^2/2)\left[I_{\frac{n-1}{2}}(\chi^2/2) + I_{\frac{n+1}{2}}(\chi^2/2)\right], \tag{2}$$

Three sub-event method:
Event plane resolution can be evaluated from correlations of three independent event planes (a, b, c) [**?**].

$$\langle\cos(n(\Psi_m^a - \Psi_r))\rangle = \sqrt{\frac{\langle\cos(n(\Psi_m^a - \Psi_m^b))\rangle\langle\cos(n(\Psi_m^a - \Psi_m^c))\rangle}{\langle\cos(n(\Psi_m^b - \Psi_m^c))\rangle}}. \tag{3}$$

Event plane resolution for wide centrality bins : was calculated for each particle by averaging the event plane resolution obtained in 10% centrality bins weighting with the yield of π, K and protons in each centrality. The results of this procedure is presented in the Table.1. The number of , K and protons for each centrality bin was selected by applying 2 PID cut and selecting the following momentum range: 0.25-3.0 GeV/c for π, 0.3-2.5 GeV/c for $K^{\pm}$ and 0.5-3.5 Gev/c for (anti-)protons.

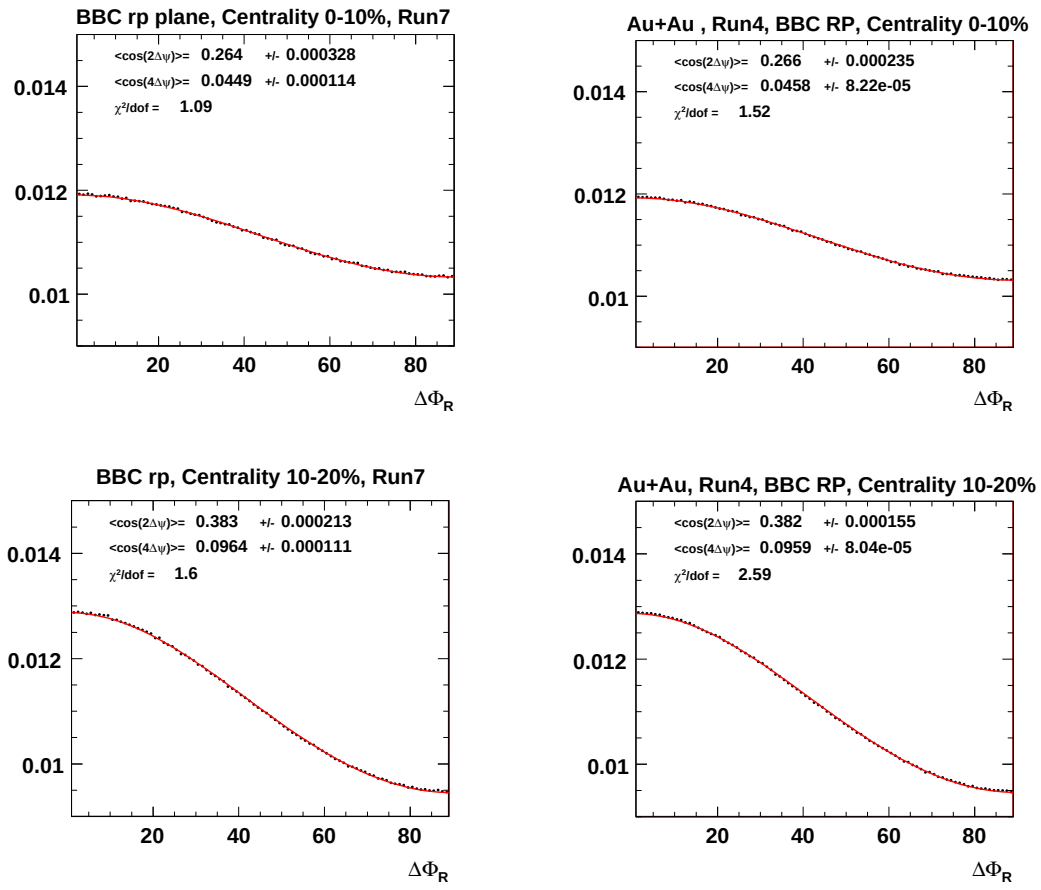


Figure 8: Estimates of the combined (S+N) BBC reaction plane resolution via the Ollitrault-Fit method for several centrality selections as indicated. The left and right panels show results from Run7 and Run4 data (Au+Au at 200 GeV) respectively.

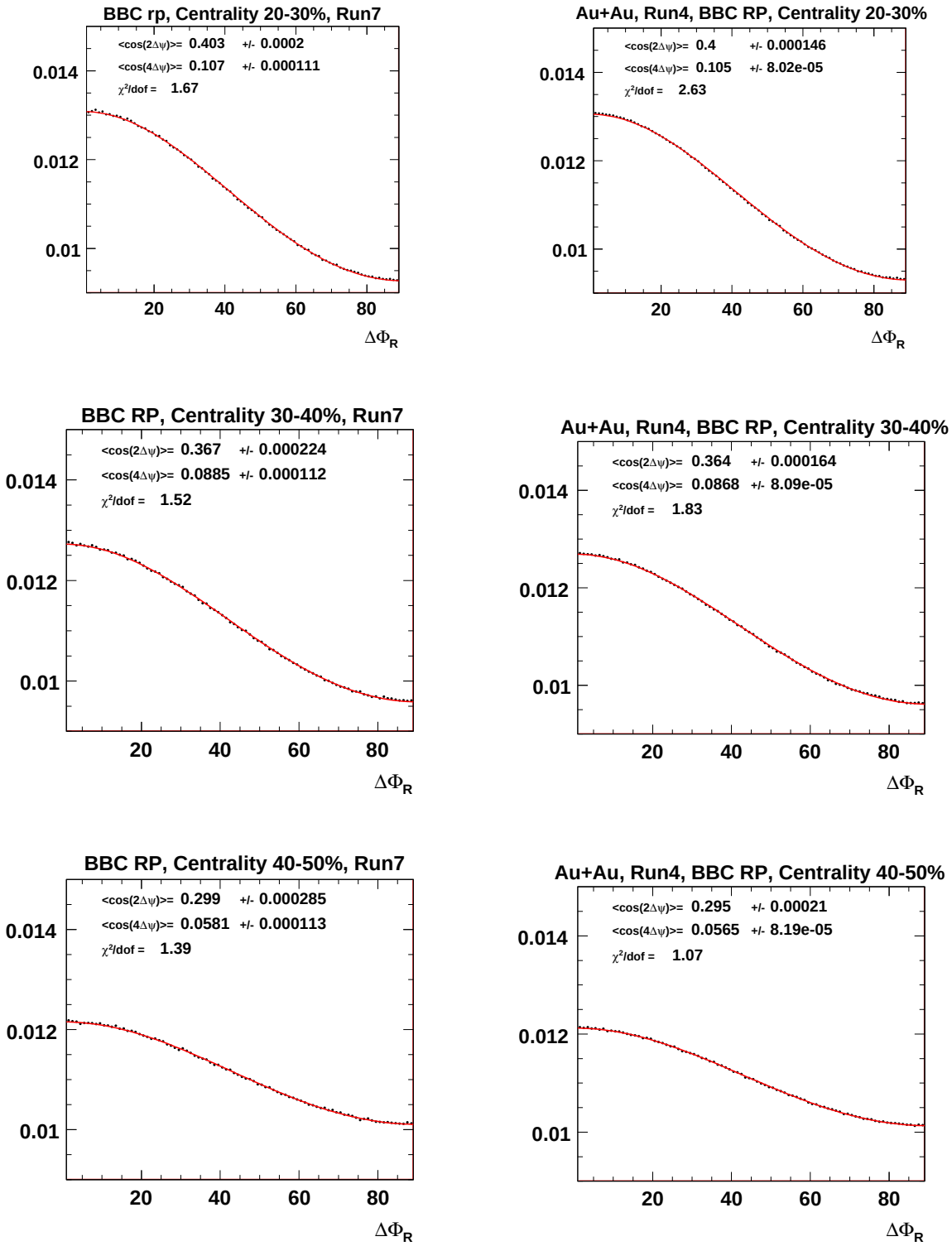


Figure 9: Estimates of the combined (S+N) BBC reaction plane resolution via the Ollitrault-Fit method for several centrality selections as indicated. The left and right panels show results from Run7 and Run4 data (Au+Au at 200 GeV) respectively.

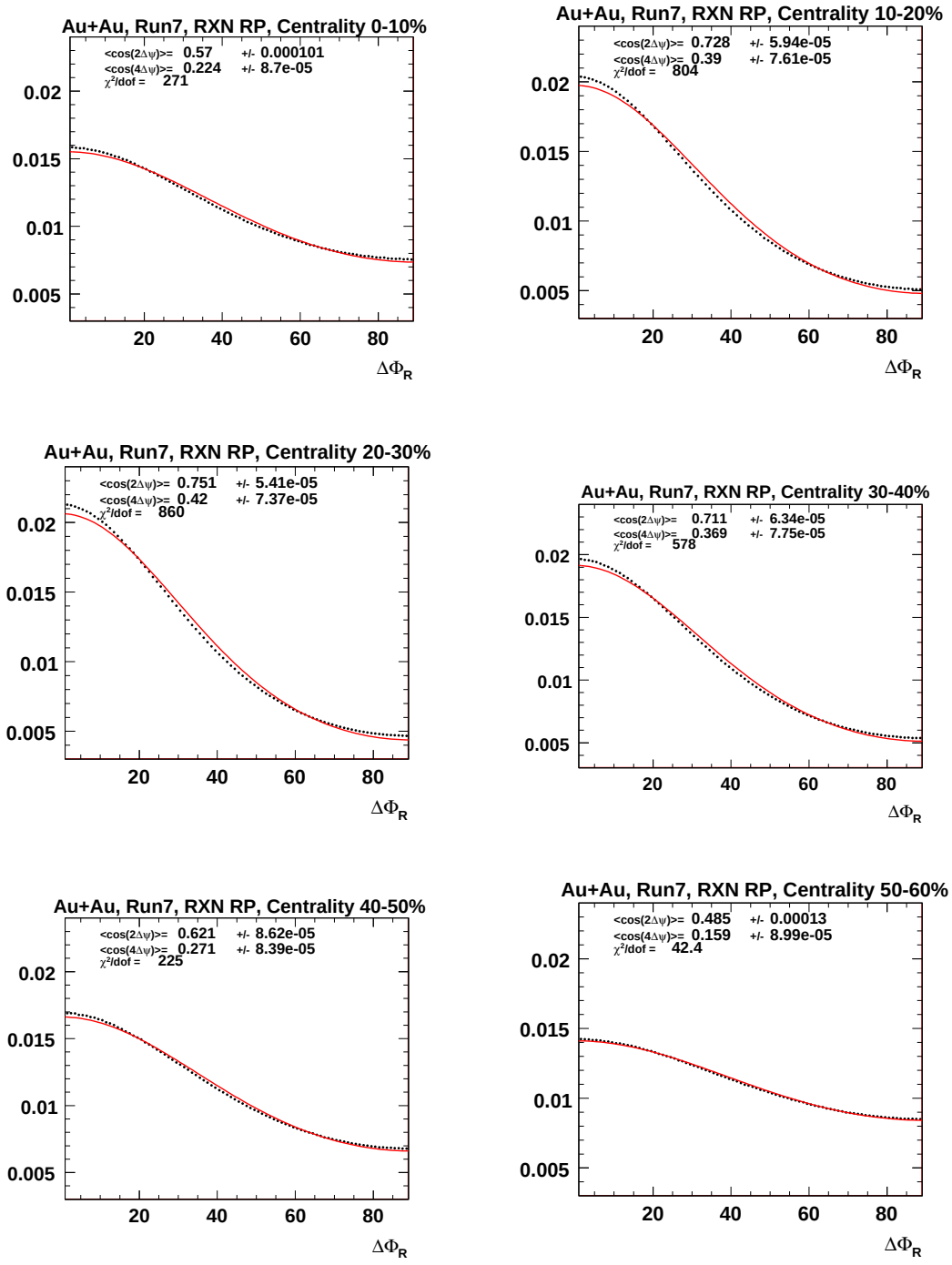


Figure 10: Estimates of the combined (S+N) RXN reaction plane resolution via the Ollitrault-Fit method for several centrality selections as indicated.

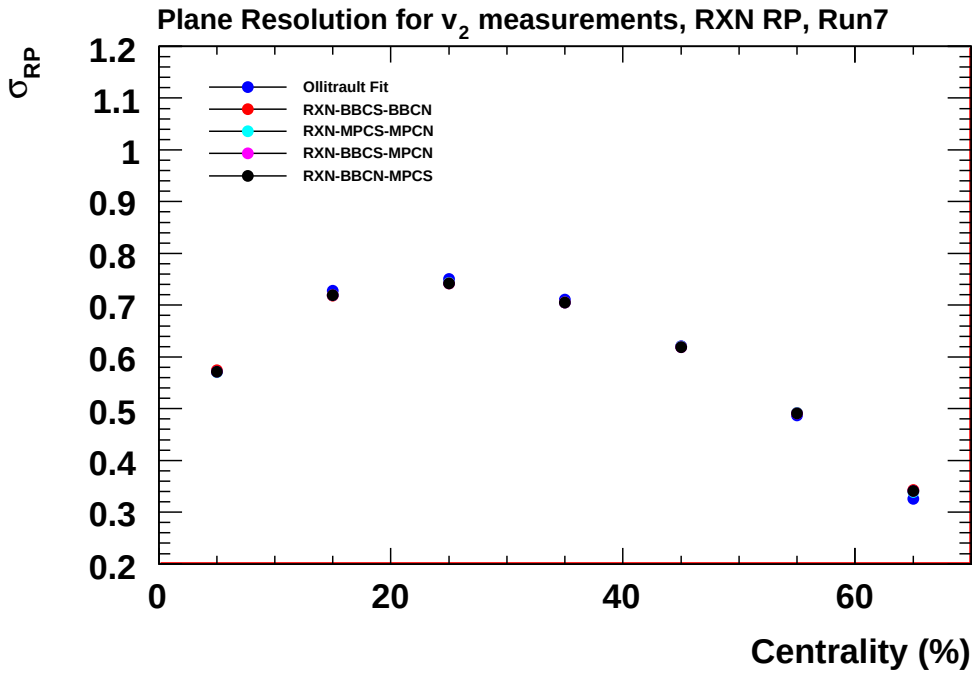


Figure 11: Centrality dependence of the dispersion correction σ_{RP} [for v_2] for the combined planes (S+N) of the RXN detector. σ_{RP} is obtained via the Ollitrault-Voloshin fit method and the 3 sub-event method; the latter exploits the correlation between the RXN - MPC South(North) - BBC North(South) event planes.

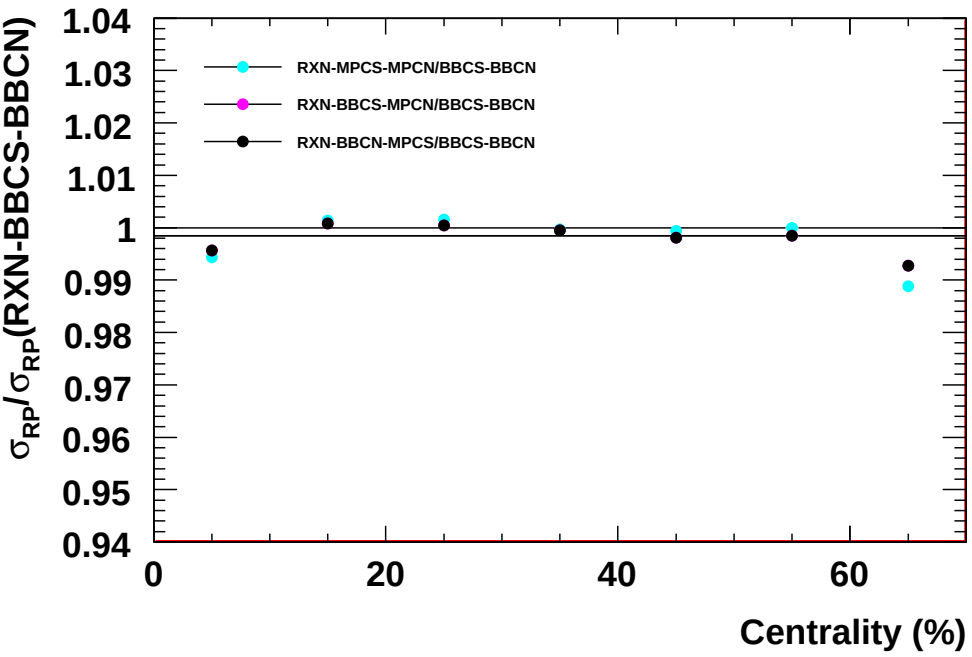


Figure 12: Centrality dependence of the dispersion correction σ_{RP} [for v_2] for the combined planes (S+N) of the RXN detector. σ_{RP} is obtained via the Ollitrault-Voloshin fit method and the 3 sub-event method; the latter exploits the correlation between the RXN - MPC South(North) - BBC North(South) event planes.

4 Particle Identification in ToF East/West

In Phenix experiment the hadron identification is based on simultaneous measurements of the particle's momentum p (measured by Drift Chamber) and time-of-flight tof (measured by high resolution TOF detectors or EMC and BBC). The particle identification (PID) technique is well developed for TOF detectors , see [6, 7], and in standart way (in Run2-Run5) user can select pions, kaons and protons using the probability functions **isPi** , **isK** and **isP** from the MasterRecalibrator which give us number of sigmas by which the measured mass square m^2_{meas} of the track deviates from the presumption that the track itself is **pion, kaon, proton** . For example $|isPi| < 2$ means $|m^2_{meas} - m^2_{centroid}(\pi)| < 2\sigma_{m^2}$, where the $m^2_{centroid}$ is the centroid position of the mass-squared distribution peak for pion and σ_{m^2} is the width of the mass squared peak (m^2 resolution). In reality the measured centroid position of the m2 distributions for pion, kaon and proton can be different from the values from the Particle Data Book and their values are momentum dependent. In case of TOF detector the momentum dependence of the centroid position of m2 distribution can be partially removed by applying the constant global TOF offset and the difference from the Particle Data Book by correcting the momentum scale as described in [7, 9].

The present version of Master Recalibrator for Run7 (Au+Au at 200 GeV) provides only the calibrated timing signals for TOF East/West detector. The usual PID functions: isPi, isK and isP are not available at the moment.
The purity of the charged pion, kaon and (anti-)protons samples as well as the p_T range for their detection are crucial for the present analysis. Consequently, a rather detailed study of the output of the Master Recalibrator for timing calibration of TOF East/West on a run-by-run and slat(strip)-by-slat(strip) level was undertaken. The results of these studies as well as methods of detection of pions, kaons and (anti-)protons are presented below.

4.1 Fine tuning of the timing calibration for ToF East/West

First the stability of T0 offsets for TOF East/West detectors was checked as a function of run number. Note that the T0 offset measures the position of the peak of the distribution **tof**-time (expected for high p_T pion). Fig. **??** shows run-by-run variations of the residual T0 offset for charged pions with momentum 0.6$\leq$ p $\leq$ 0.9 GeV/c and the E_{cent} range 0.25-0.4 GeV, after application of the Master Recalibrator. As one can see, small corrections are needed for each run.

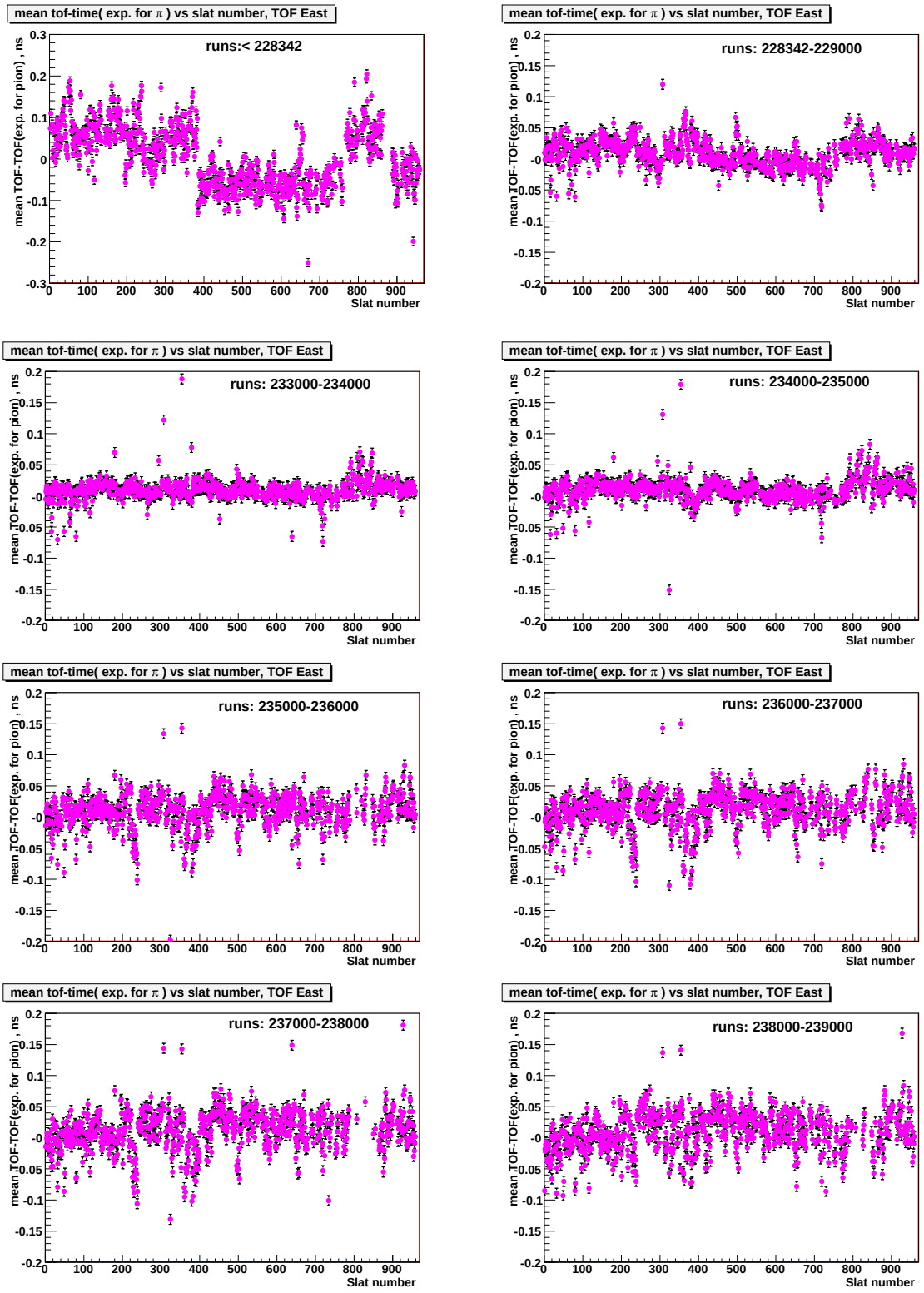


Figure 13: TOF East: T0 offset (mean of ¡tof-time (expected for π)¿) as a function of slat number for different groups of runs.

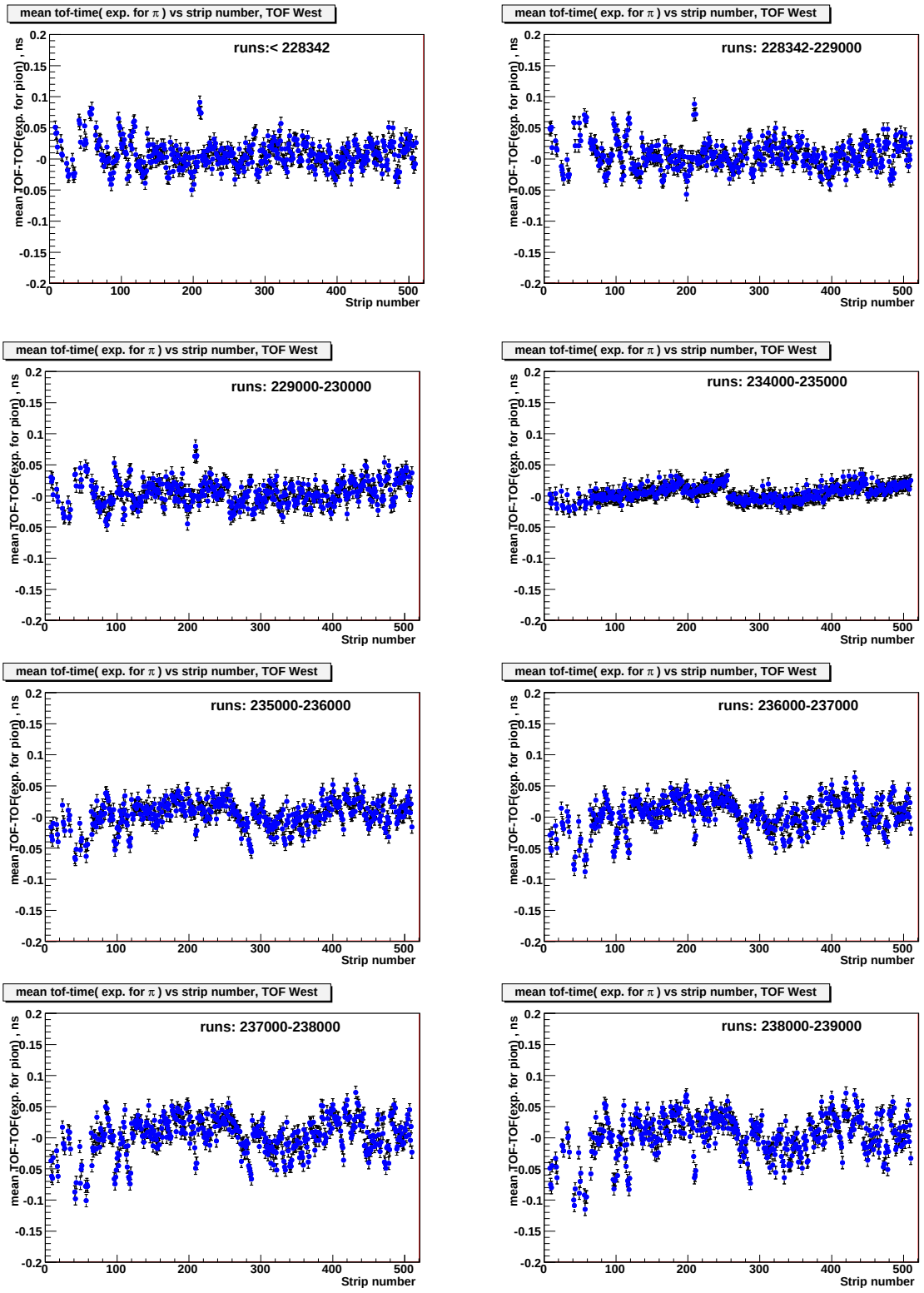


Figure 14: TOF West: T0 offset (mean of ¡tof-time (expected for π)¿) as a function of strip number for different groups of runs.

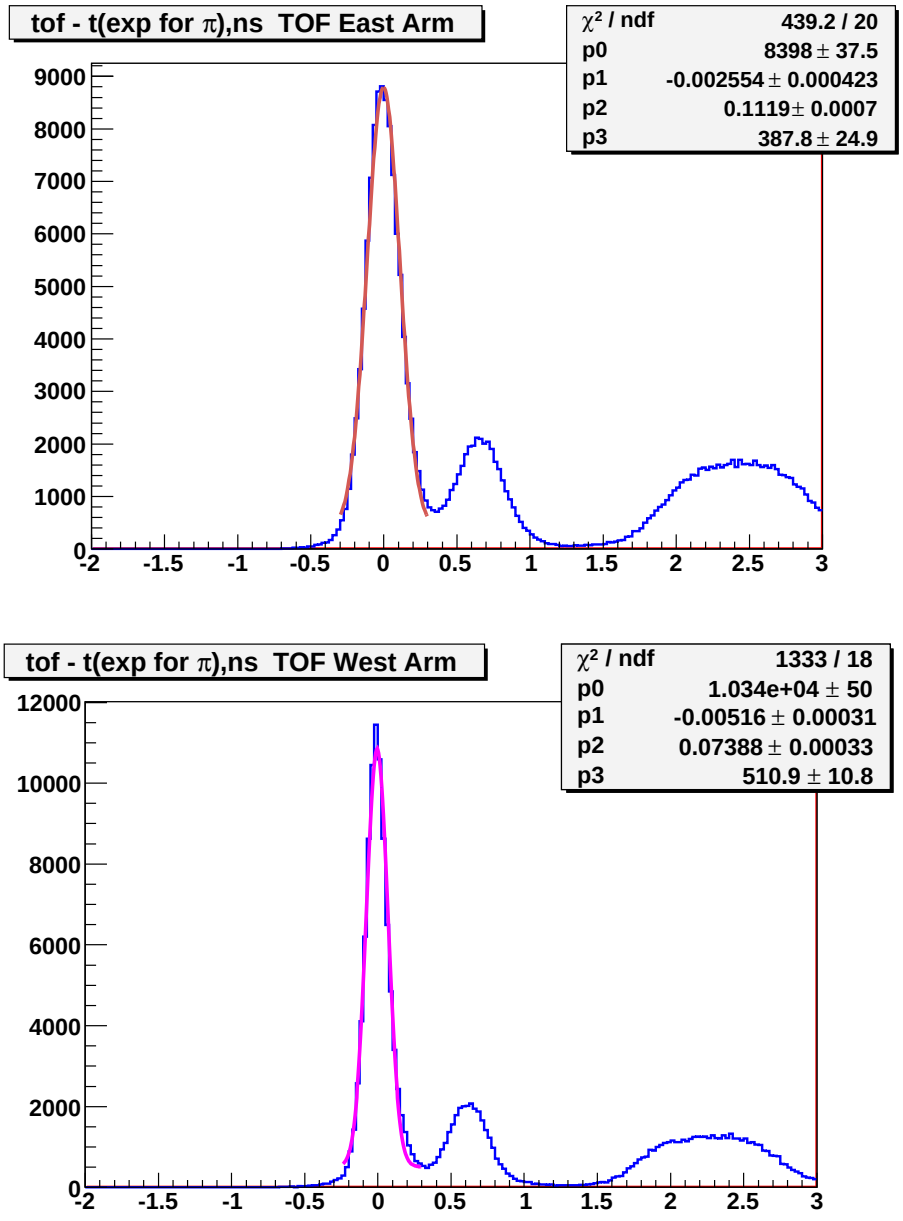


Figure 15: An example of distribution of the difference between measured and expected time for high (1.5-1.9 GeV/c) p_T pions for TOF East (top panel) and TOF West (bottom panel) for a single run after fine tuning of timing calibration

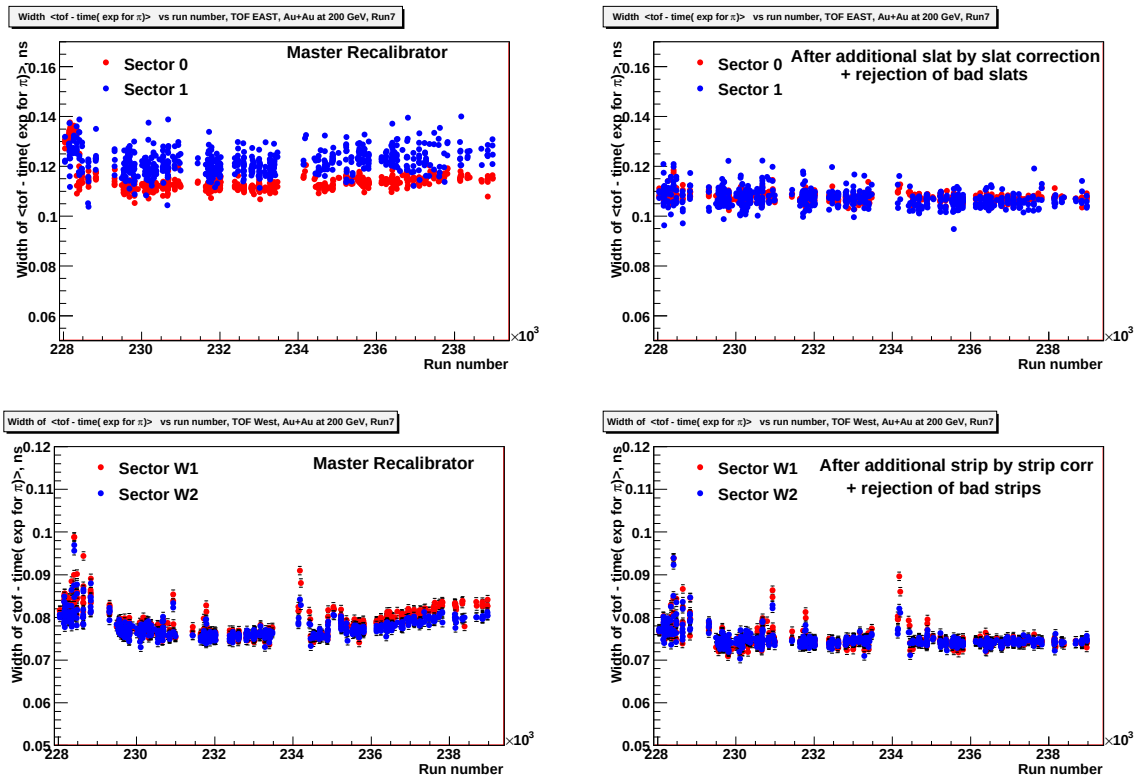


Figure 16: Left panel: timing resolution for high p_T pions as a function of run number for TOF East (left top panel) and TOF West (left bottom panel) as it is coming after Master Recalibrator. Rigth pane: timing resolution for high p_T pions as a function of run number for TOF East (left top panel) and TOF West (left bottom panel) after additional slat-by-slat/strip-by-strip corrections for T0 offset and rejection of slat/strips with "bad" resolution.

4.2 Beam Shift and Momentum Scale Calibration

Beam Shift and Momentum Scale Calibration was performed togather with S. Huang and briefly explained in this section. More detailed information and all suporting plots are available at [**?**].

Beam Shift Correction: A shift of the beam position from the nominal origin of PHENIX detector will produce an systematic offset in mean α value, which can be parameterized as function of azimuthal angle ϕ as:

$$= X_{off} * sin(\phi)/R_{DC} + Y_{off} * cos(\phi)/R_{DC} \quad (4)$$

where R_{DC} is Drift chamber radius = 220 cm.
The procedure of extracting (X_{off}, Y_{off}) from the fit of α vs ϕ by Eq 1 using the zero-field runs is explained in details in [**?**, **?**]. The following Run7 AuAu zero-field runs were reconstructed: **229545, 231156,236137, 238530, 238531, 238971, 239312** and used to get initial set of (X_{off}, Y_{off}) values for East and West Arm. For the final set of (X_{off}, Y_{off}) values for different groups of runs we look at the systematic shift in proton and anti-proton m^2 value for TOF East and TOF West, the similar way as it was done in AN 296 [**?**].
Momentum Scale: After correction of momentum for beam shift we calculate the mean m^2 of the proton and antiproton using momentum and time-of-flight information from TOF East/West (tof). In general case m^2 of the particle depends both on momentum scale A_p and T0 offset

$$m^2 = (A_p p)^2 \left[\frac{(tof + T0)^2 c^2}{d^2} - 1 \right]$$

. The careful checks were performed using tof-time(expcted for π) for high p_T=1.4-1.8 GeV/c pions to be sure that T0 offset is zero and timing calibration done properly. Then the magnitude of $M_+ = (m_p^2 + m_{\bar{p}}^2)/2$ - 0.9382 gives the momentum scale of the DC via $M_+/2/0.9382$ [**?**].

4.3 PID Functions

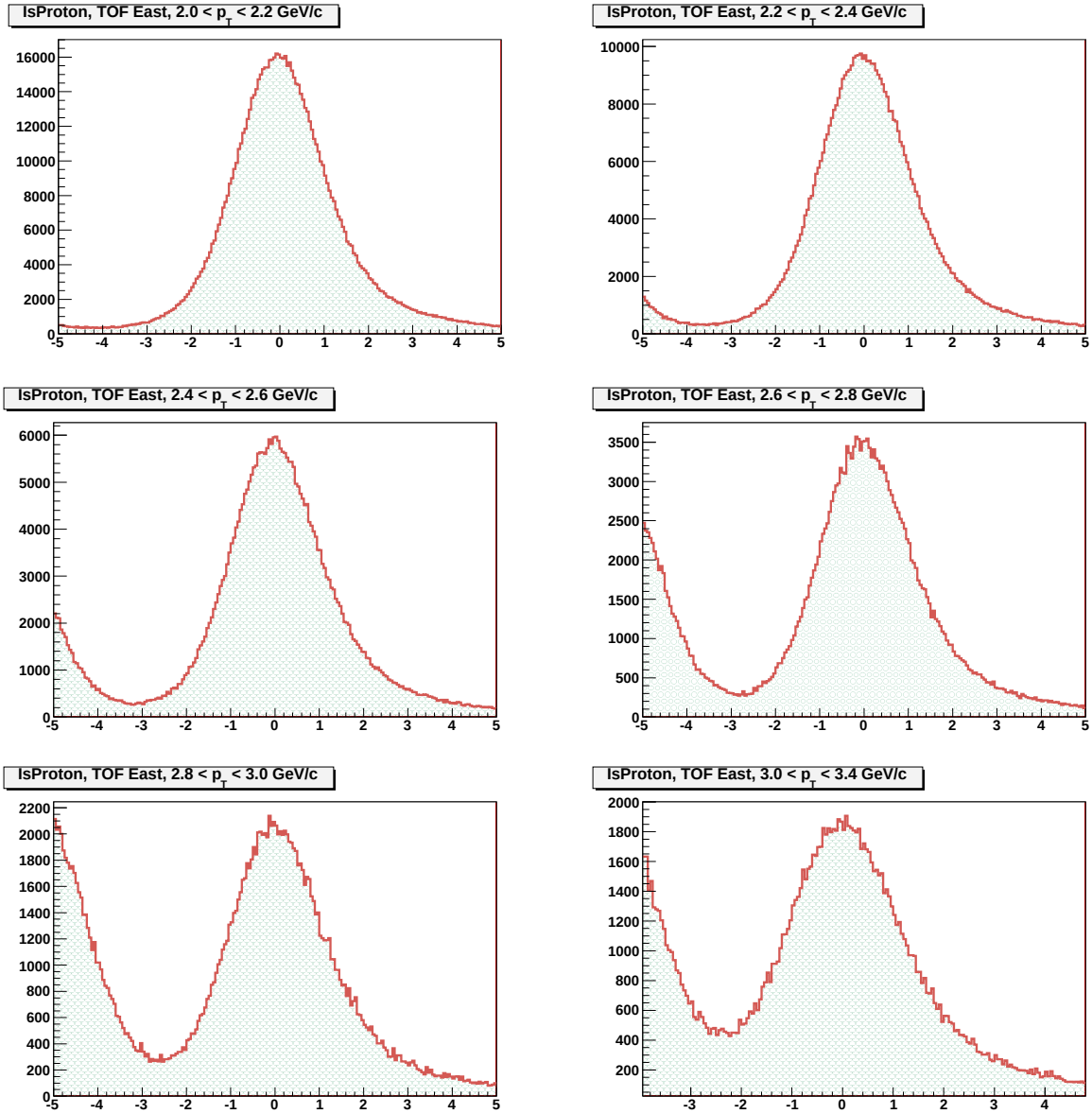


Figure 17: Example of n-sigma distribution IsProton (TOF East) for several bins in transverse momentum p_T

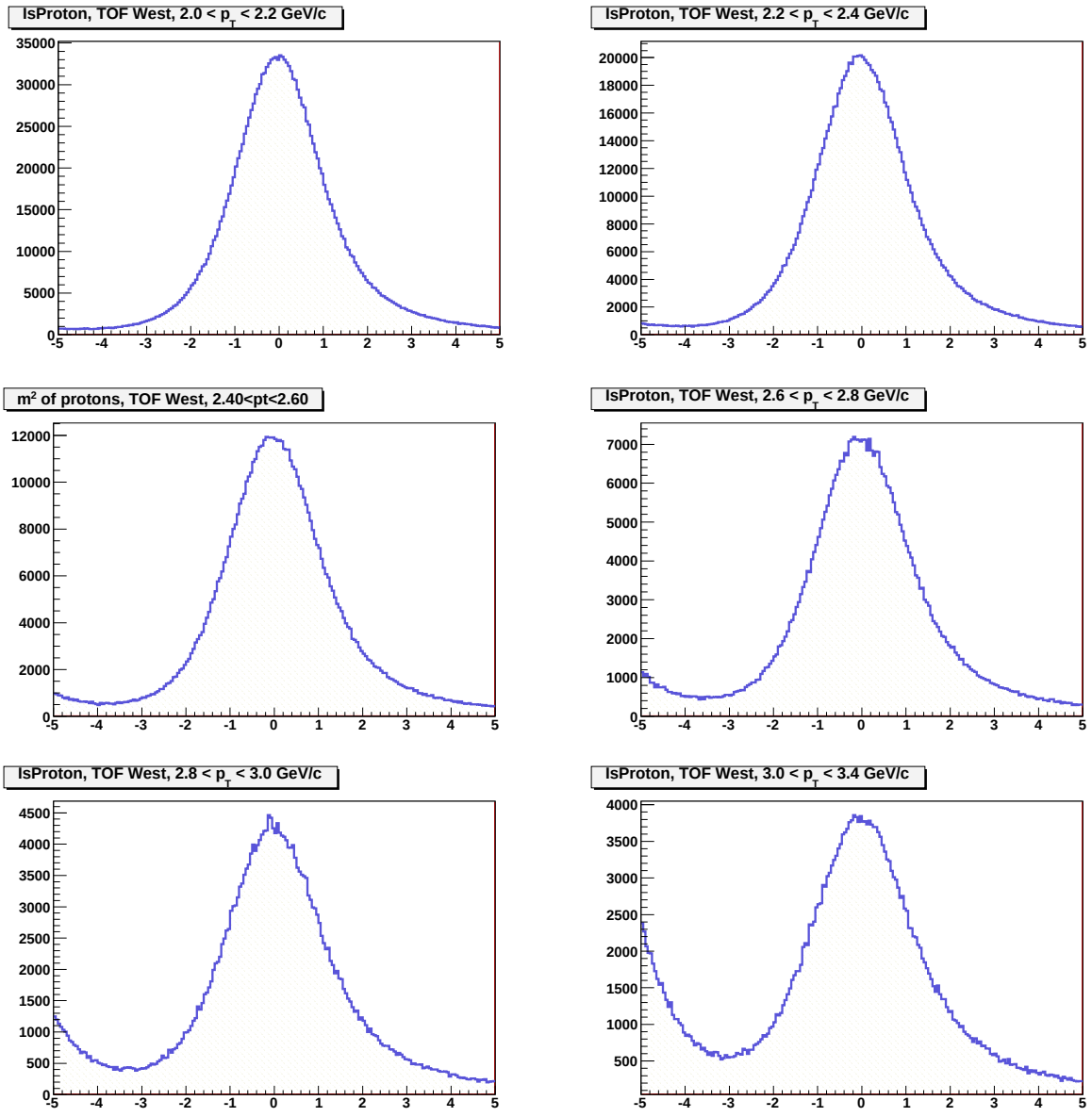


Figure 18: Example of n-sigma distribution IsProton (TOF West) for several bins in transverse momentum p_T

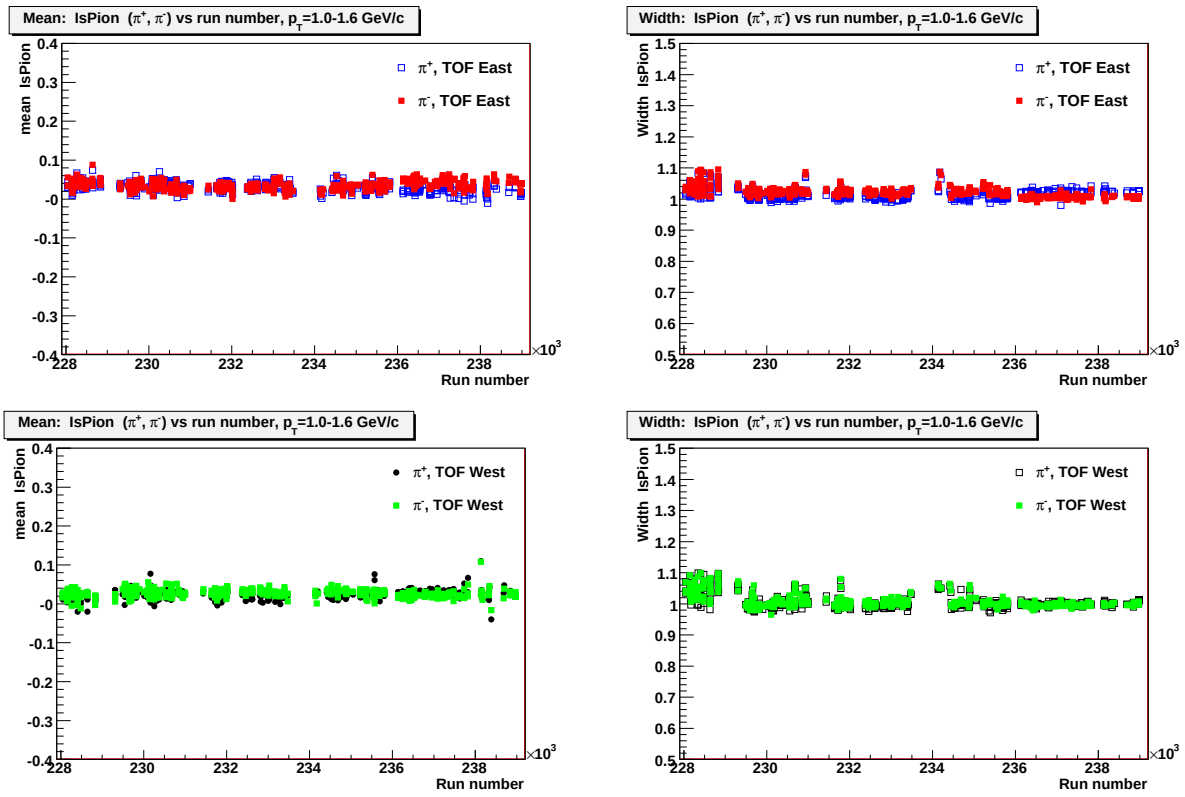


Figure 19: Check of the run-by-run dependence of the mean (left panel) and width (rigth panel) of n-sigma distrobution IsPion for particles detected in TOF East (top panel) and TOF West (bottom panel).

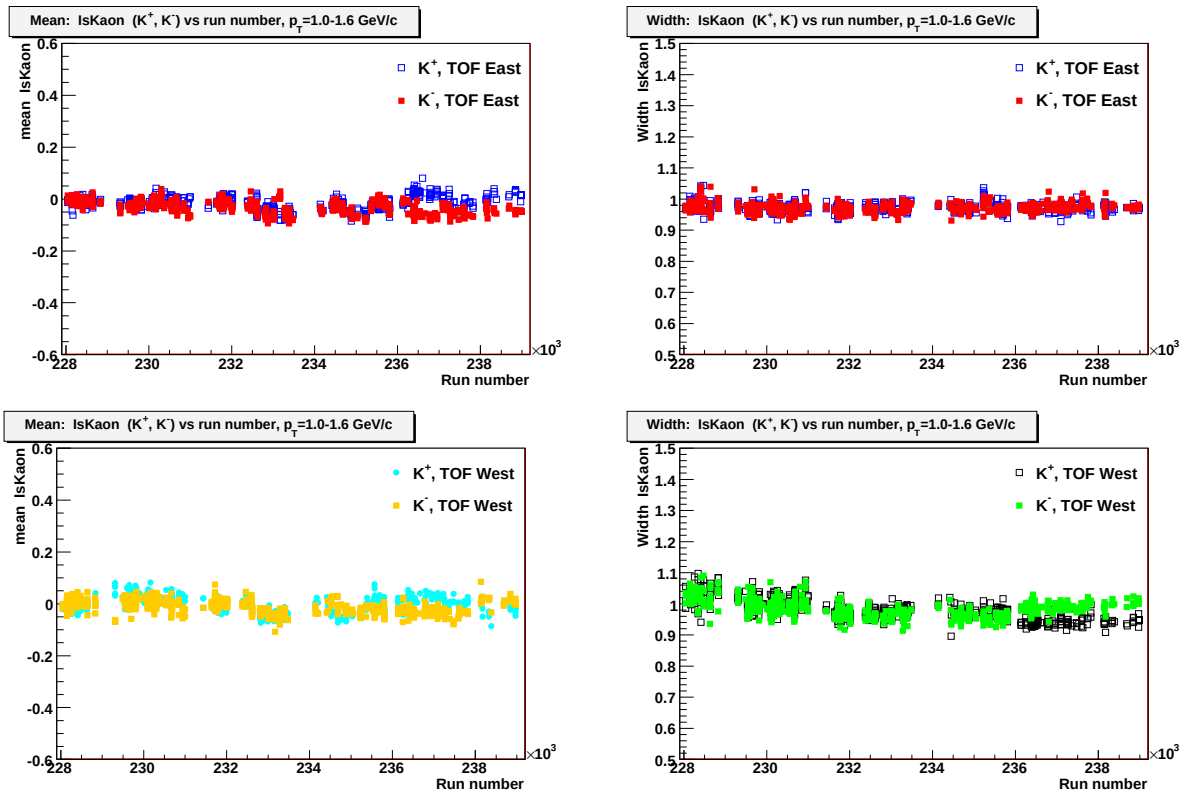


Figure 20: Check of the run-by-run dependence of the mean (left panel) and width (rigth panel) of n-sigma distrobution IsKaon for particles detected in TOF East (top panel) and TOF West (bottom panel).

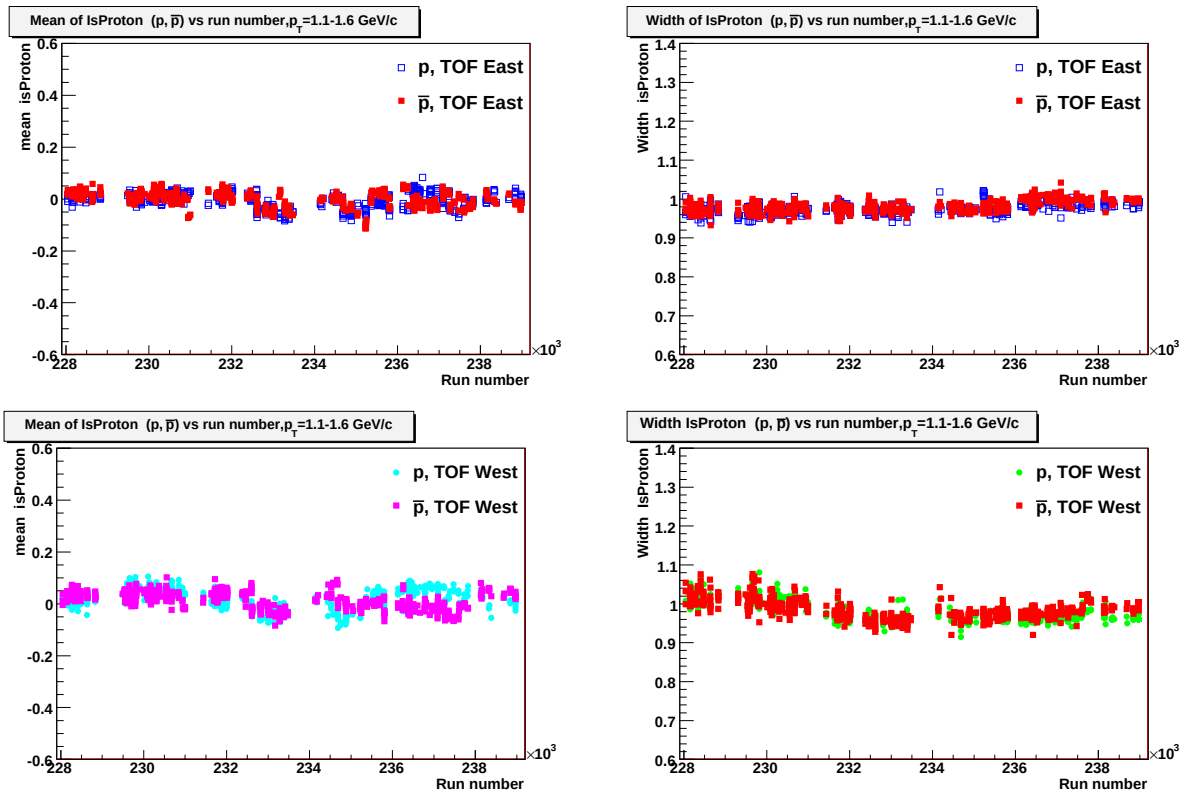


Figure 21: Check of the run-by-run dependence of the mean (left panel) and width (rigth panel) of n-sigma distrobution IsProton for particles detected in TOF East (top panel) and TOF West (bottom panel).

5 Results

Systematic extractions of v_2 and v_4 were made for both identified and unidentified charged hadrons as a function of p_T and centrality. In addition, systematic studies were performed to evaluate the influence of imperfections in the flatness of the centrality distribution and reaction plane, etc .. etc.. Where possible, extensive comparisons were also made between the results of the current analysis and those from our earlier analysis of Run 4 data. For the latter, overall good agreement is observed.

5.1 Elliptic flow of charged hadrons

Figures 22 and 25 give a detailed comparison of the the differential $v_2(p_T)$ for charged hadrons. As shown, these measurements are relatively insensitive to small deviations ($5 < \chi^2/ndf < 80$) from the expected flat distributions for the centrality distributions and stable across different run groups.

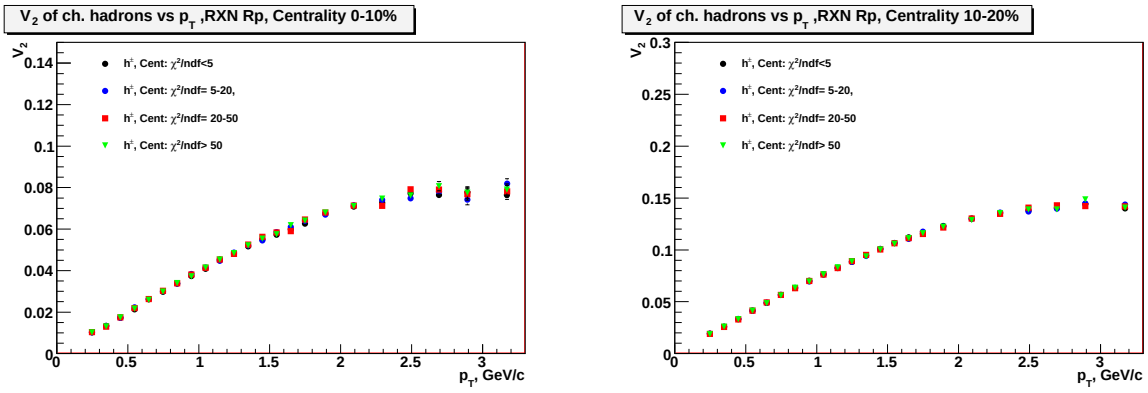


Figure 22: v_2 of charged hadrons as a function of transverse momentum p_T for the centrality selections 0-10% and 10-20%. Results are shown for several run groups selected according to the value of χ^2/ndf of the fit of the centrality distributions. The v_2 measurements were performed with respected to the combined RXN event plane.

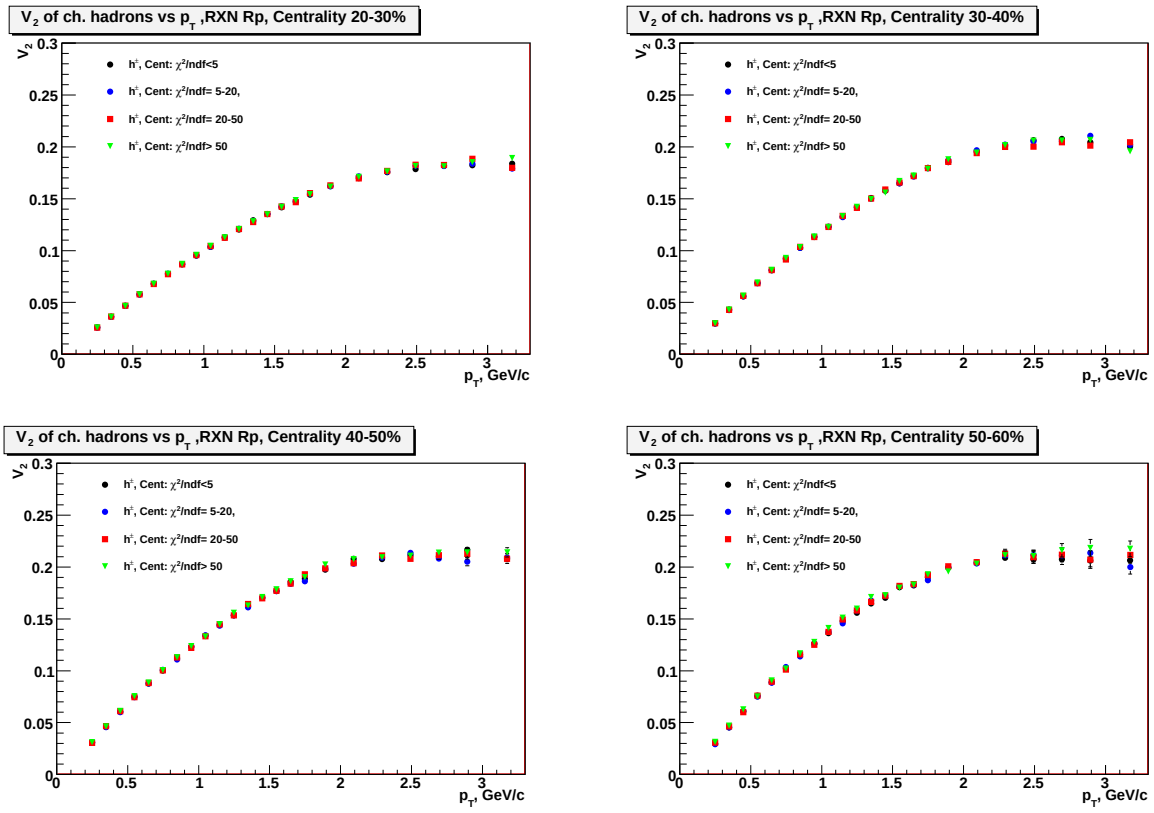


Figure 23: v_2 of charged hadrons as a function of transverse momentum p_T for the centrality selections 20-30%, 30-40%, 40-50% and 50-60%. Results are shown for several run groups selected according to the value of χ^2/ndf of the fit of the centrality distributions. The v_2 measurements were performed with respected to the combined RXN event plane.

As the next step: we perfomrmed detailed comparison of v_2 measurements with respect to the diffent combined event planes (South+North): RXN, RXN Outer Part, BBC and MPC. The resulting v_2 values are in a good agreement. In the same figure we compared the Run7 results with published results for v_2 of charged hadrons from Run4 measured with respect to the BBC event plane (results of PPG 062). As can be seen, the Run7 v2 values for the 0-10This can be attributed to the different methods for centrality determination: the centrality for the Run4 data has been determined by the "clock" method that utilizes the correlation of the BBC charge sum and the ZDC energy. For Run7 such a centrality calibration has not yet been done. Rather, the centrality has been estimated using the BBC charge sum alone. Ever small shift between centrality definition of the order of one is small and growing very fast with centrality. In order to check this we performed measurements with centrality classes shifted by 1the results are in a very good agreement with ppg 062 if one assume 1

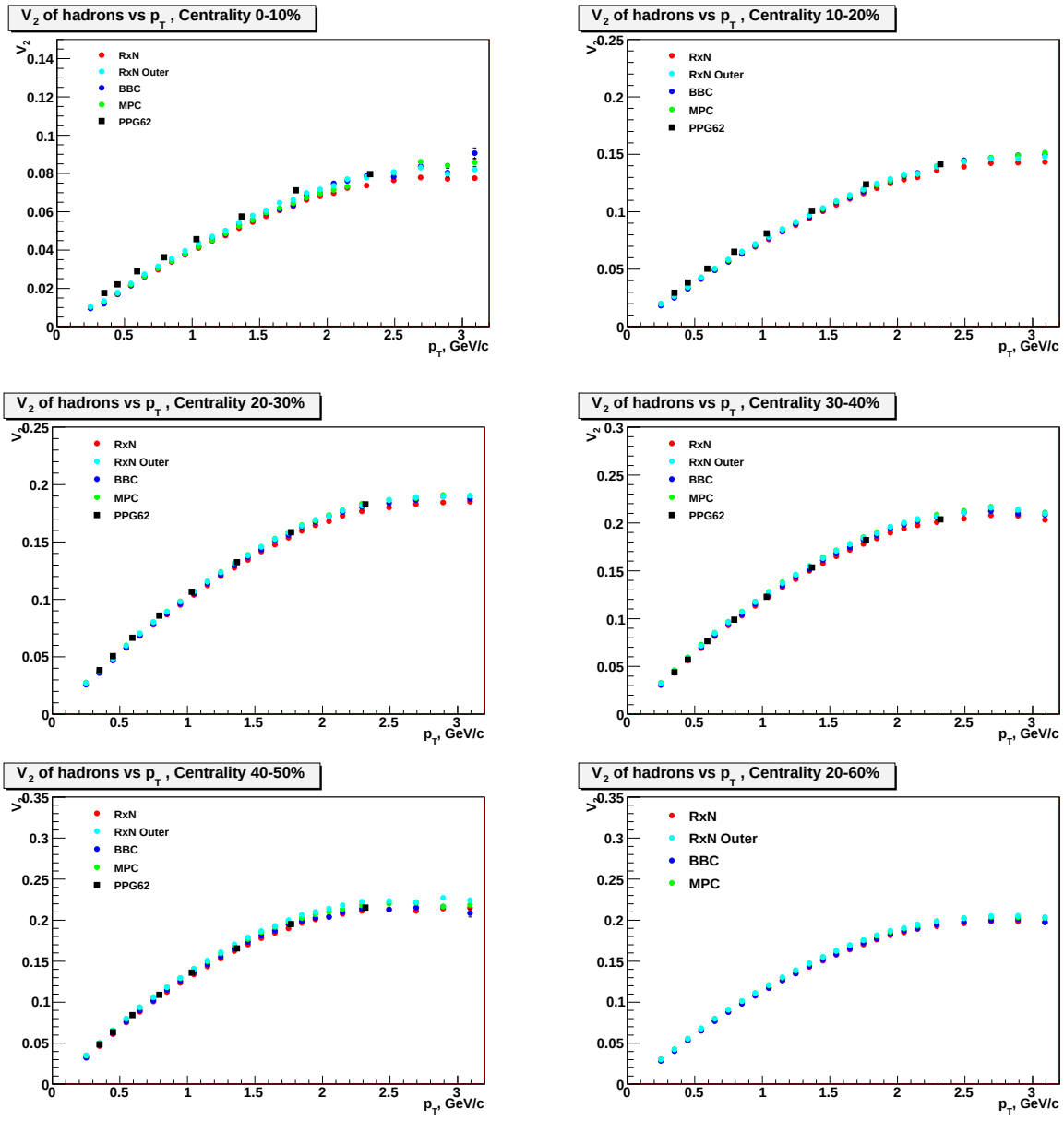


Figure 24: v_2 of charged hadrons as a function of transverse momentum p_T for the centrality selections 0-10%, 10-20%, 20-30%, 30-40%, 40-50% and 20-60% . The v_2 measurements were performed with respected to the combined event planes (South+North): RXN, RXN Outer Part, BBC and MPC. The published results from Run4 (ppg062) are plotted for comparison (black boxes)

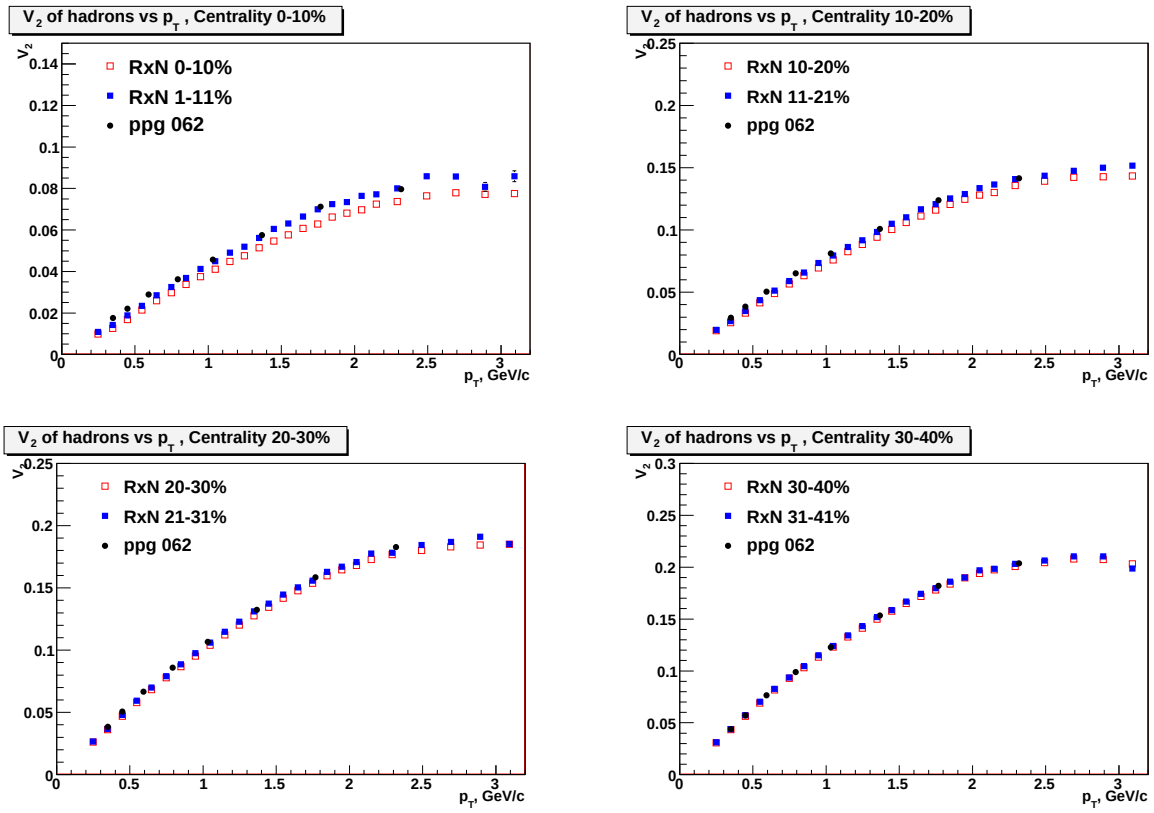


Figure 25: v_2 of charged hadrons as a function of transverse momentum p_T for the centrality selections 0-10%, 10-20%, 20-30% and 30-40% and shifted by 1The v_2 measurements were performed with respected to the combined RXN event plane. The published results from Run4 (ppg062) are plotted for comparison

5.2 Elliptic flow of identified charged hadrons

Subsequent to v_2 extraction for identified charged hadrons, a comparison was made between the results from the current analysis and those reported in PPG073 [?] and published in [?].

The comparisons shown in Fig. [?, ?] for the centrality selection 20-60% indicate good agreement between both measurements.

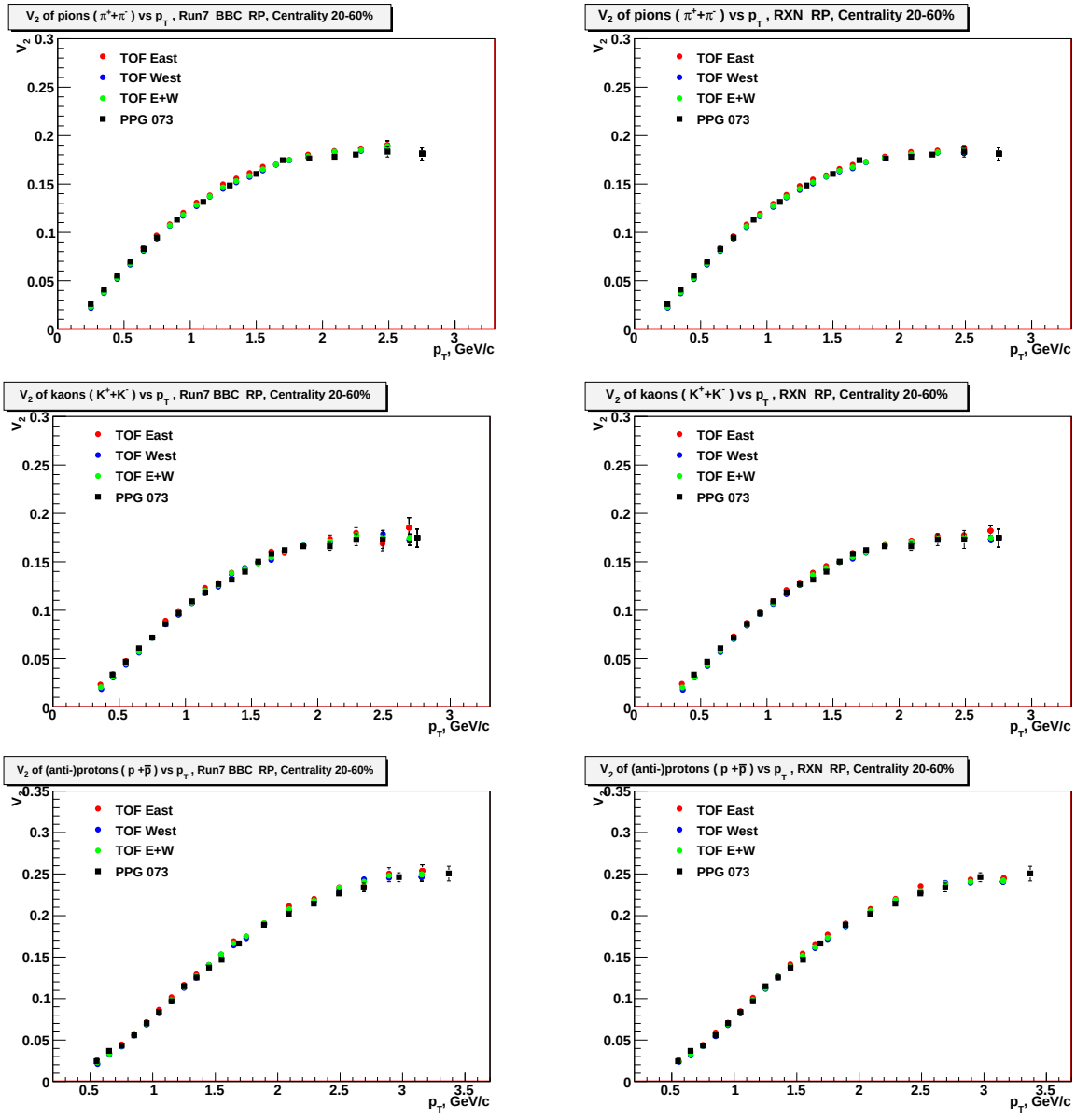


Figure 26: v_2 vs p_T for charged pions, kaons and (anti)protons for 20-60% central Au+Au collisions at 200 GeV measured with respect to the BBC combined reaction plane (left panel) and RXN combined reaction plane (right panel)

5.3 v_4 vs p_T of identified charged hadrons

v_4 values were also extracted and compared to the results of similar extractions from Run 4 data [**?**].

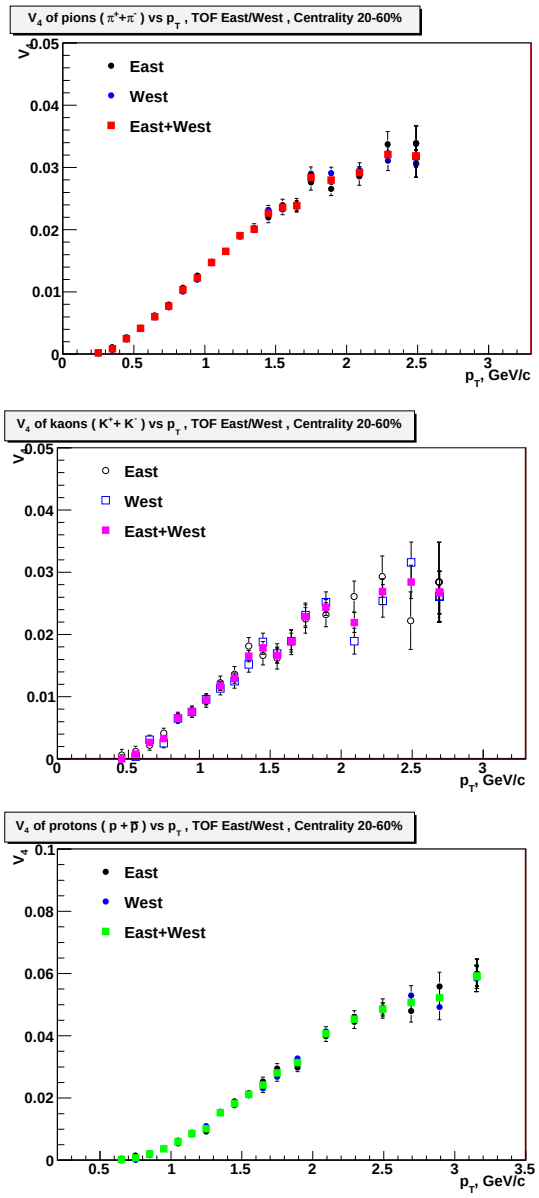


Figure 27: v_4 vs p_T for charged pions, kaons and (anti)protons for 20-60% central Au+Au collisions at 200 GeV measured with respect to the RXN combined reaction plane

5.4 v_4 vs KE_T of identified charged hadrons

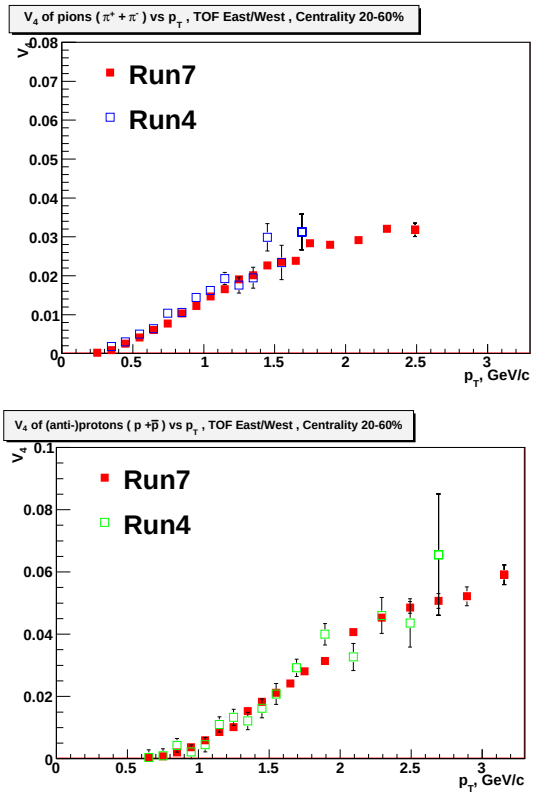


Figure 28: v_4 vs p_T for charged pions, kaons and (anti)protons for 20-60% central Au+Au collisions measured with respect to the RXN combined reaction plane

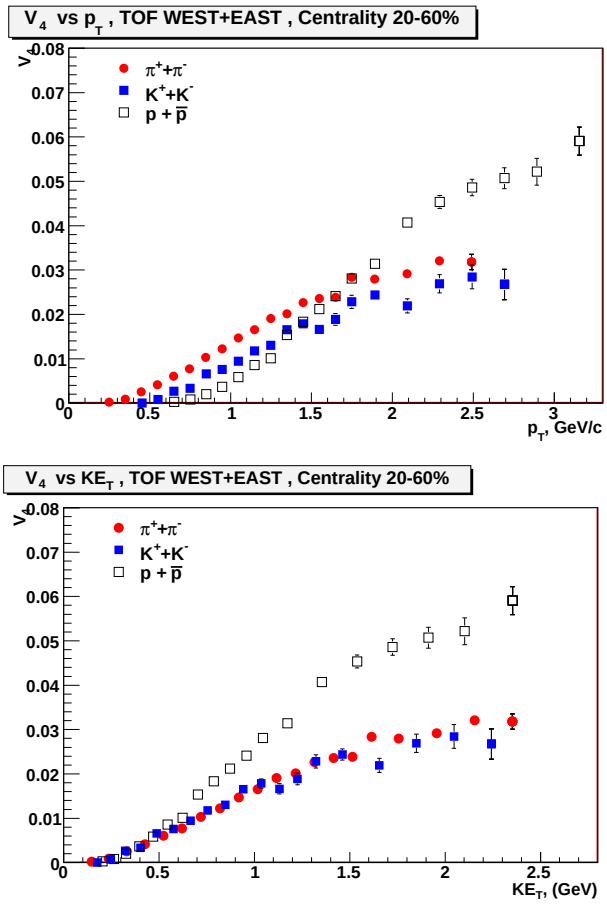


Figure 29: v_4 vs p_T for charged pions, kaons and (anti)protons for 20-60% central Au+Au collisions measured with respect to the RXN combined reaction plane

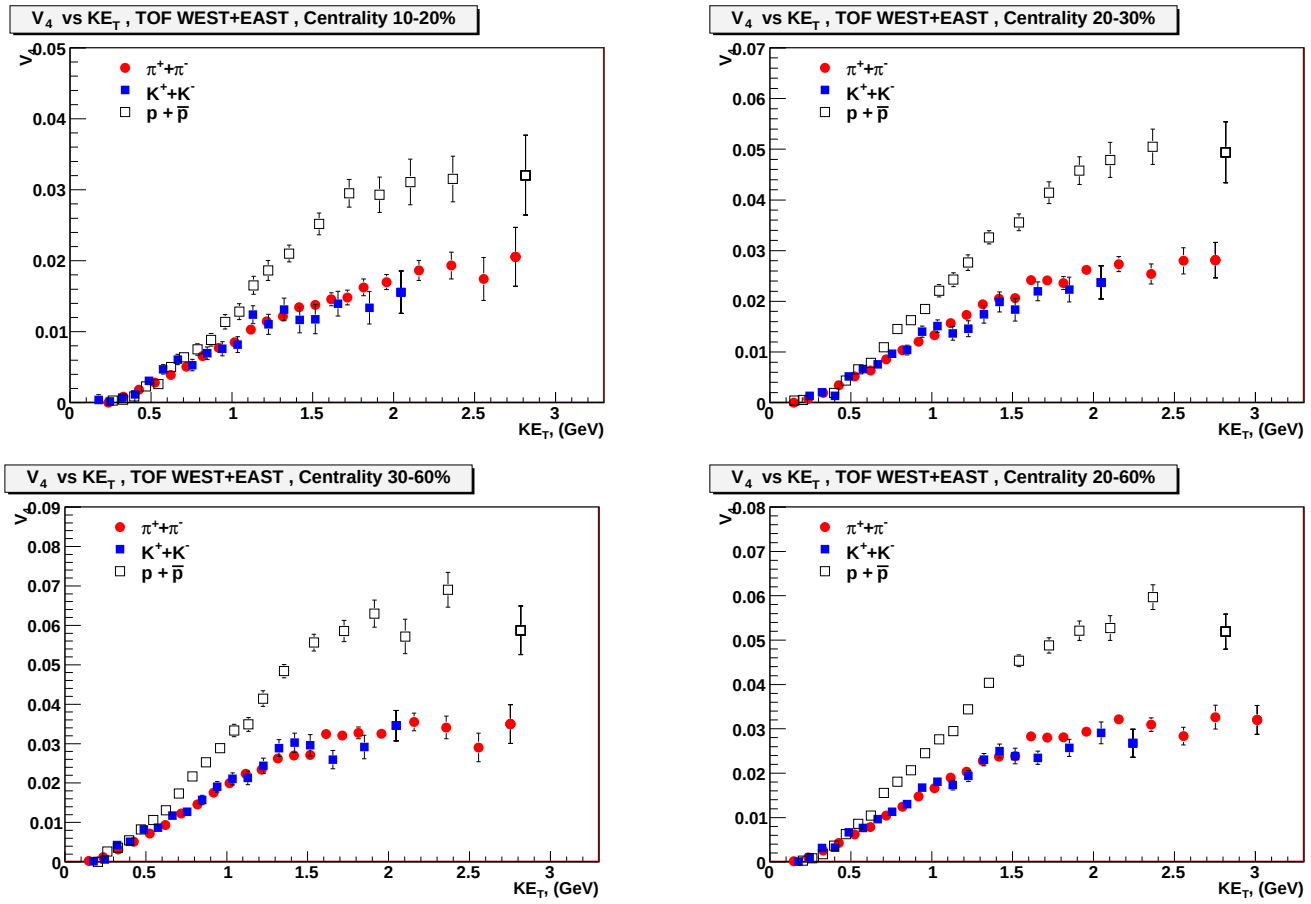


Figure 30: v_4 vs KE_T for charged pions, kaons and (anti)protons for 20-60% central Au+Au collisions measured with respect to the RXN combined reaction plane

5.5 Systematic Errors

We estimate the systematic errors from

- comparison of $v_4(p_T)$ with respect to the different event planes, such as MPC and BBC: from 10
- comparison of v_4 for several Run groups with equal statistics: 2
- matching cuts: $2 - 2.5\sigma$ (pc3+tof): 2-3
- PID cuts and separate measurements TOF East/West:

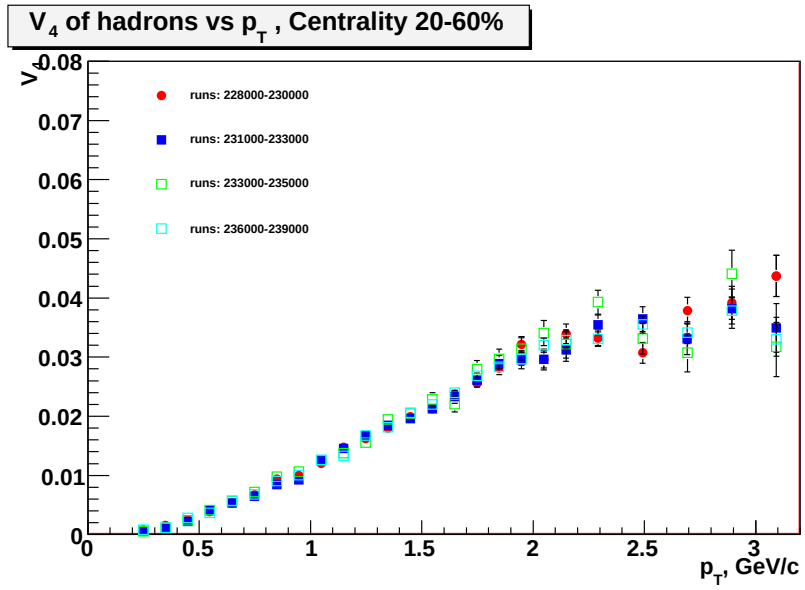


Figure 31: v_4 vs p_T for charged hadrons for 20-60% central Au+Au collisions at 200 GeV measured with respect to the RXN combined reaction plane. The measurements were performed for four run groups.

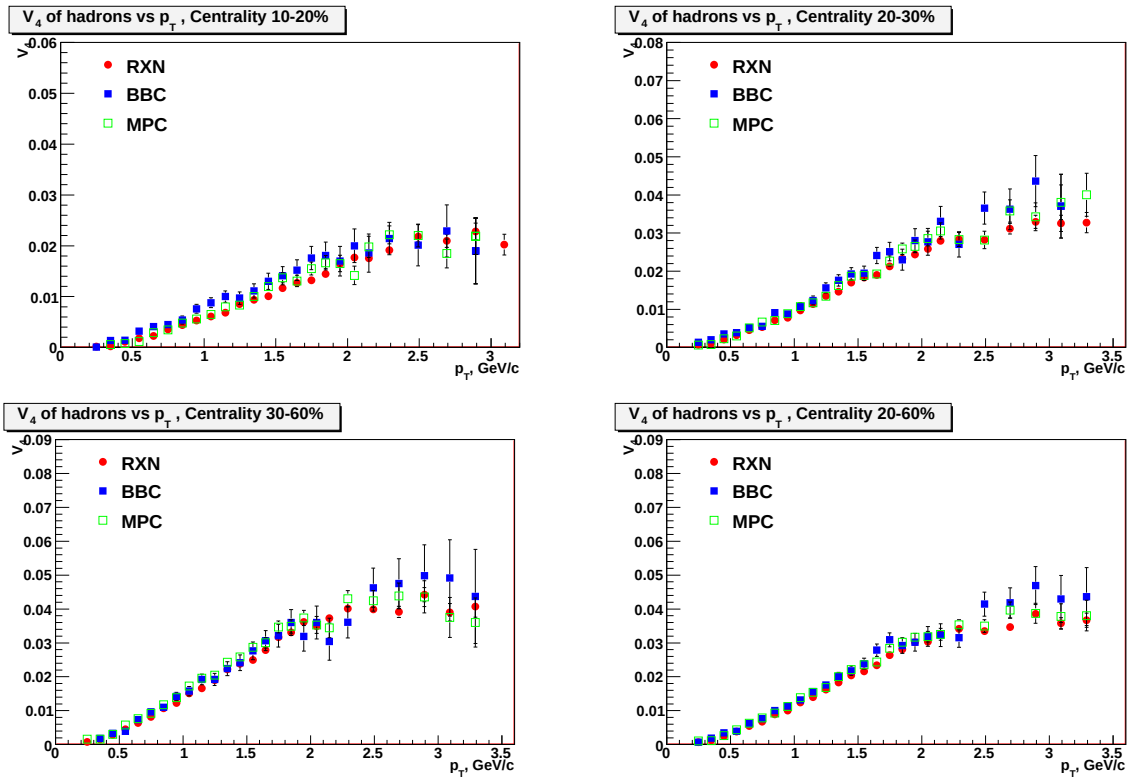


Figure 32: v_4 vs p_T for charged hadrons for 20-60% central Au+Au collisions at 200 GeV measured with respect to the RXN combined reaction plane. The measurements were performed for four run groups.

6 Plots requested for Preliminary

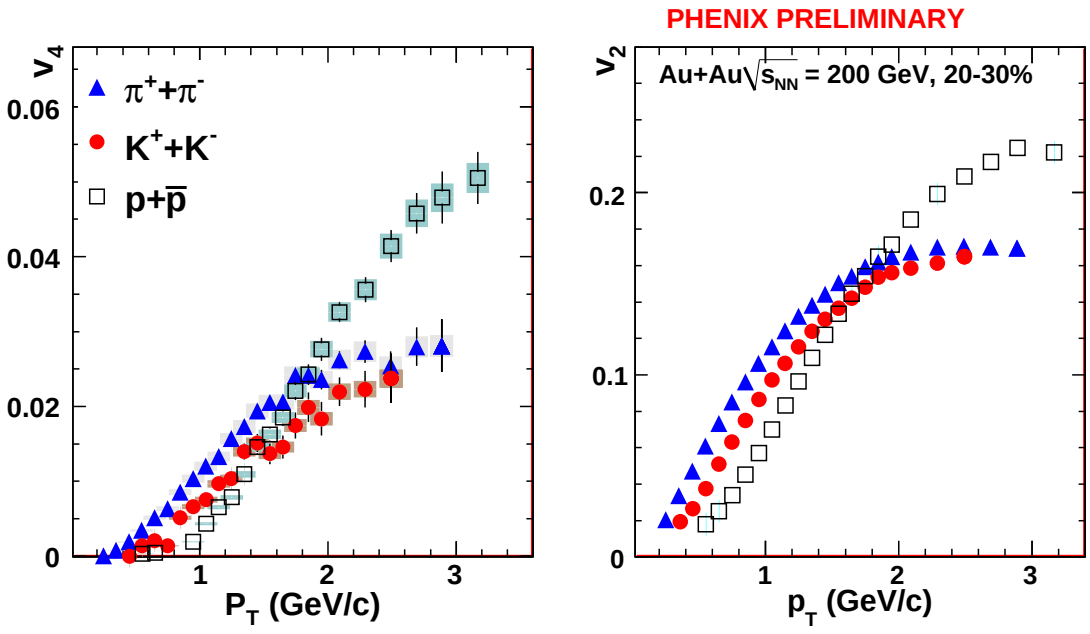


Figure 33: v_4 vs p_T (left panel) and v_2 vs p_T (right panel) for charged pions, kaons and (anti-)protons for 20-30% central Au+Au collisions at 200 GeV measured with respect to the RXN combined reaction plane.

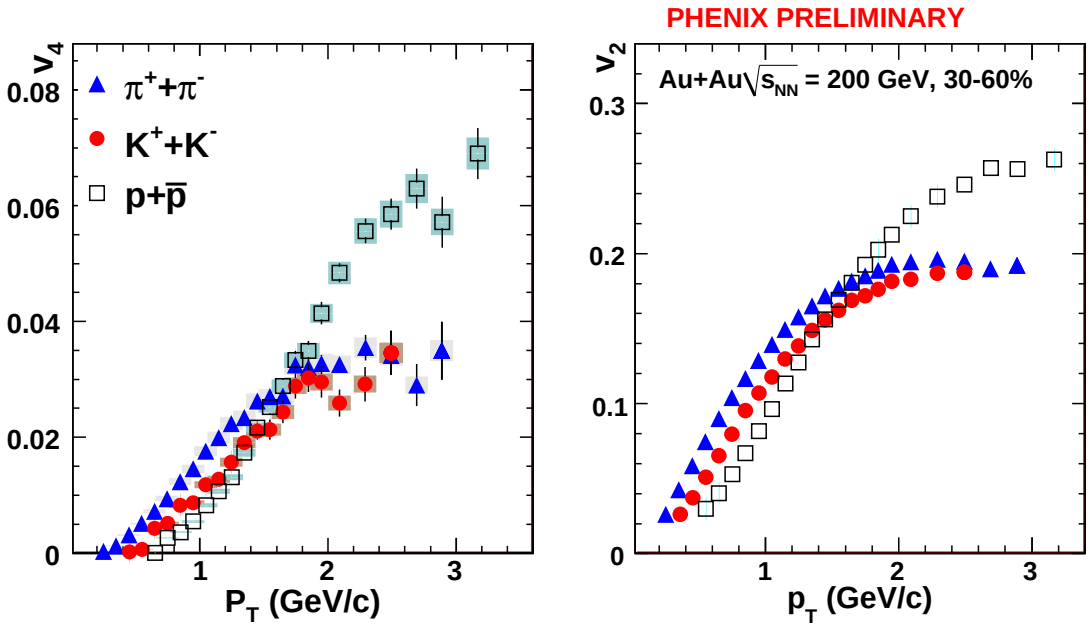


Figure 34: v_4 vs p_T (left panel) and v_2 vs p_T (right panel) for charged pions, kaons and (anti-)protons for 30-60% central Au+Au collisions at 200 GeV measured with respect to the RXN combined reaction plane.

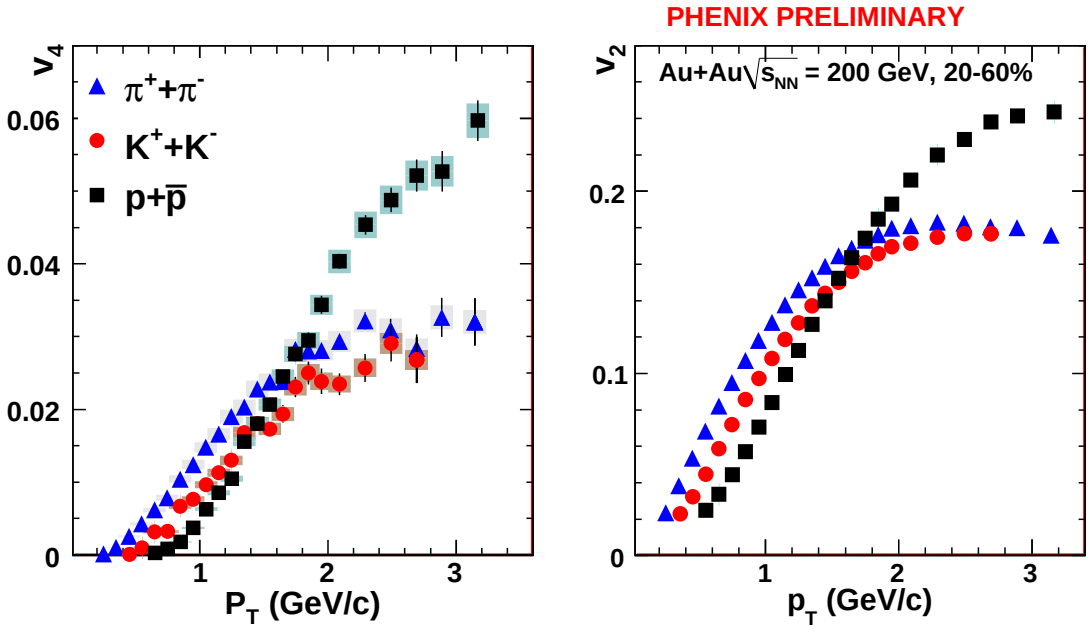


Figure 35: v_4 vs p_T (left panel) and v_2 vs p_T (right panel) for charged pions, kaons and (anti-)protons for 20-60% central Au+Au collisions at 200 GeV measured with respect to the RXN combined reaction plane.

7 Elliptic flow of identified charged hadrons TOF/EMC

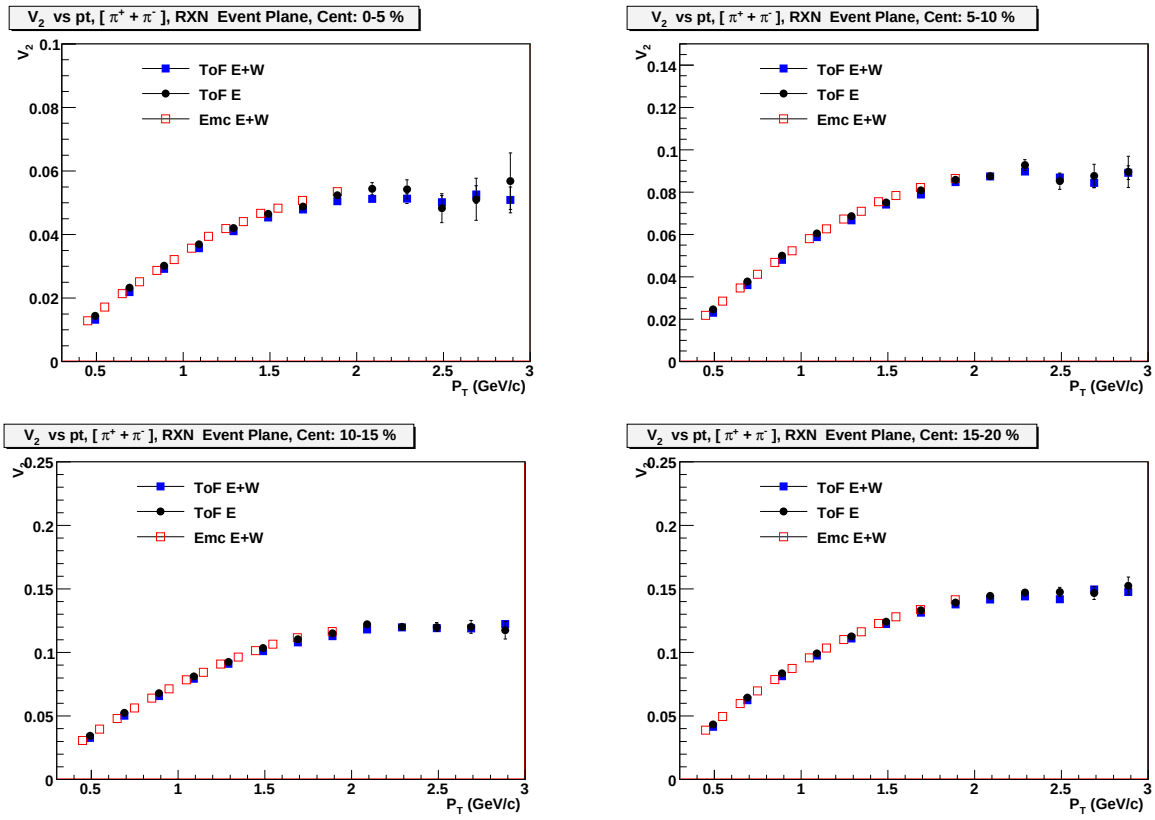


Figure 36: P_T dependence of elliptic flow of charged pions [$\pi^+ + \pi^-$] measured with respect to the combined RXN event plane. Different symbols and colors correspond to the pions detected by time-of-flight method using TOF East, TOF WEST+EAST and EMC (PbSc) as indicated. The results are presented for different bins in reaction centrality as indicated in each panel.

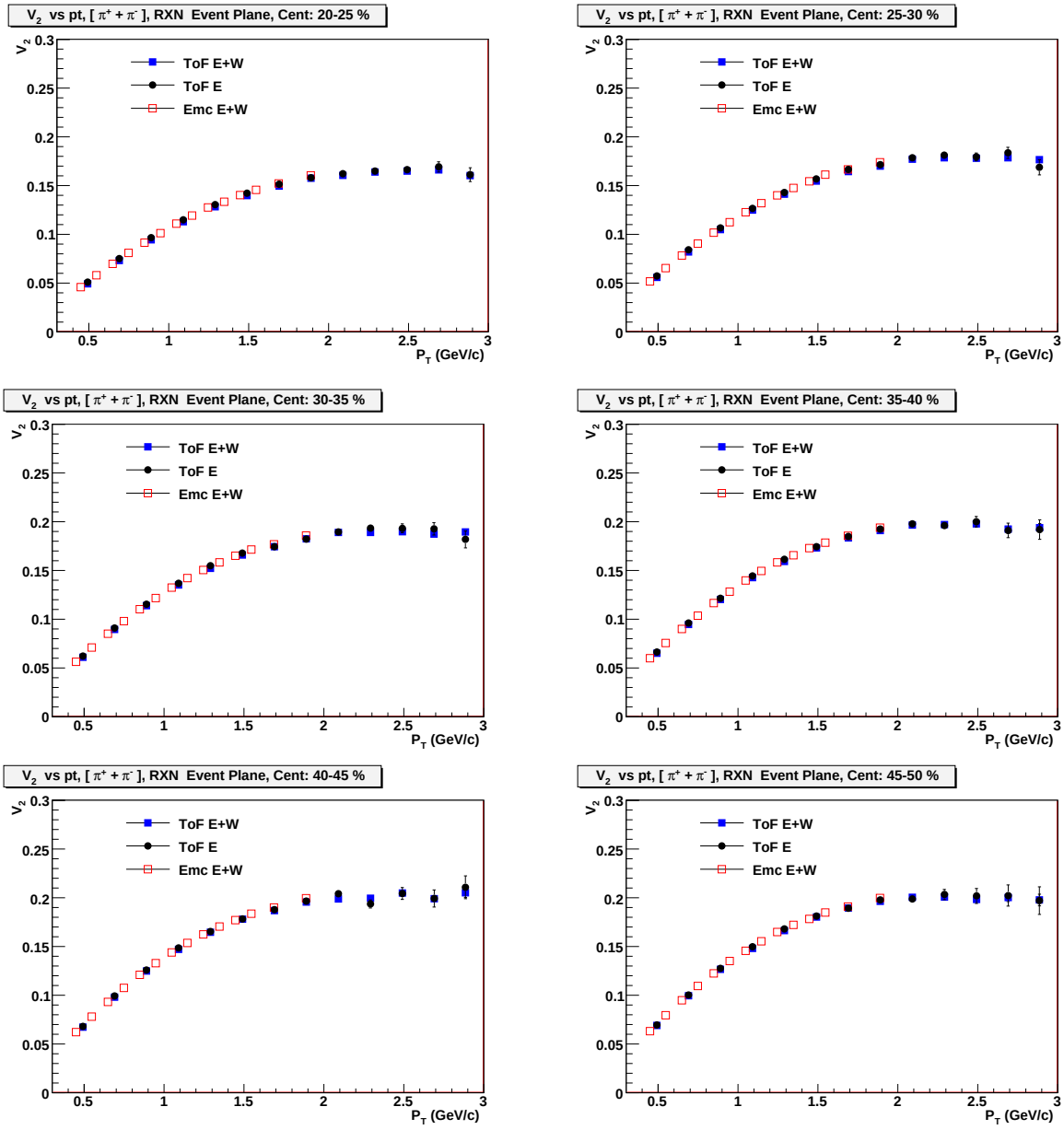


Figure 37: P_T dependence of elliptic flow of charged pions [$\pi^+ + \pi^-$] measured with respect to the combined RXN event plane. Different symbols and colors correspond to the pions detected by time-of-flight method using TOF East, TOF WEST+EAST and EMC (PbSc) as indicated. The results are presented for different bins in reaction centrality as indicated in each panel.

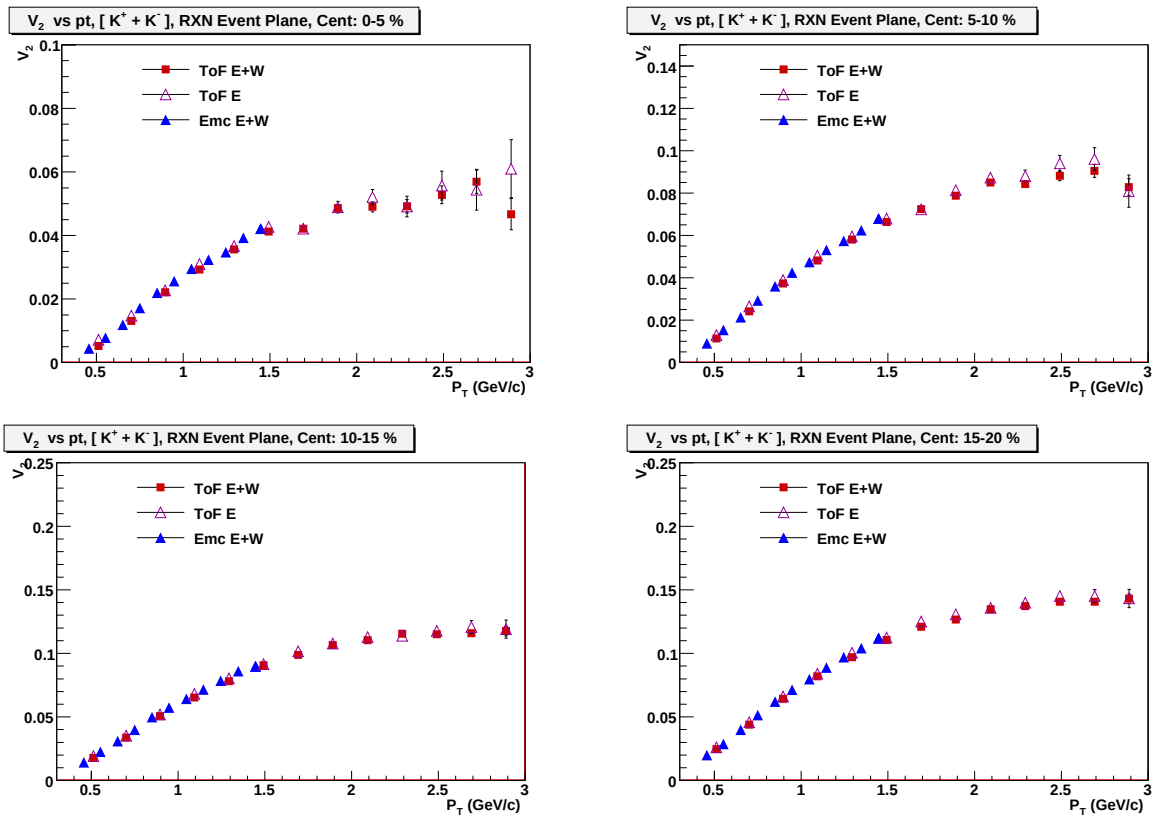


Figure 38: P_T dependence of elliptic flow of charged kaons [$K^+ + K^-$] measured with respect to the combined RXN event plane. Different symbols and colors correspond to the pions detected by time-of-flight method using TOF East, TOF WEST+EAST and EMC (PbSc) as indicated. The results are presented for different bins in reaction centrality as indicated in each panel.

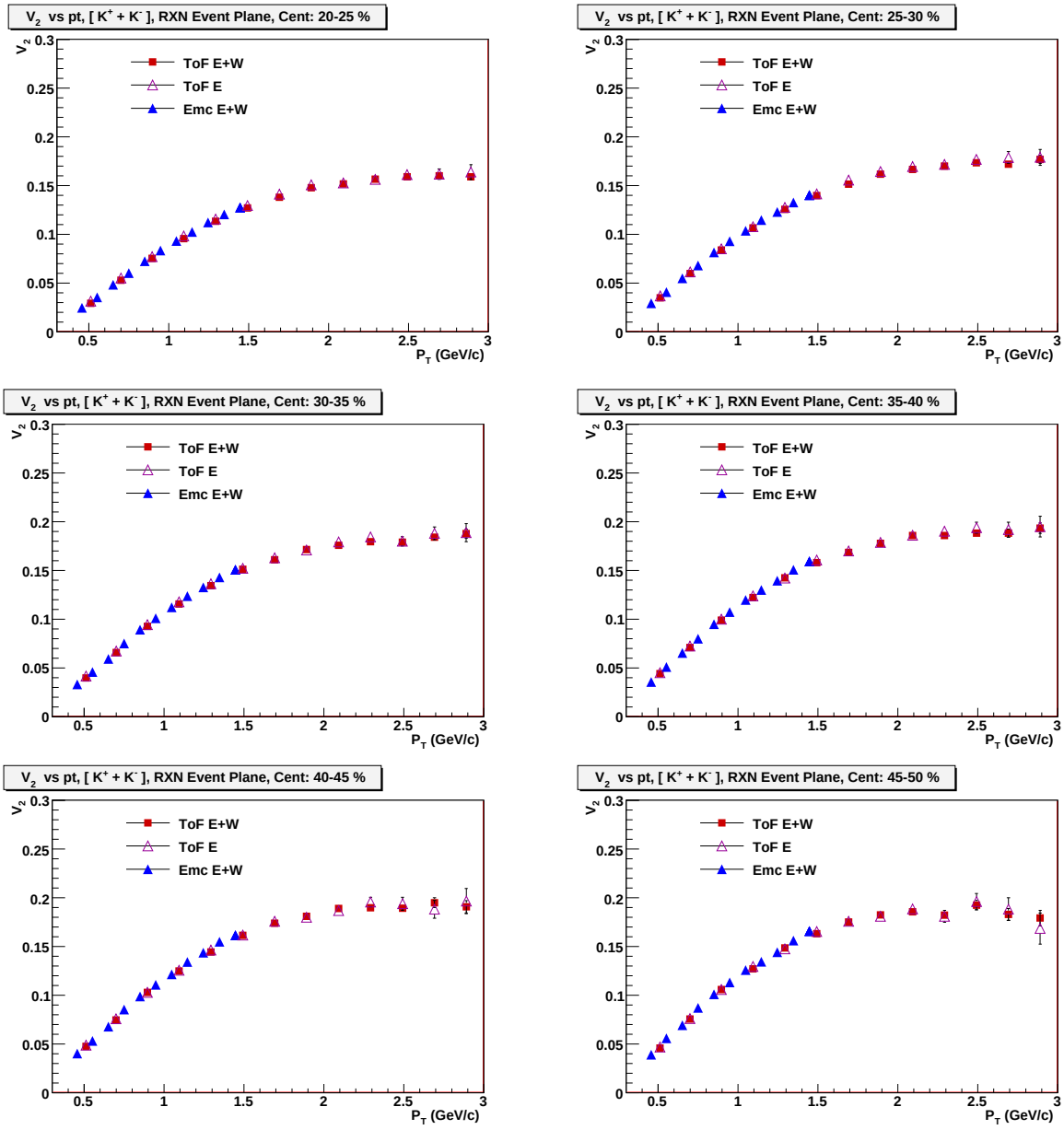


Figure 39: P_T dependence of elliptic flow of charged kaons [$K^+ + K^-$] measured with respect to the combined RXN event plane. Different symbols and colors correspond to the pions detected by time-of-flight method using TOF East, TOF WEST+EAST and EMC (PbSc) as indicated. The results are presented for different bins in reaction centrality as indicated in each panel.

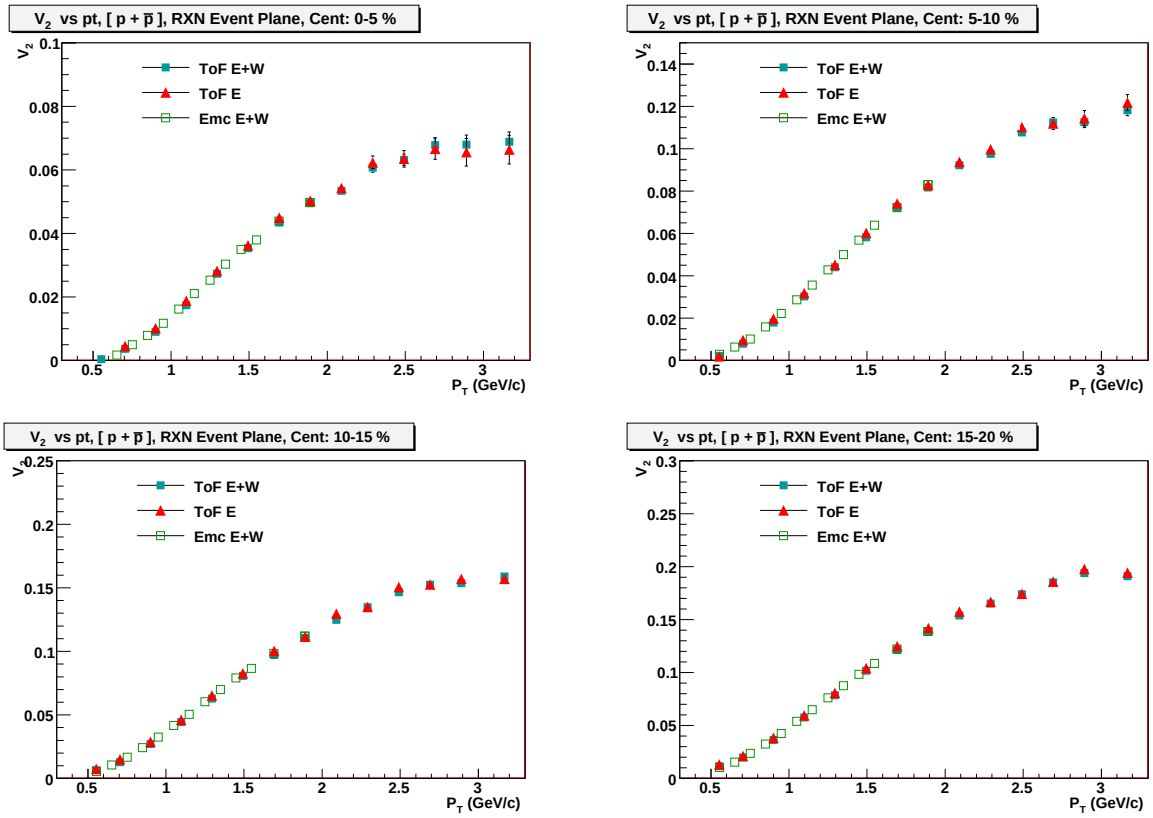


Figure 40: P_T dependence of elliptic flow of (anti-)protons $[p + \bar{p}\ ]$ measured with respect to the combined RXN event plane. Different symbols and colors correspond to the pions detected by time-of-flight method using TOF East, TOF WEST+EAST and EMC (PbSc) as indicated. The results are presented for different bins in reaction centrality as indicated in each panel.

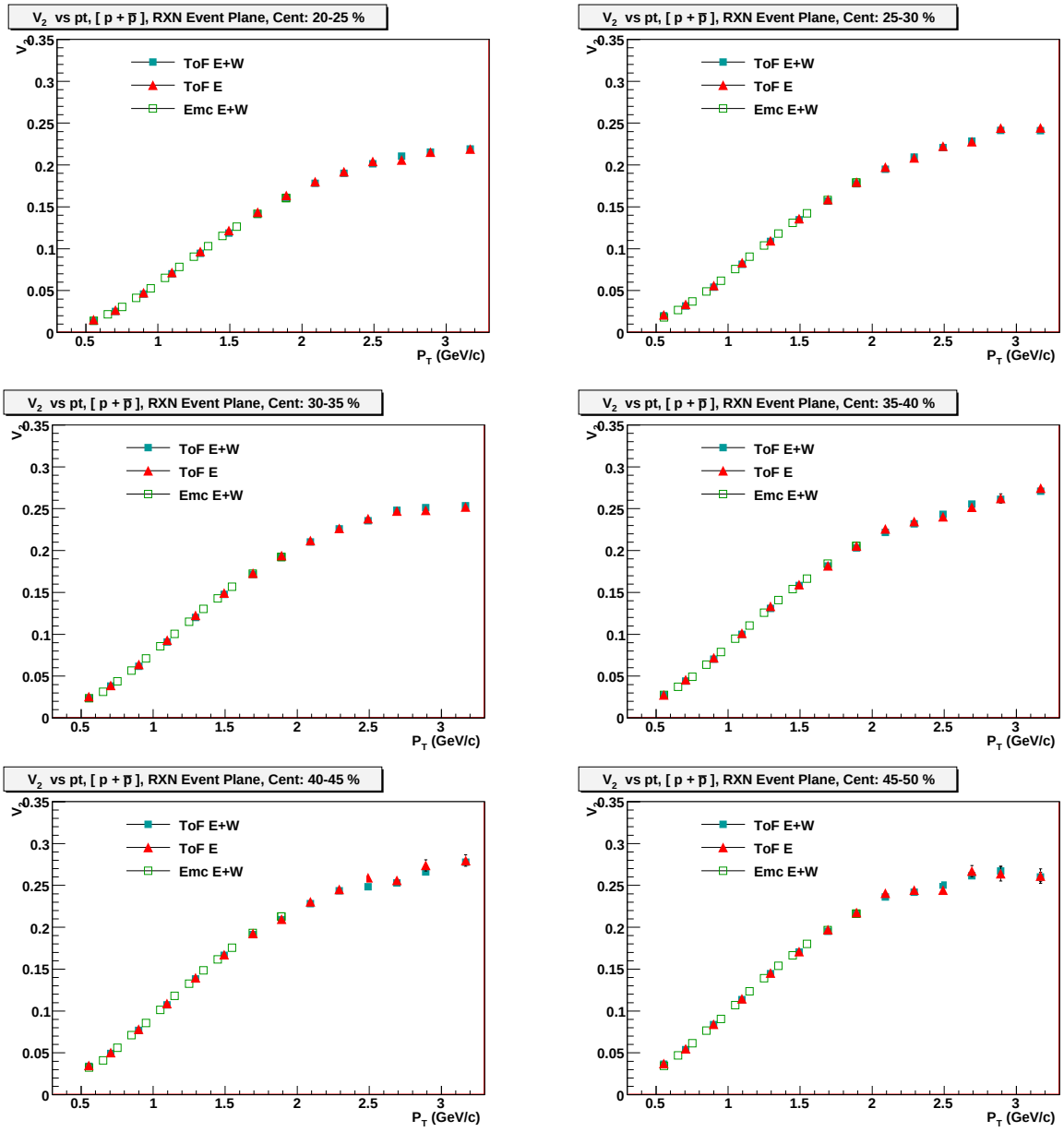


Figure 41: P_T dependence of elliptic flow of (anti-)protons [$p + \bar{p}$] measured with respect to the combined RXN event plane. Different symbols and colors correspond to the pions detected by time-of-flight method using TOF East, TOF WEST+EAST and EMC (PbSc) as indicated. The results are presented for different bins in reaction centrality as indicated in each panel.

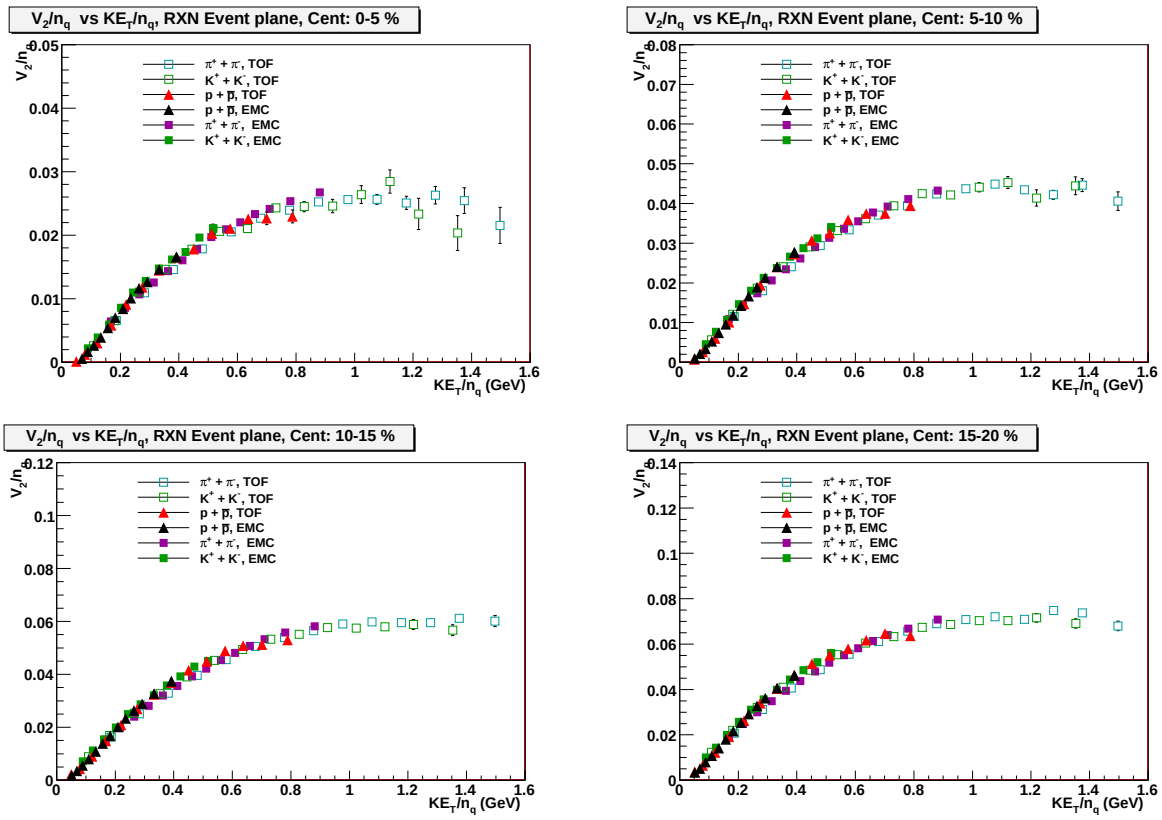


Figure 42: Transverse kinetic energy dependence of the scaled elliptic flow v_2/n_q of charged identified hadrons: charged pions $\pi^+ + \pi^-$, kaons and (anti-)protons measured with respect to the combined RXN event plane. Different symbols and colors correspond to the pions detected by time-of-flight method using TOF East, TOF WEST+EAST and EMC (PbSc) as indicated. The results are presented for different bins in reaction centrality as indicated in each panel.

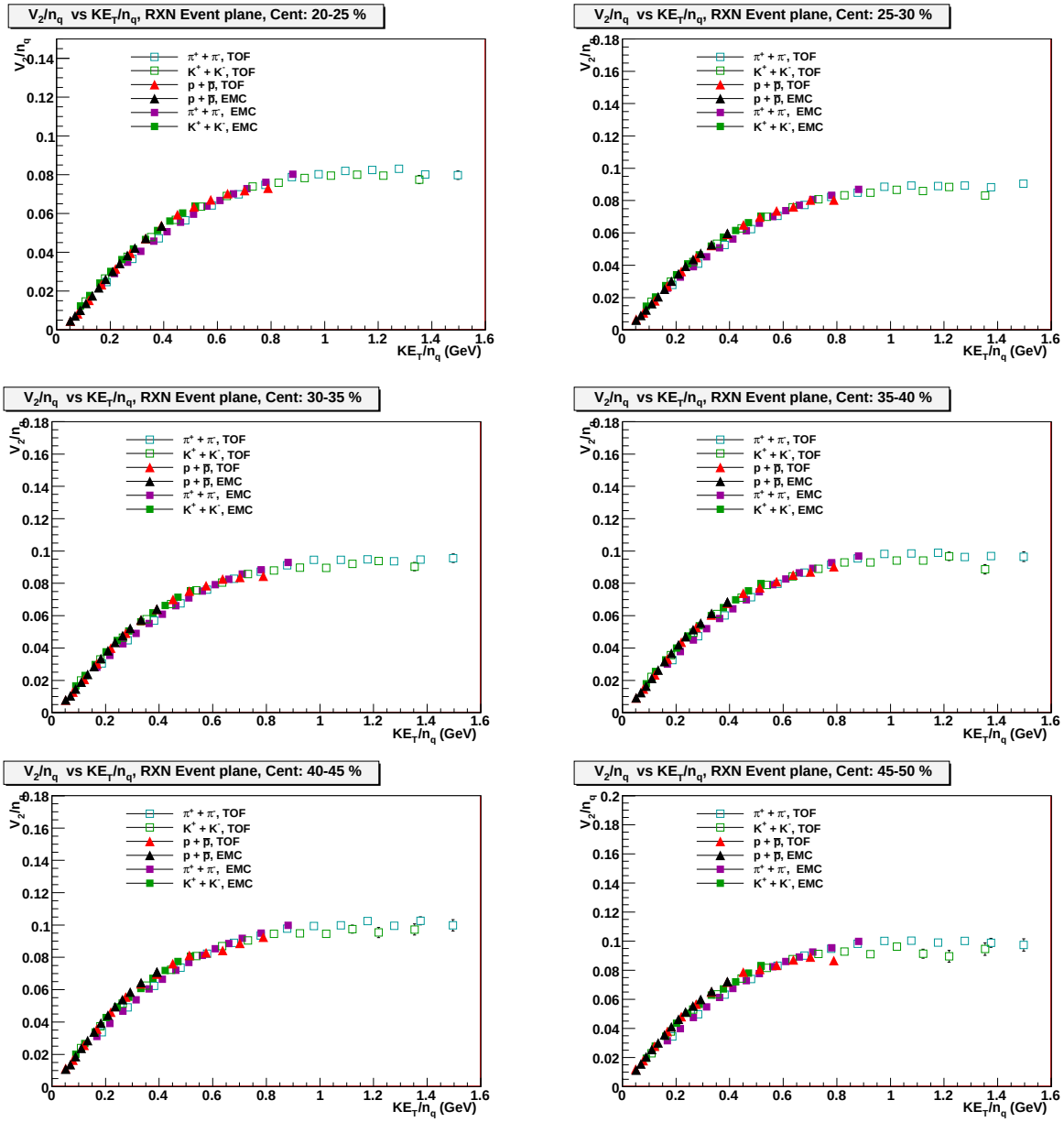


Figure 43: Transverse kinetic energy dependence of the scaled elliptic flow v_2/n_q of charged identified hadrons: charged pions $\pi^+ + \pi^-$, kaons and (anti-)protons measured with respect to the combined RXN event plane. Different symbols and colors correspond to the pions detected by time-of-flight method using TOF East, TOF WEST+EAST and EMC (PbSc) as indicated. The results are presented for different bins in reaction centrality as indicated in each panel..

8 Detailed check of PID functions

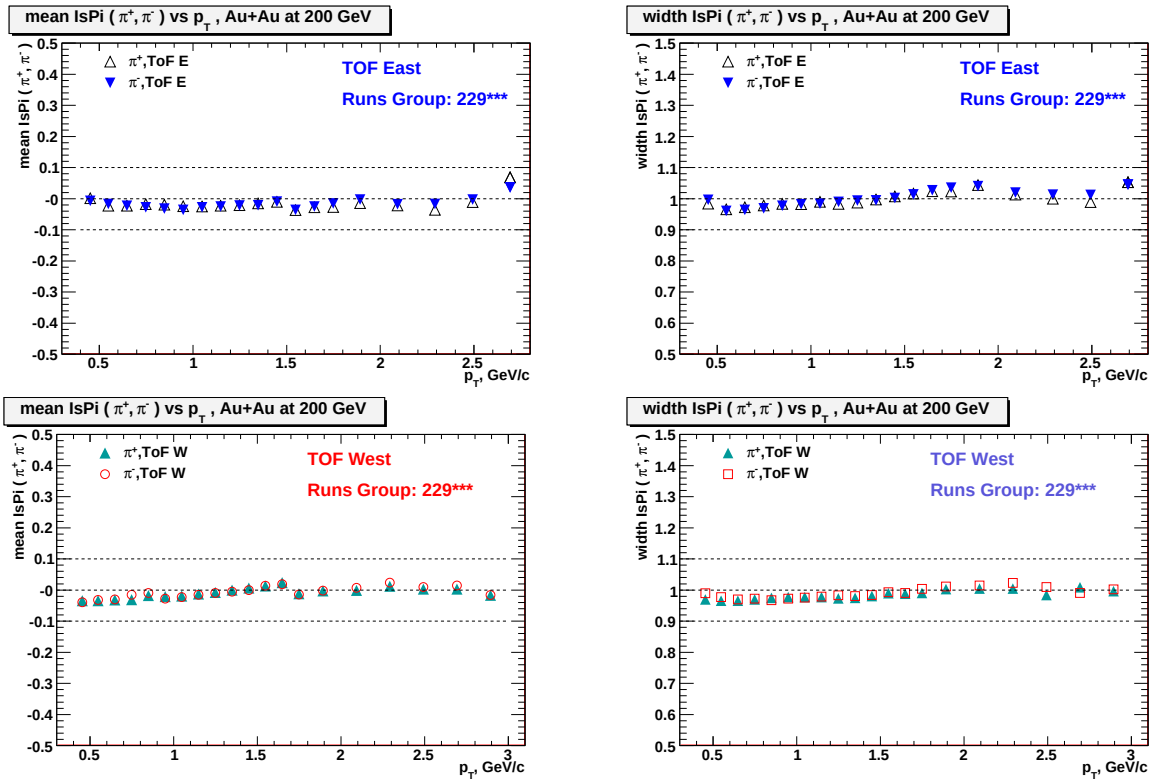


Figure 44: Mean/Sigma of IsPion as a function of p_T

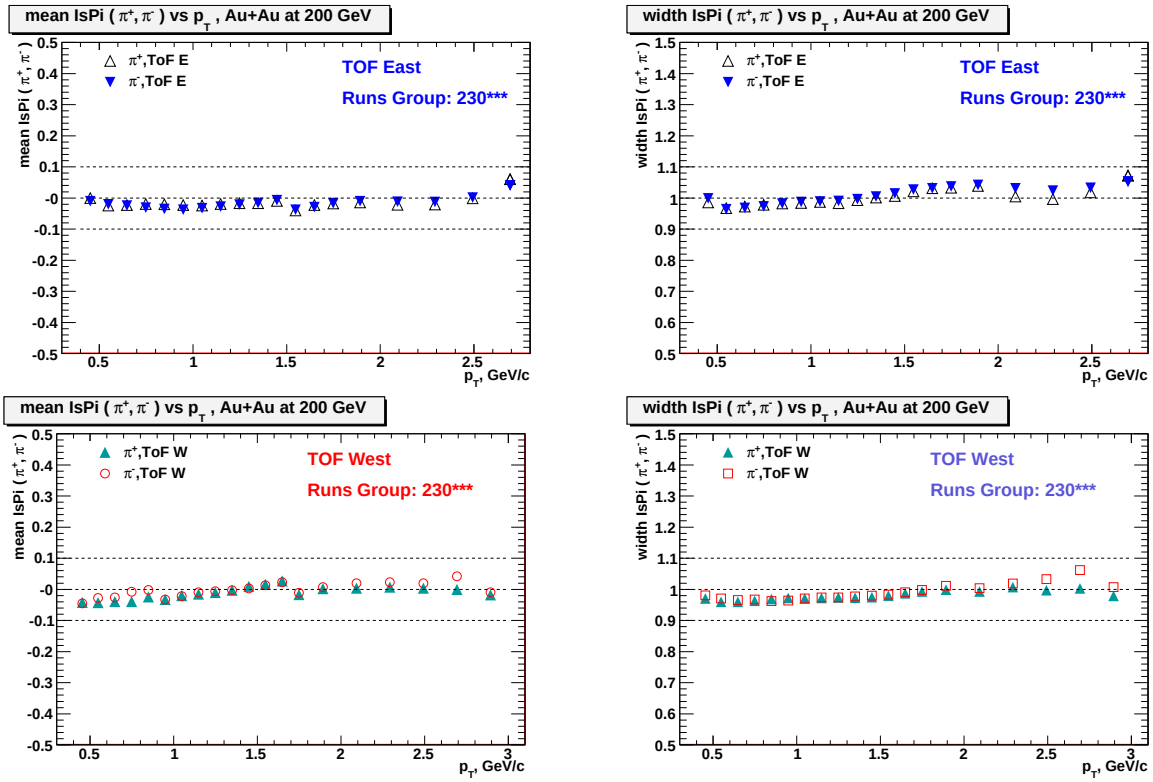


Figure 45: Mean/Sigma of IsPion as a function of p_T

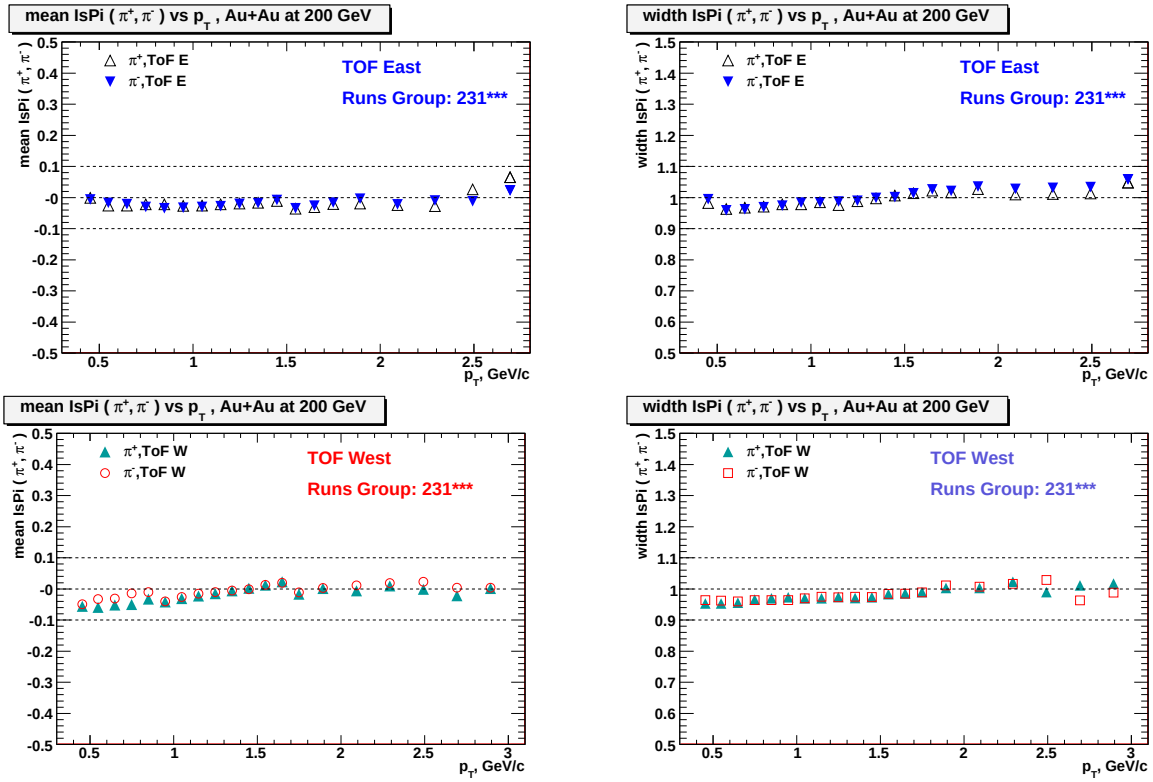


Figure 46: Mean/Sigma of IsPion as a function of p_T

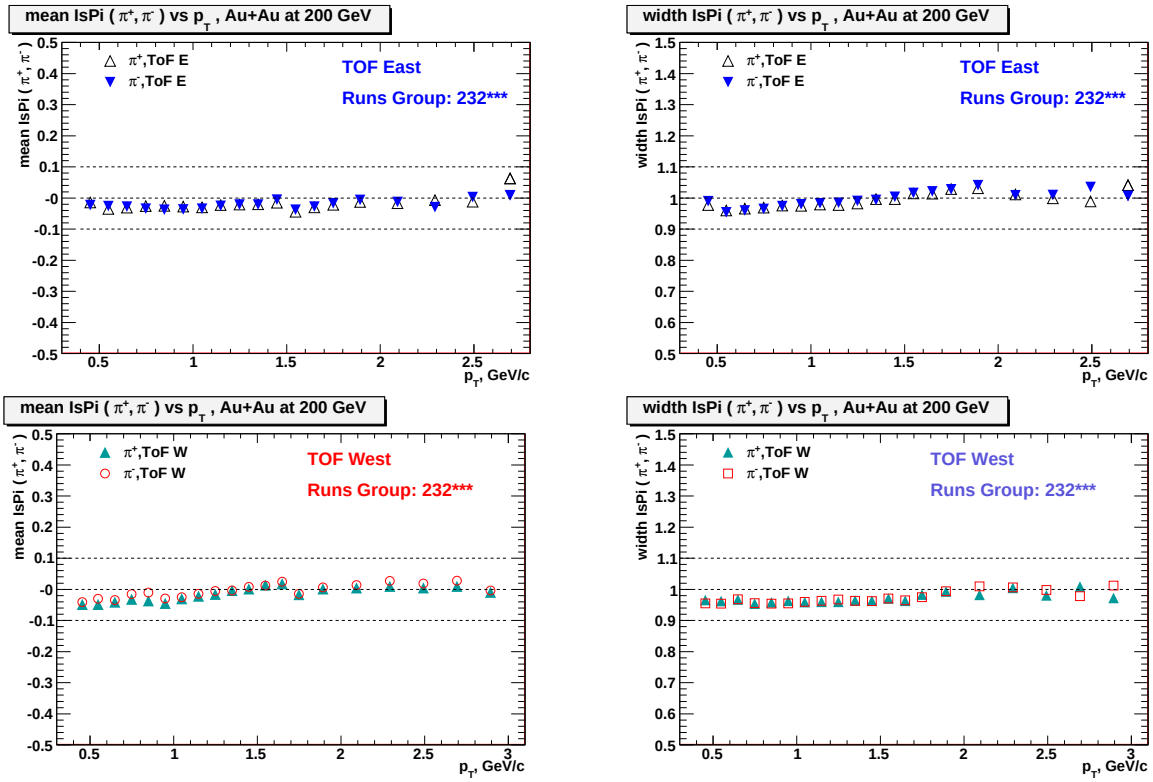


Figure 47: Mean/Sigma of IsPion as a function of p_T

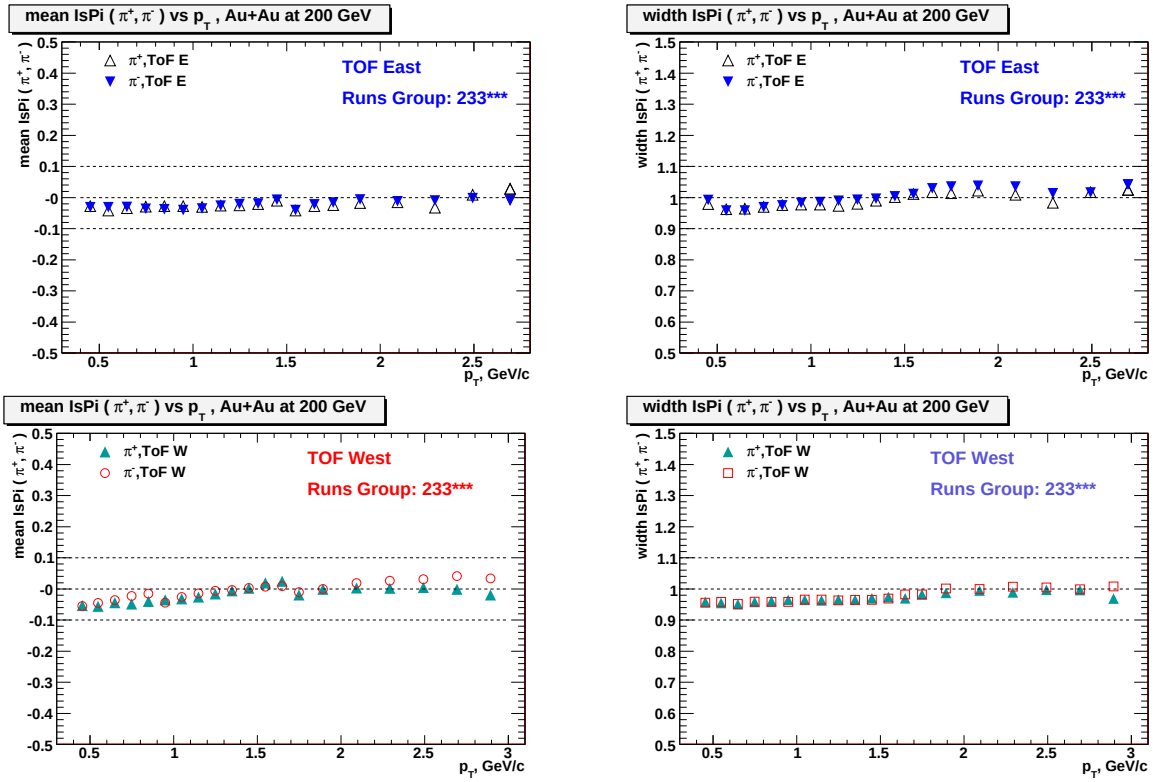


Figure 48: Mean/Sigma of IsPion as a function of p_T

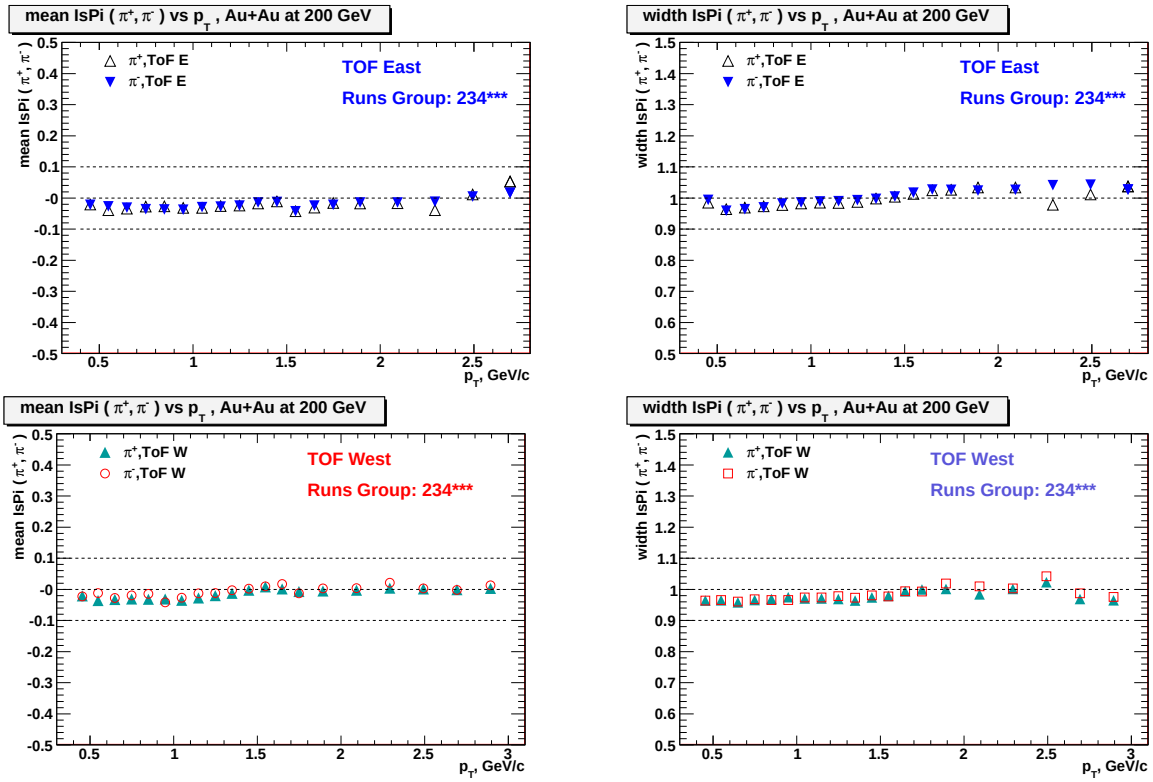


Figure 49: Mean/Sigma of IsPion as a function of p_T

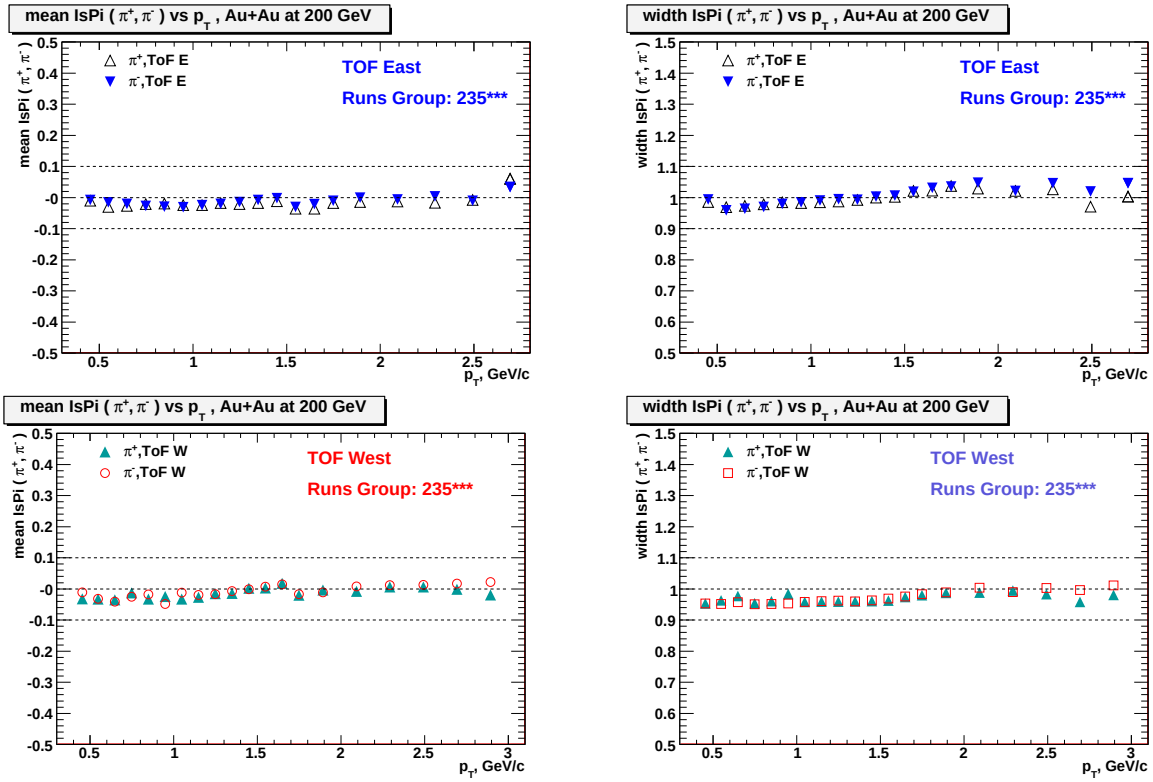


Figure 50: Mean/Sigma of IsPion as a function of p_T

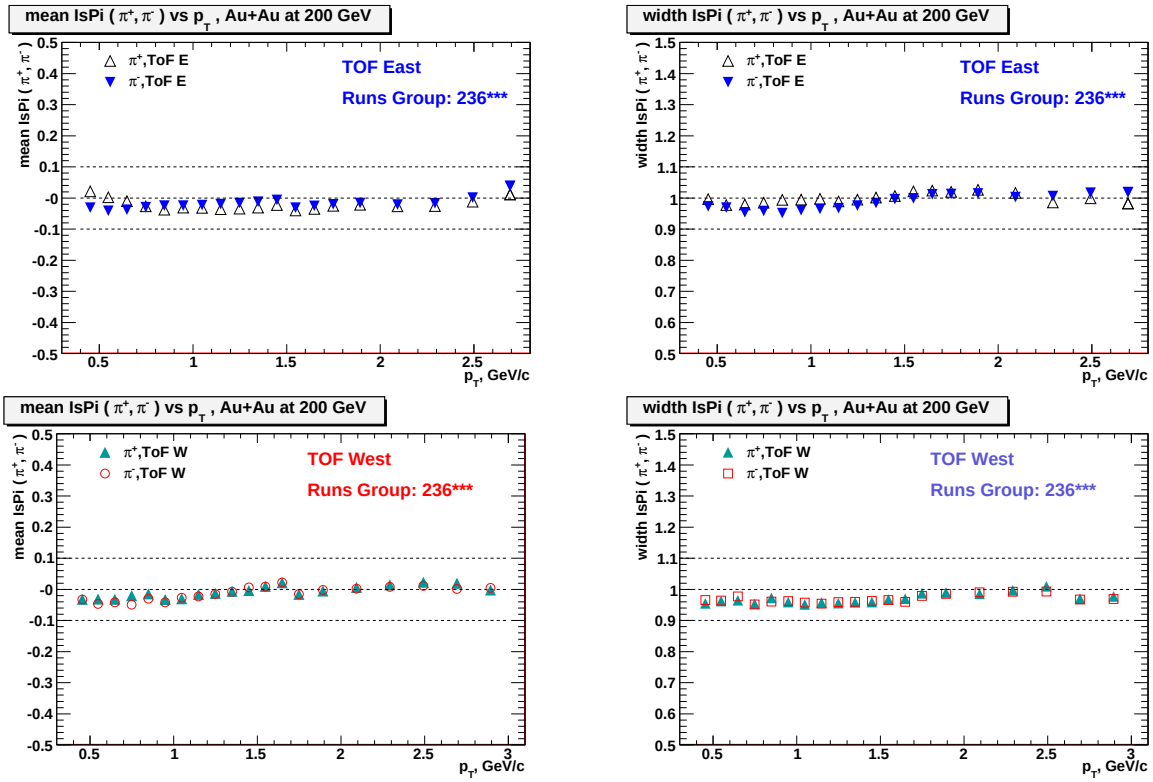


Figure 51: Mean/Sigma of IsPion as a function of p_T

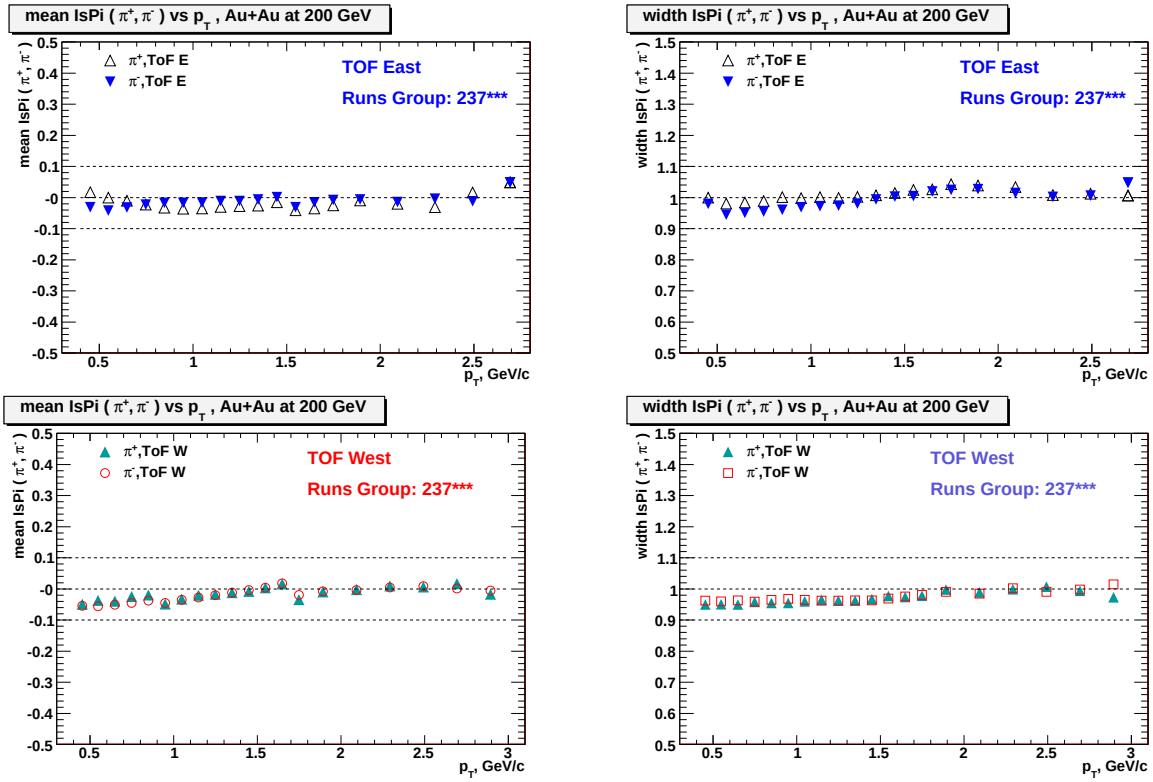


Figure 52: Mean/Sigma of IsPion as a function of p_T

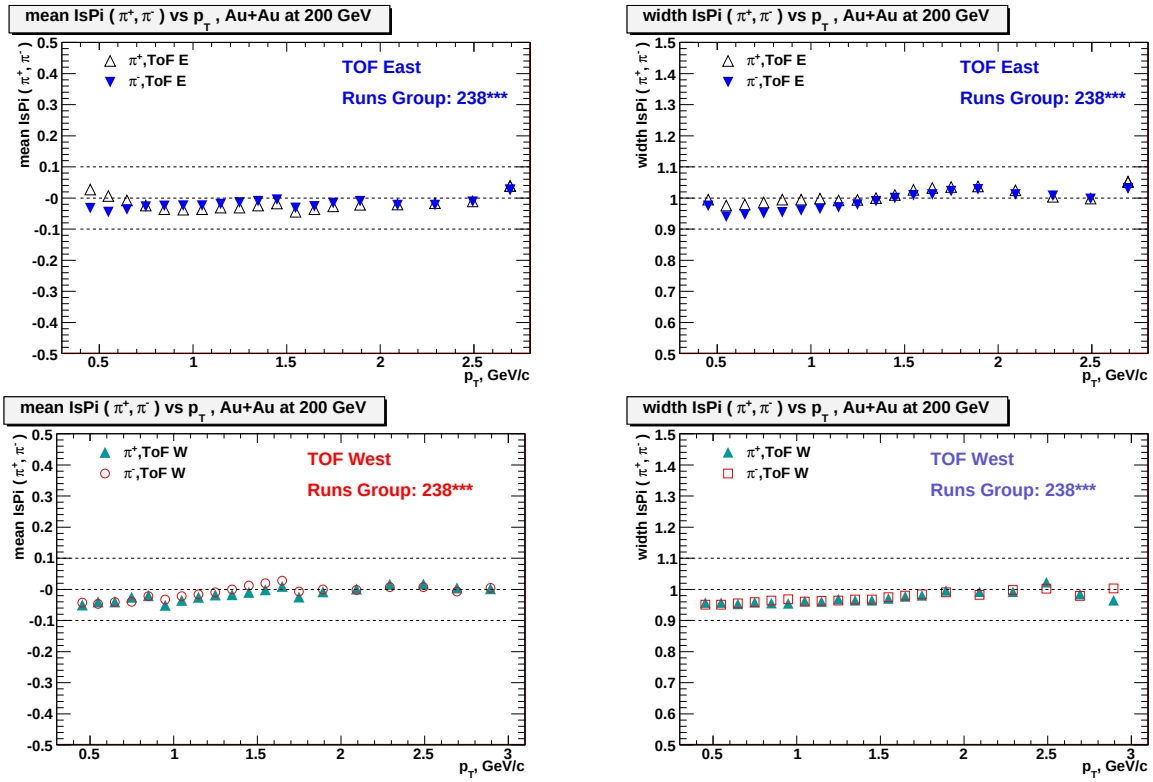


Figure 53: Mean/Sigma of IsPion as a function of p_T

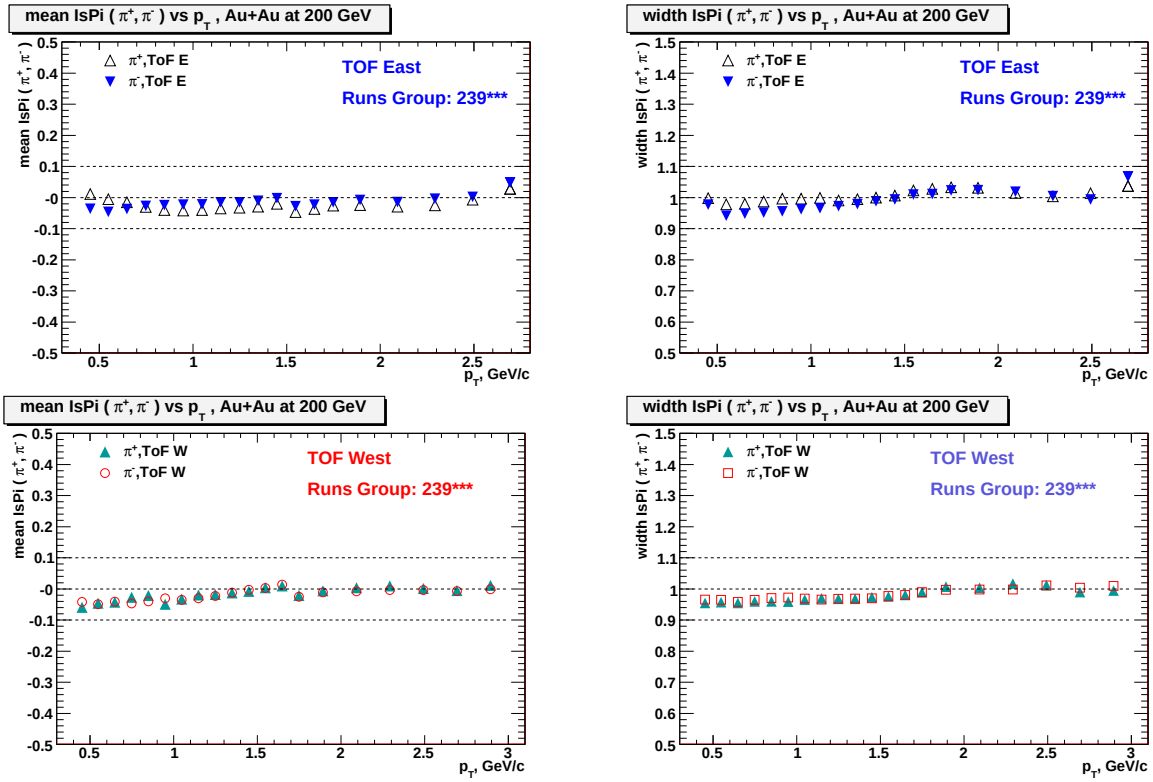


Figure 54: Mean/Sigma of IsPion as a function of p_T

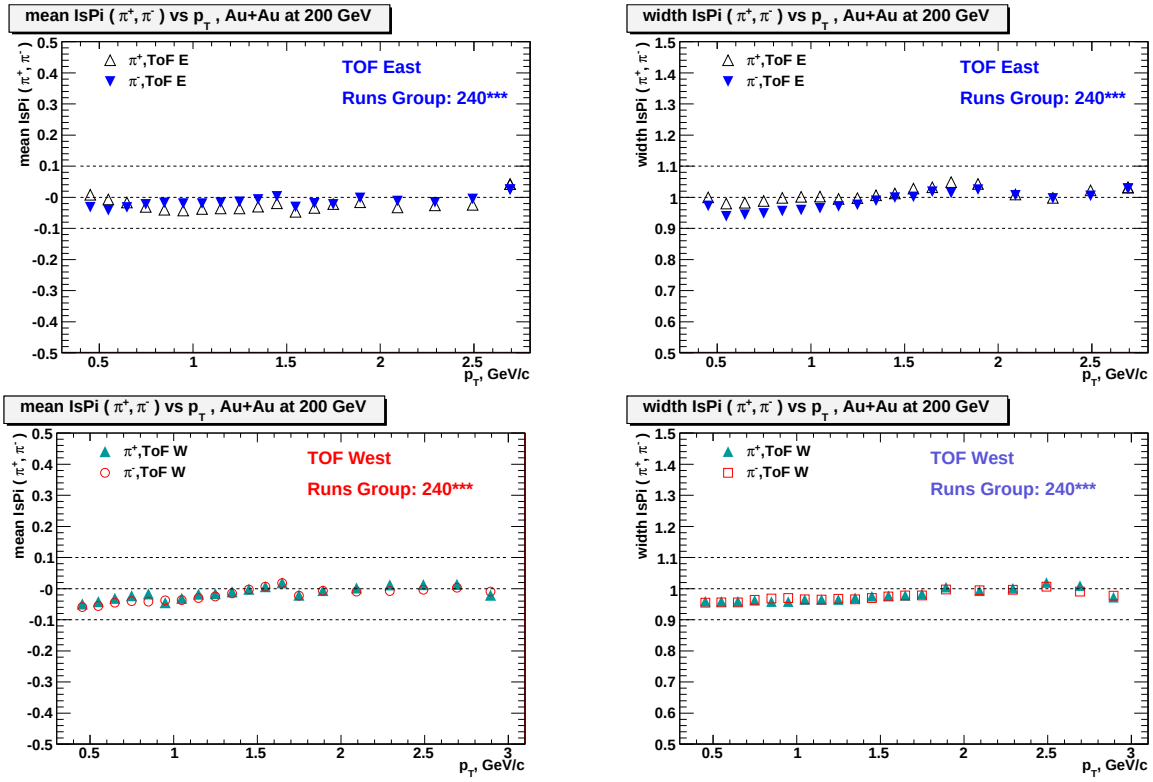


Figure 55: Mean/Sigma of IsPion as a function of p_T

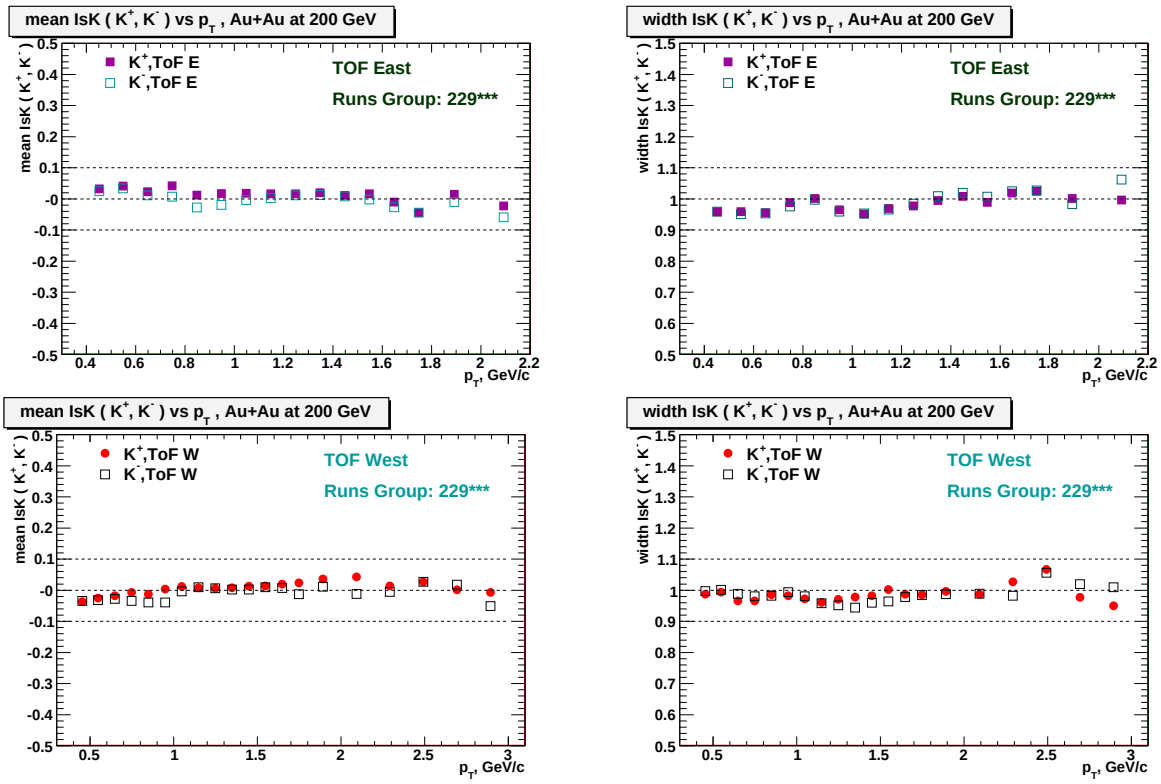


Figure 56: Mean/Sigma of IsKaon as a function of p_T

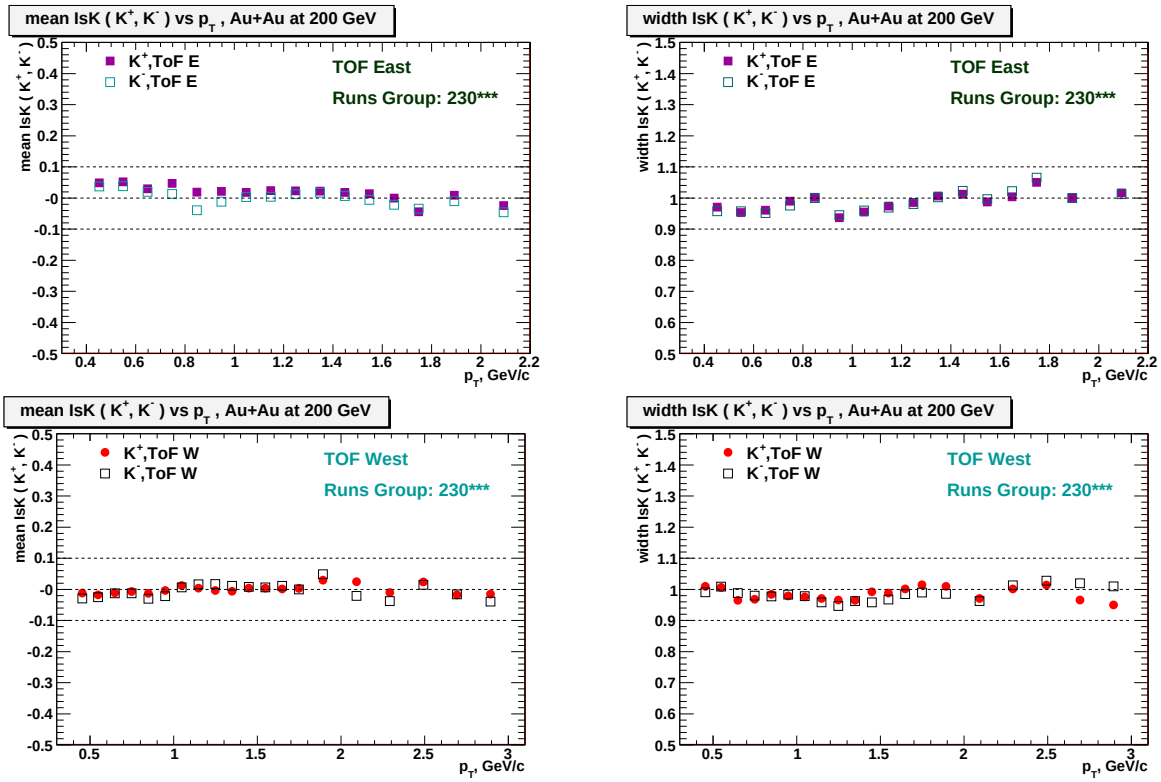


Figure 57: Mean/Sigma of IsKaon as a function of p_T

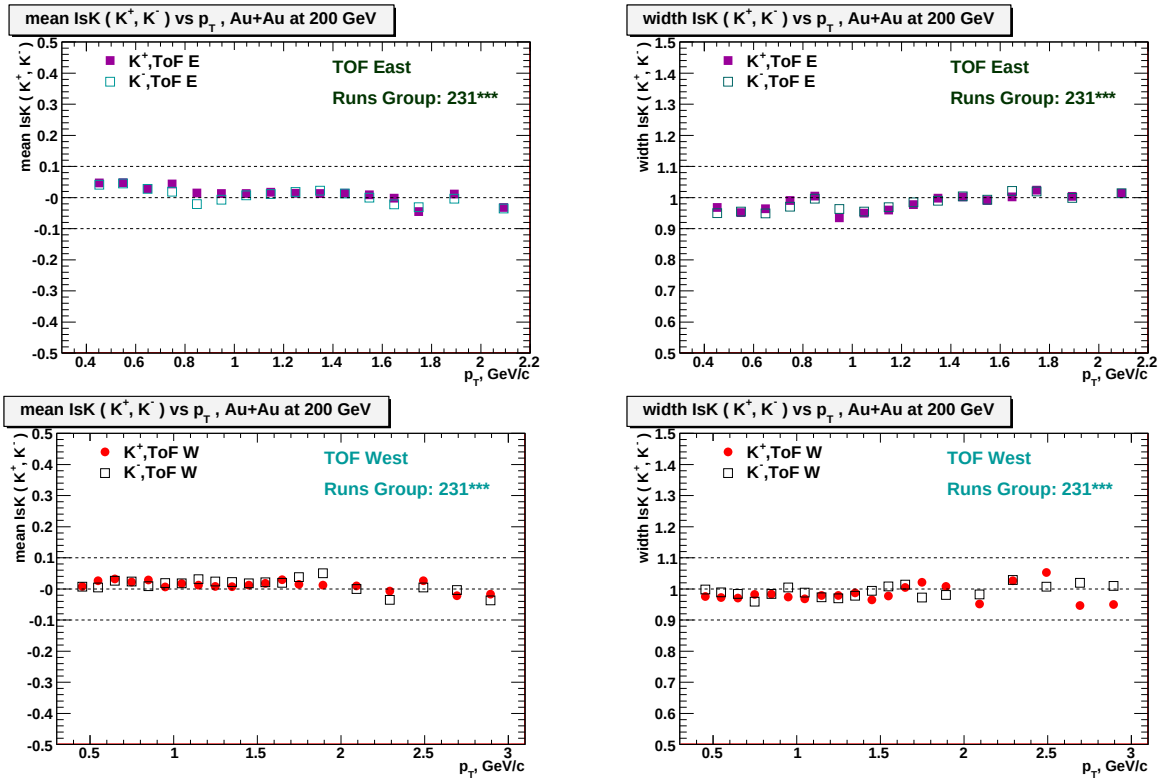


Figure 58: Mean/Sigma of IsKaon as a function of p_T

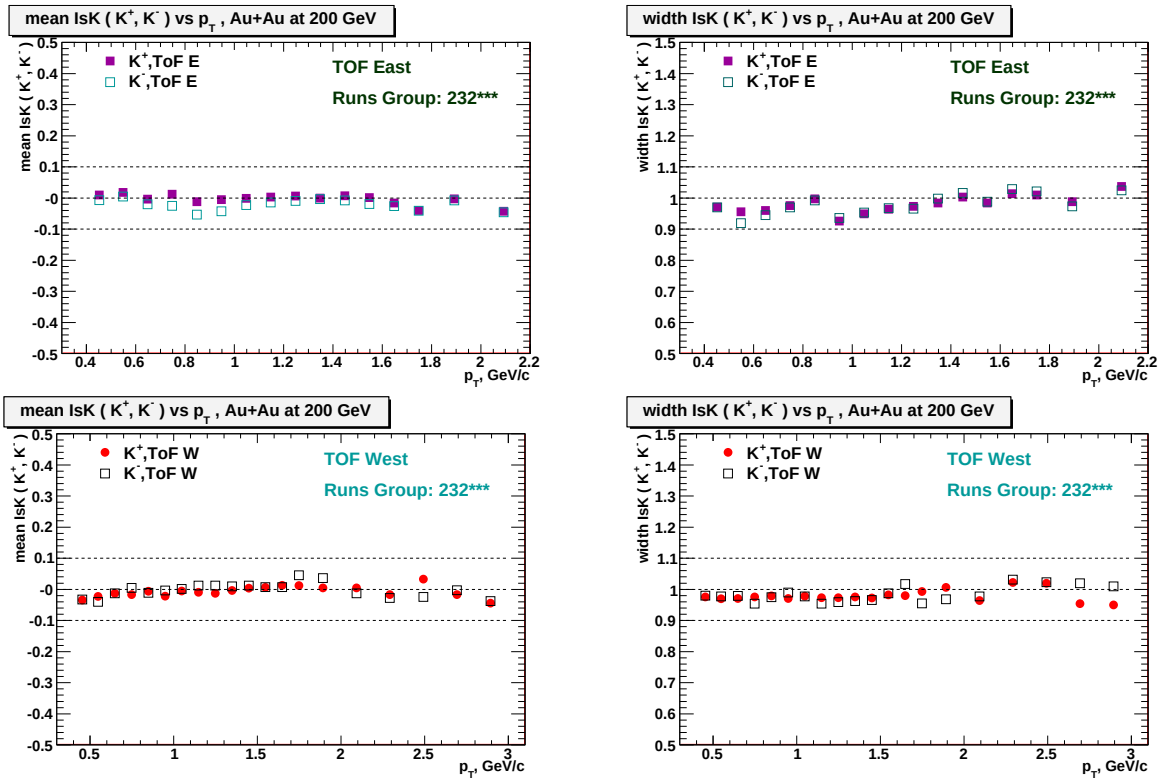


Figure 59: Mean/Sigma of IsKaon as a function of p_T

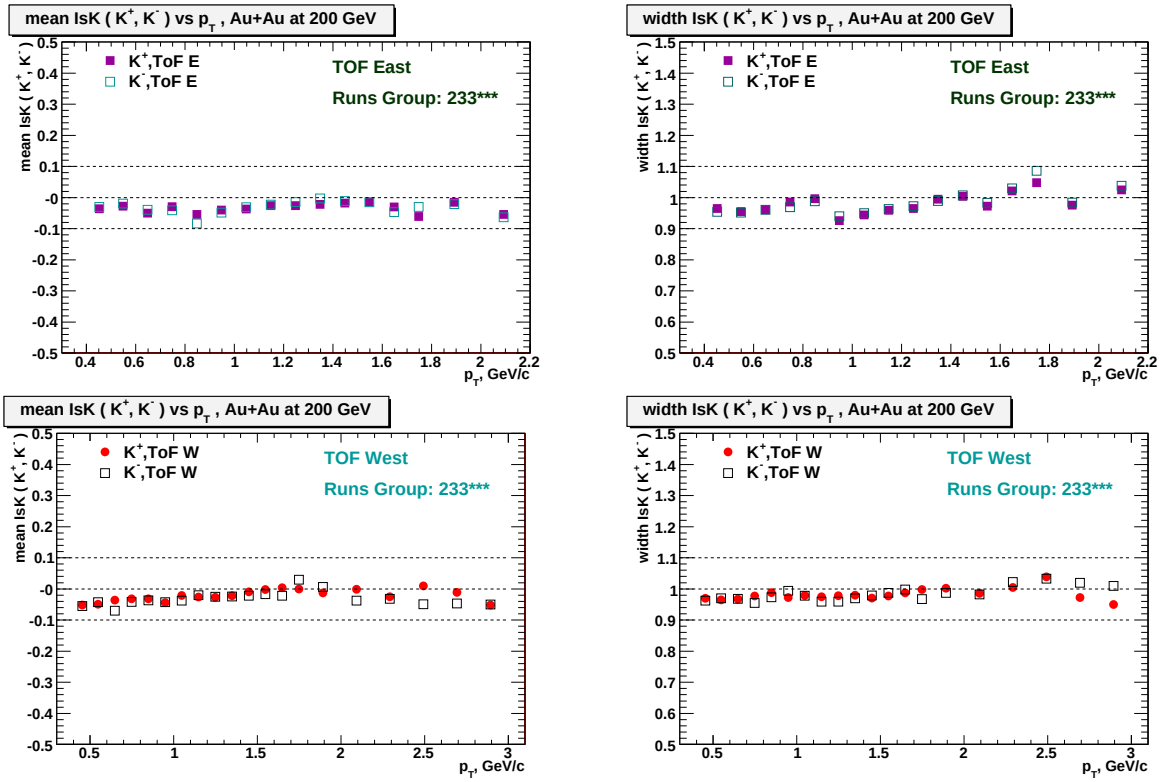


Figure 60: Mean/Sigma of IsKaon as a function of p_T

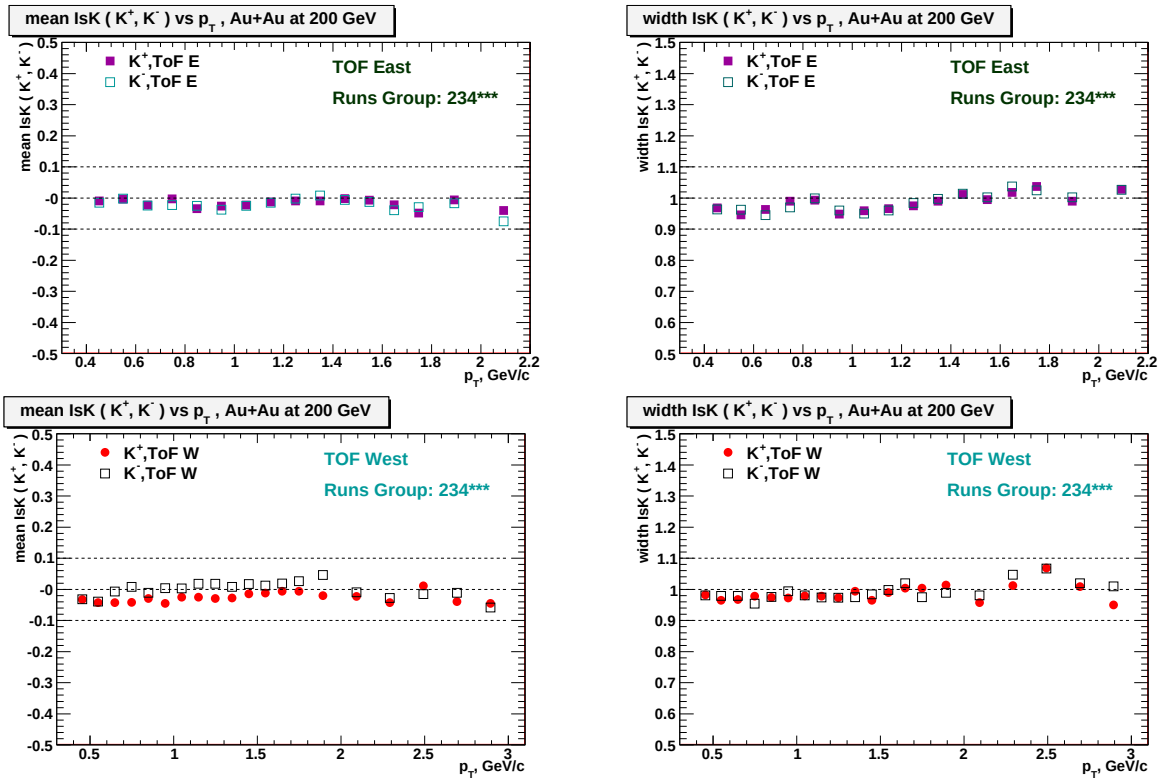


Figure 61: Mean/Sigma of IsKaon as a function of p_T

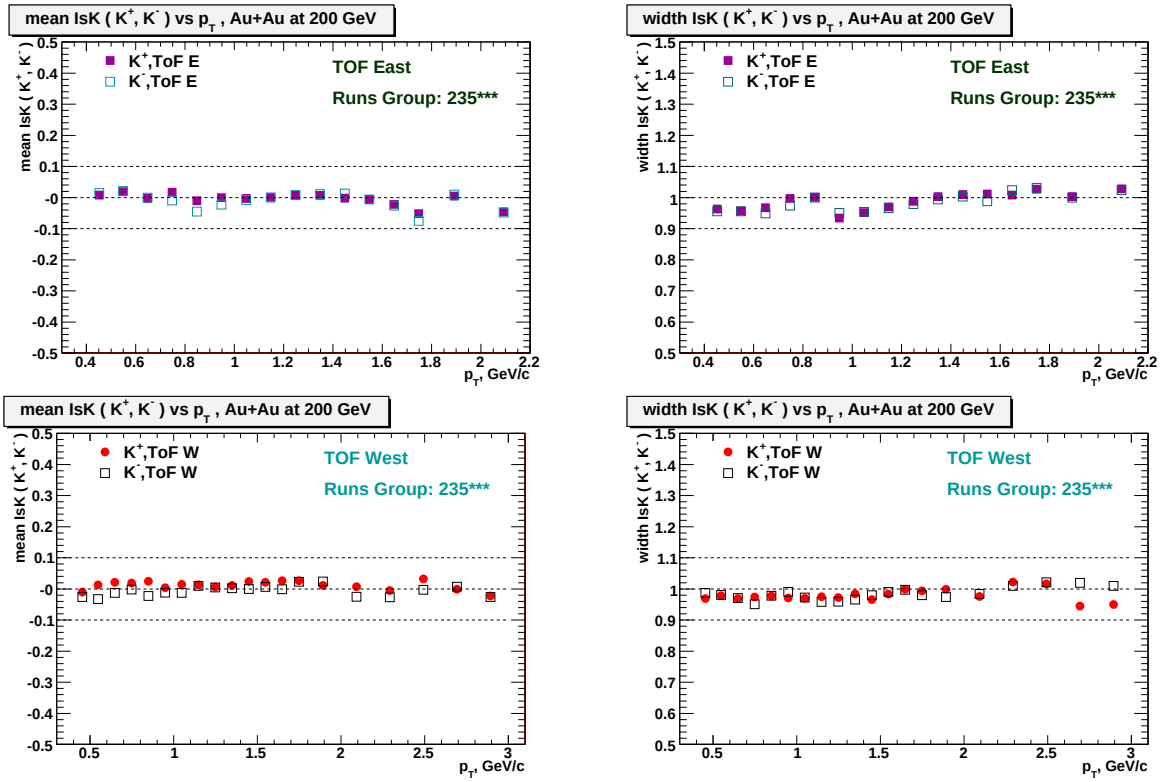


Figure 62: Mean/Sigma of IsKaon as a function of p_T

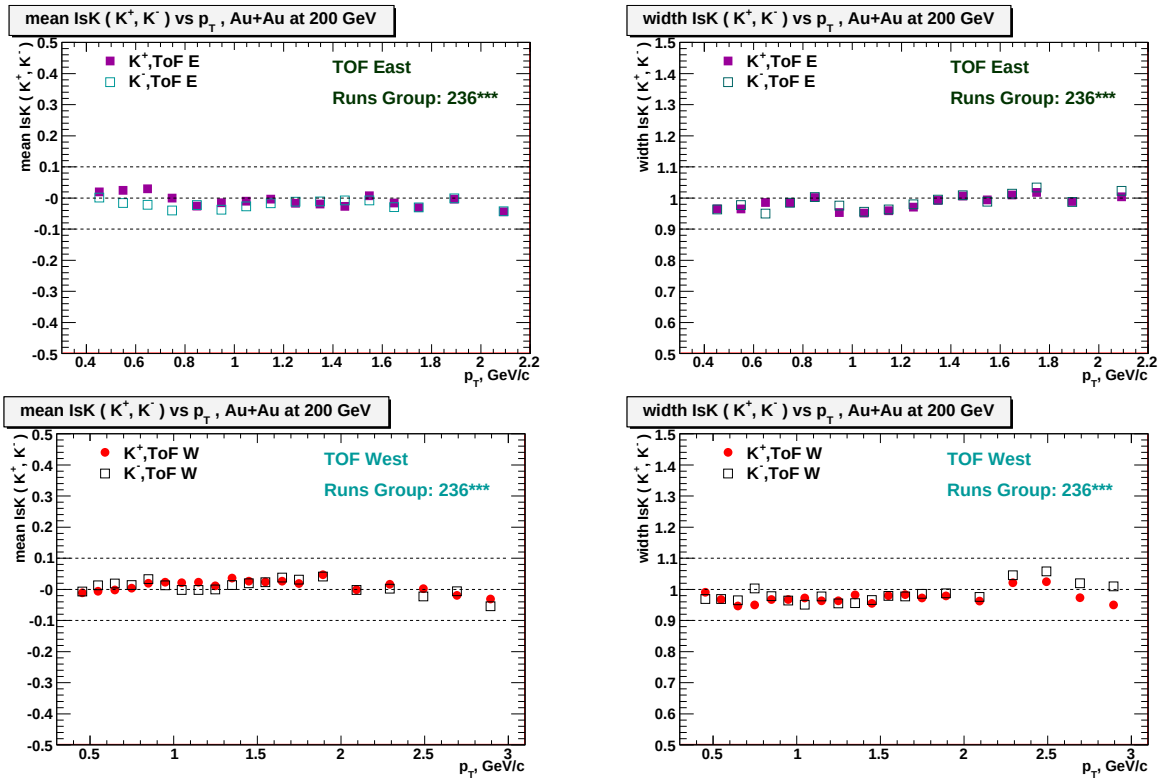


Figure 63: Mean/Sigma of IsKaon as a function of p_T

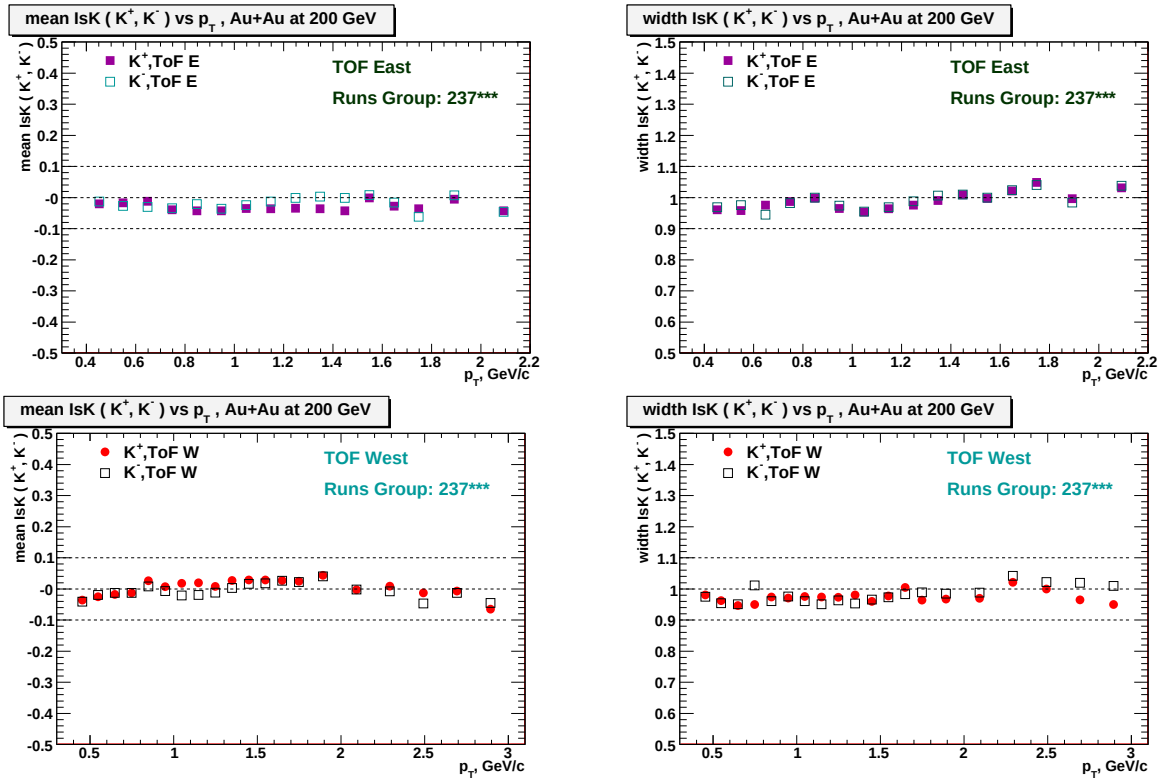


Figure 64: Mean/Sigma of IsKaon as a function of p_T

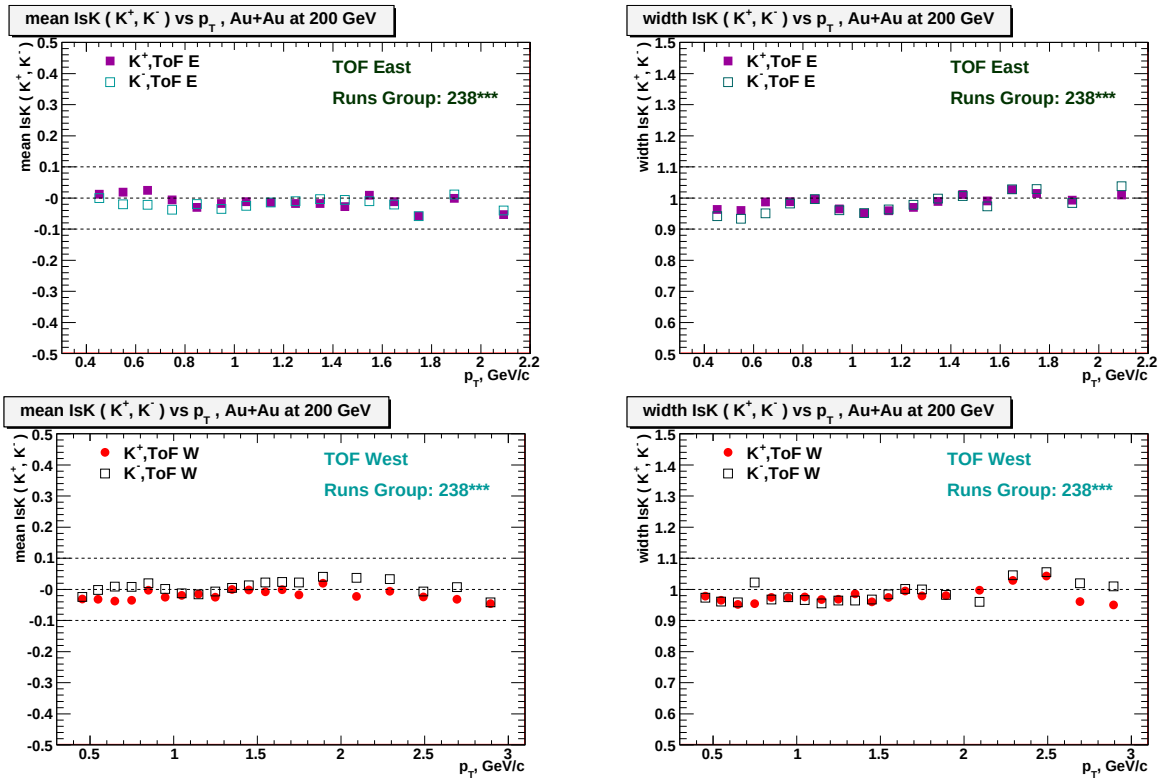


Figure 65: Mean/Sigma of IsKaon as a function of p_T

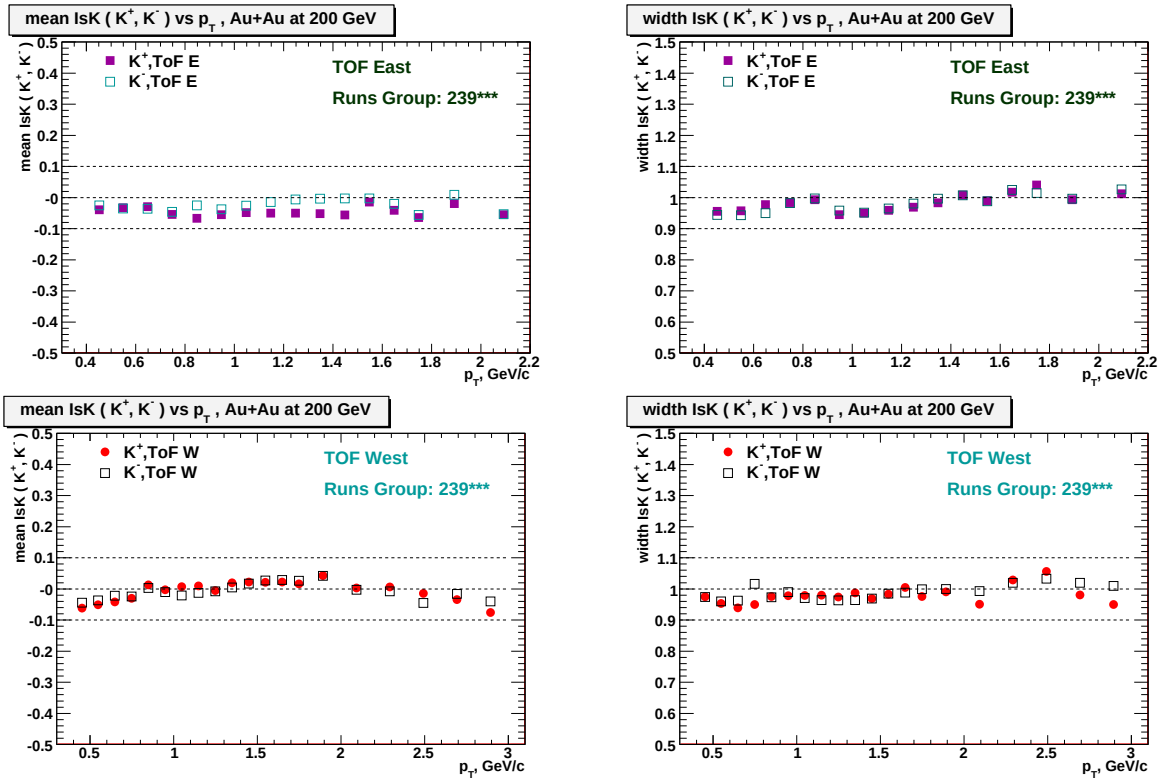


Figure 66: Mean/Sigma of IsKaon as a function of p_T

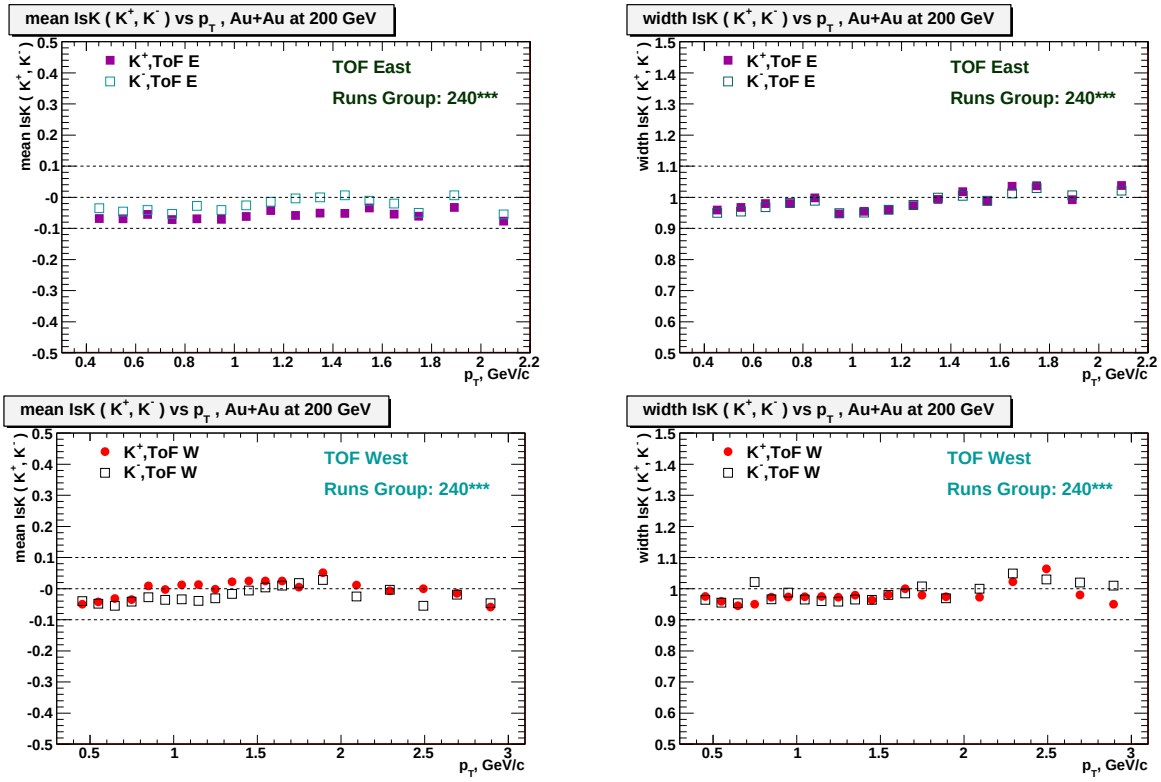


Figure 67: Mean/Sigma of IsKaon as a function of p_T

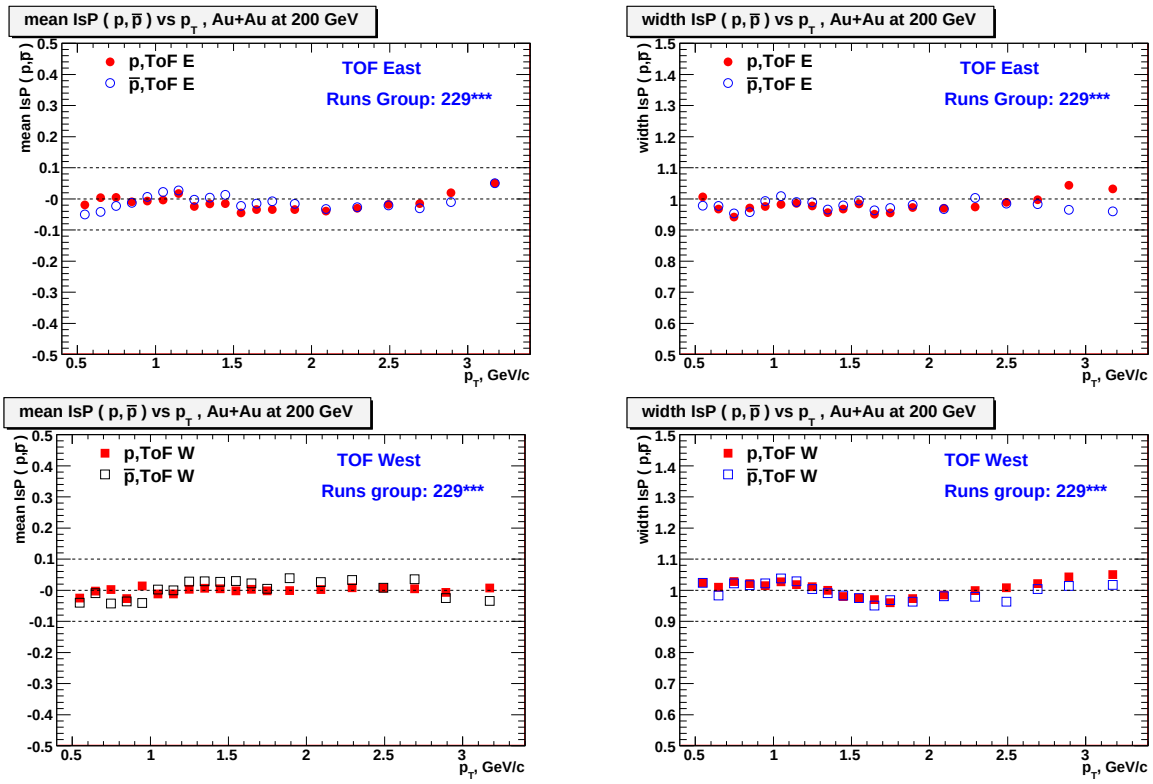


Figure 68: Mean/Sigma of IsProton as a function of p_T

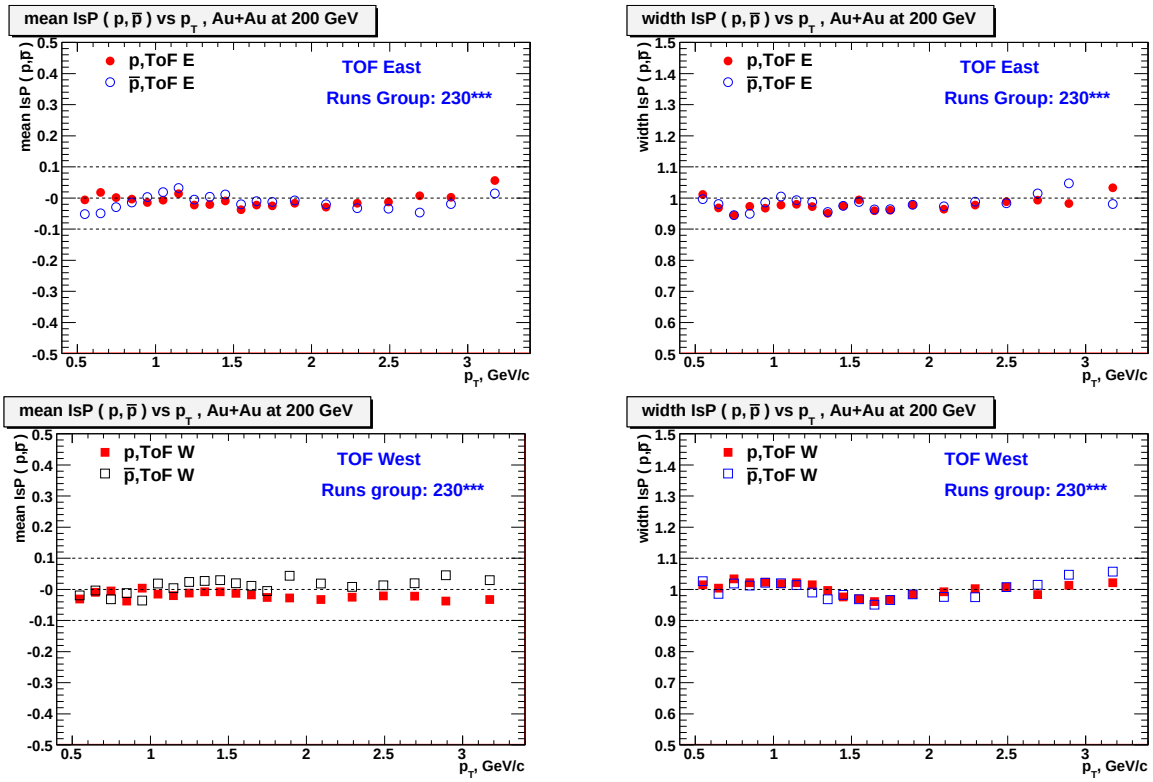


Figure 69: Mean/Sigma of IsProton as a function of p_T

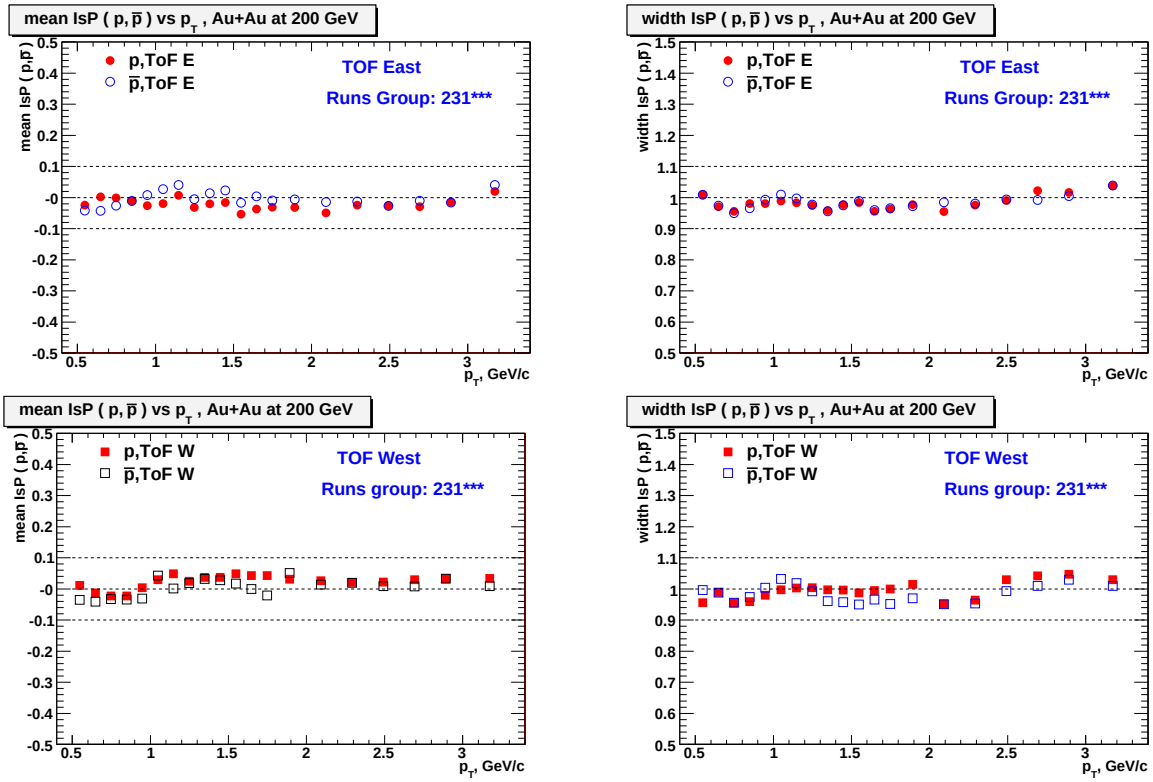


Figure 70: Mean/Sigma of IsProton as a function of p_T

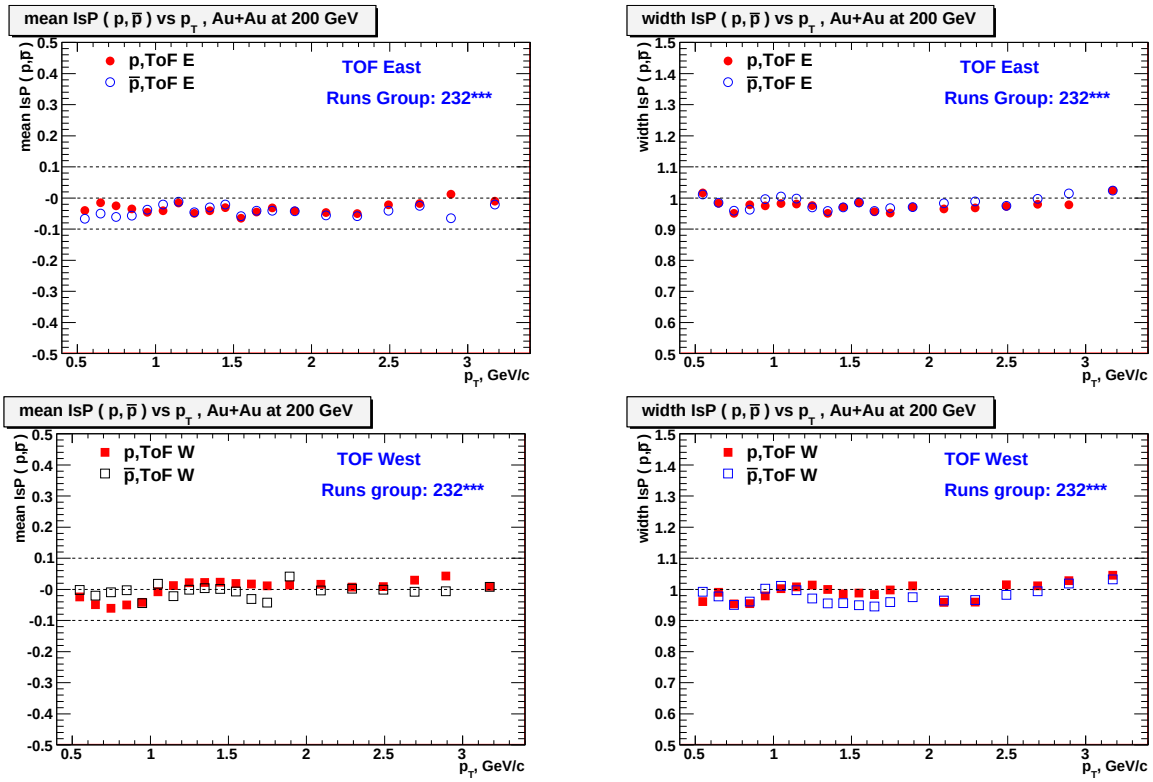


Figure 71: Mean/Sigma of IsProton as a function of p_T

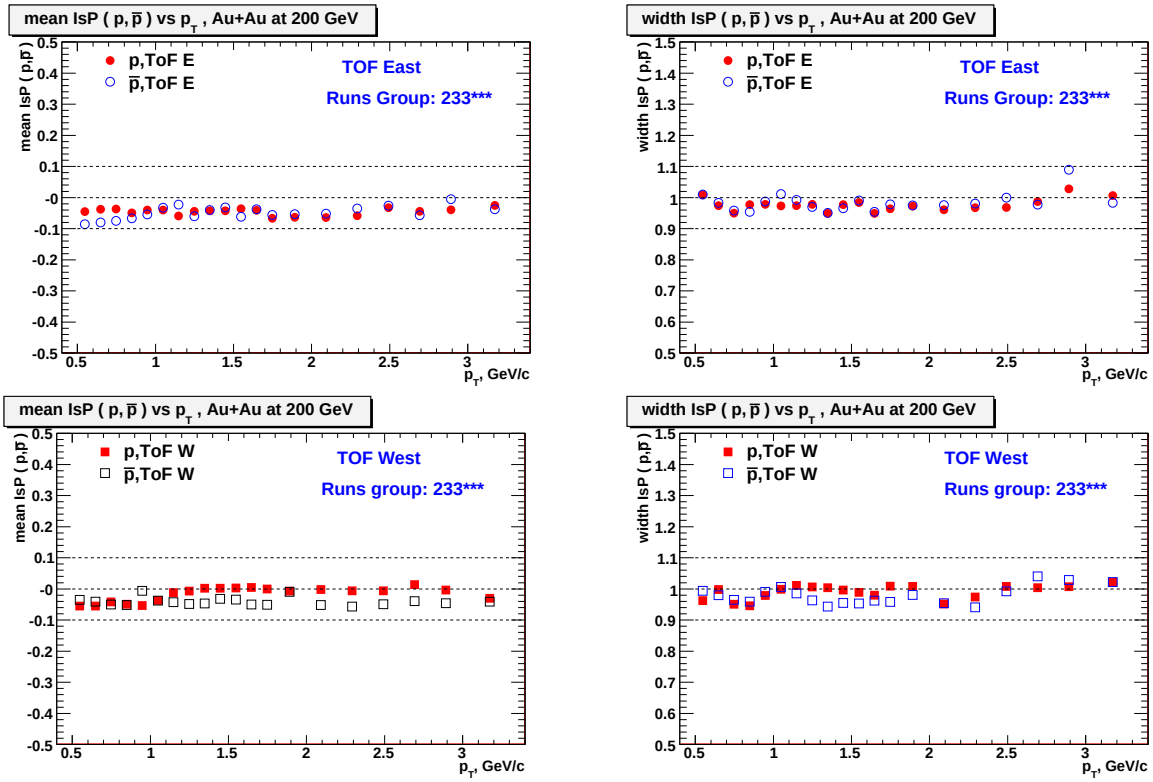


Figure 72: Mean/Sigma of IsProton as a function of p_T

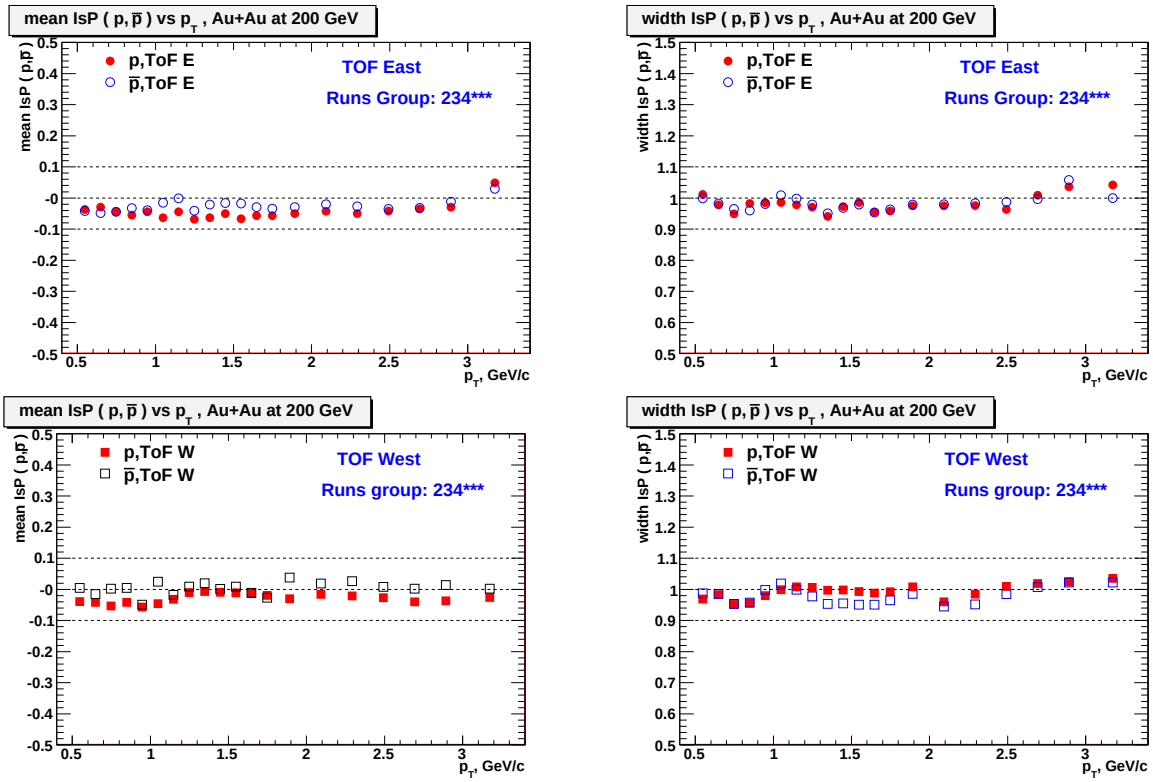


Figure 73: Mean/Sigma of IsProton as a function of p_T

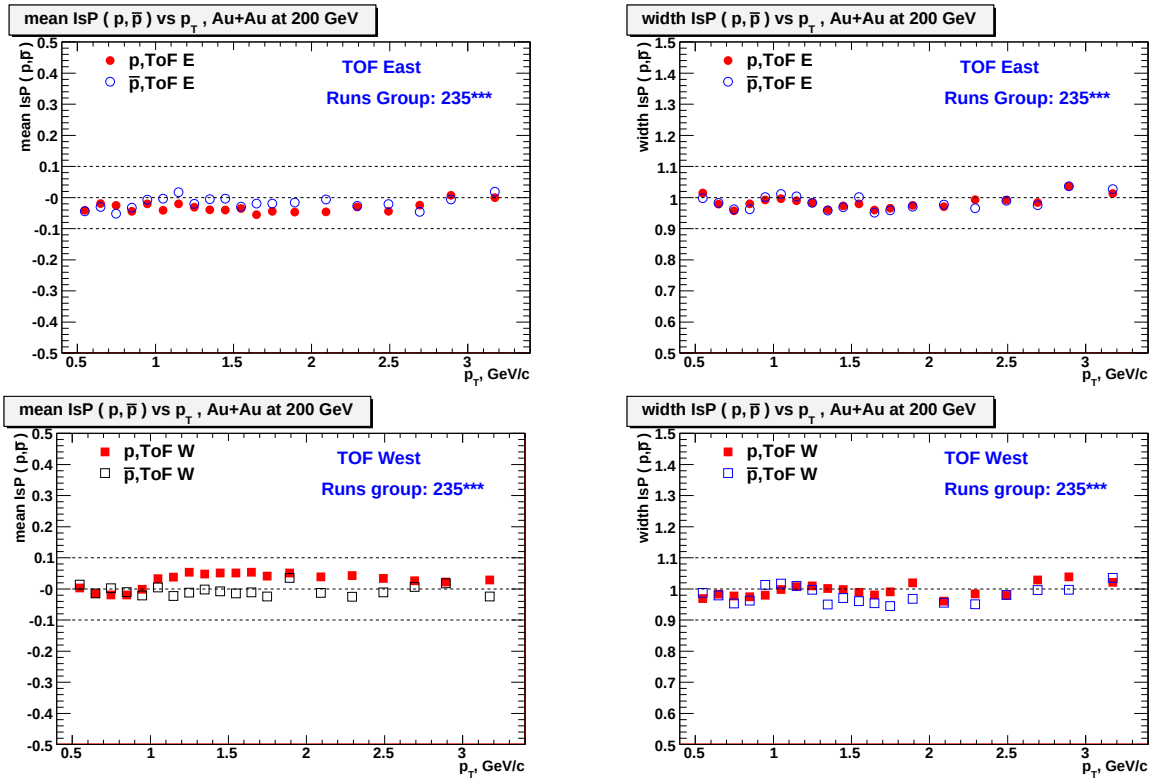


Figure 74: Mean/Sigma of IsProton as a function of p_T

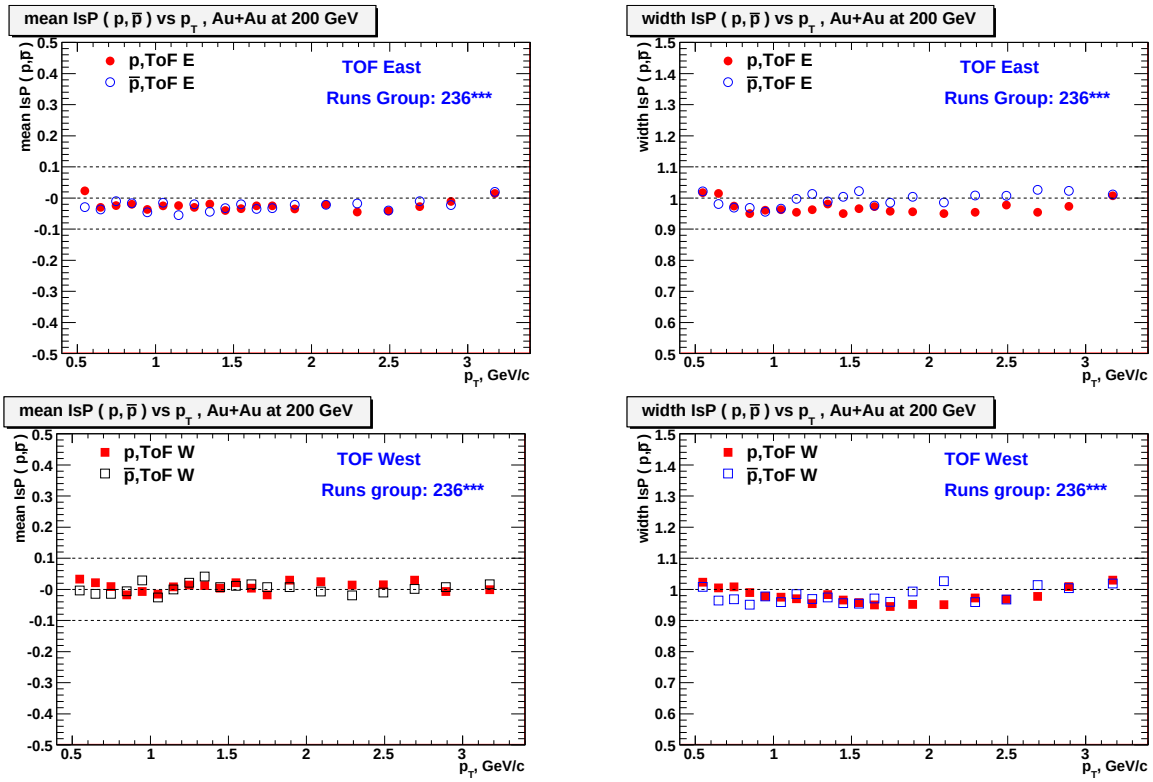


Figure 75: Mean/Sigma of IsProton as a function of p_T

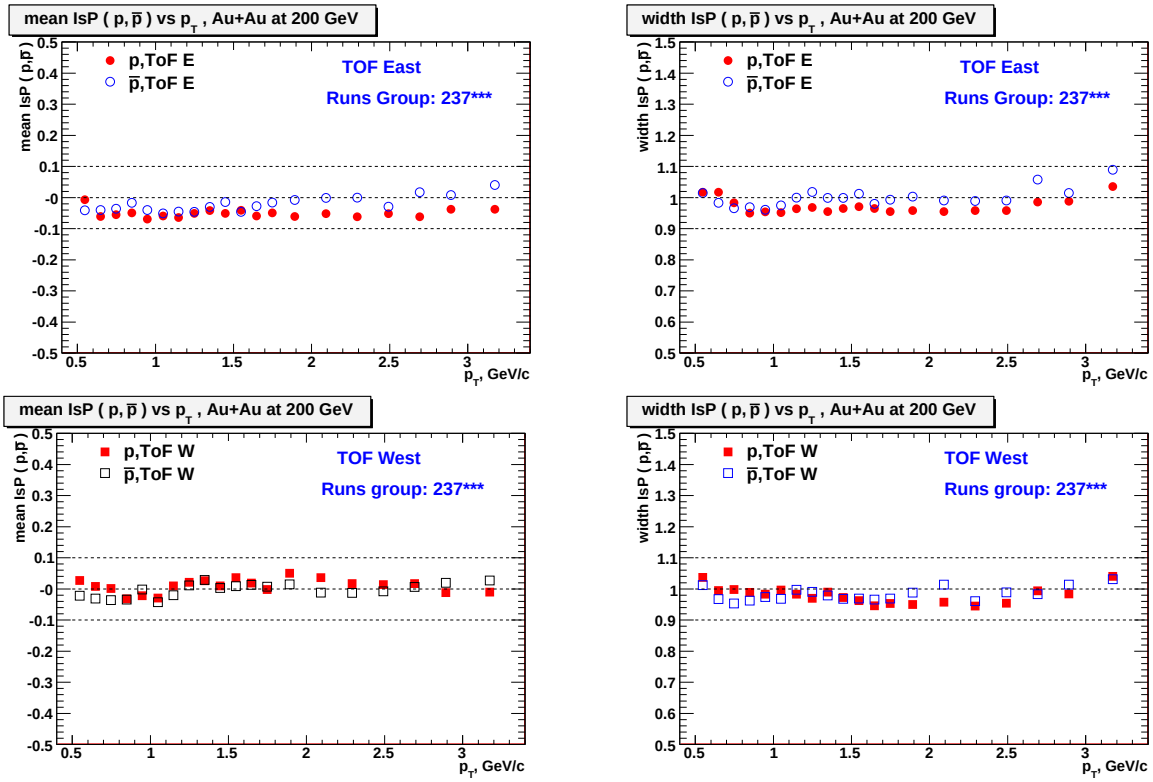


Figure 76: Mean/Sigma of IsProton as a function of p_T

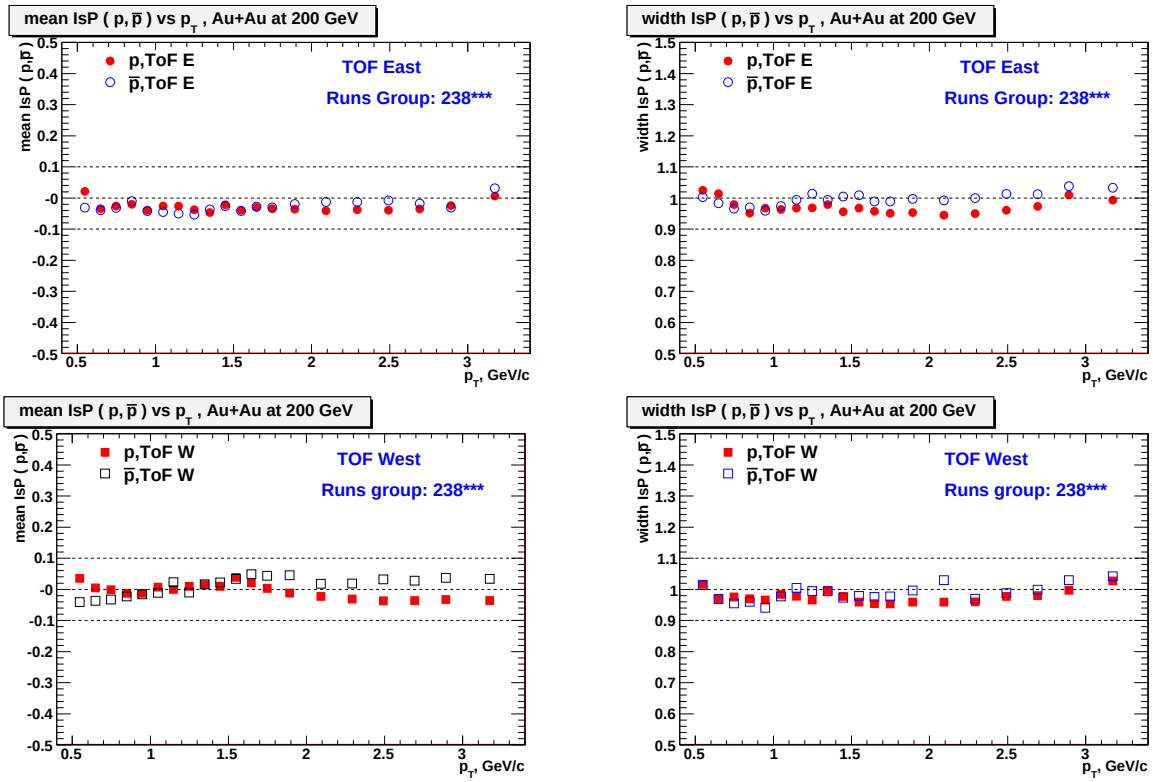


Figure 77: Mean/Sigma of IsProton as a function of p_T

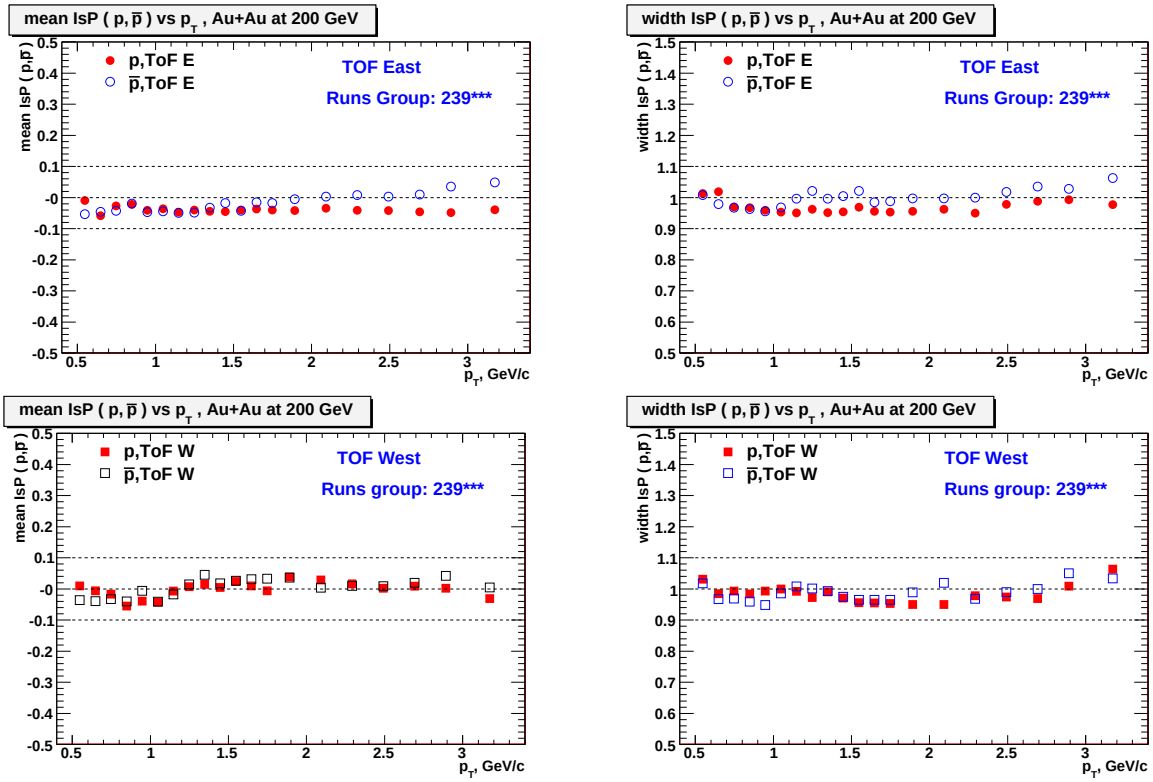


Figure 78: Mean/Sigma of IsProton as a function of p_T

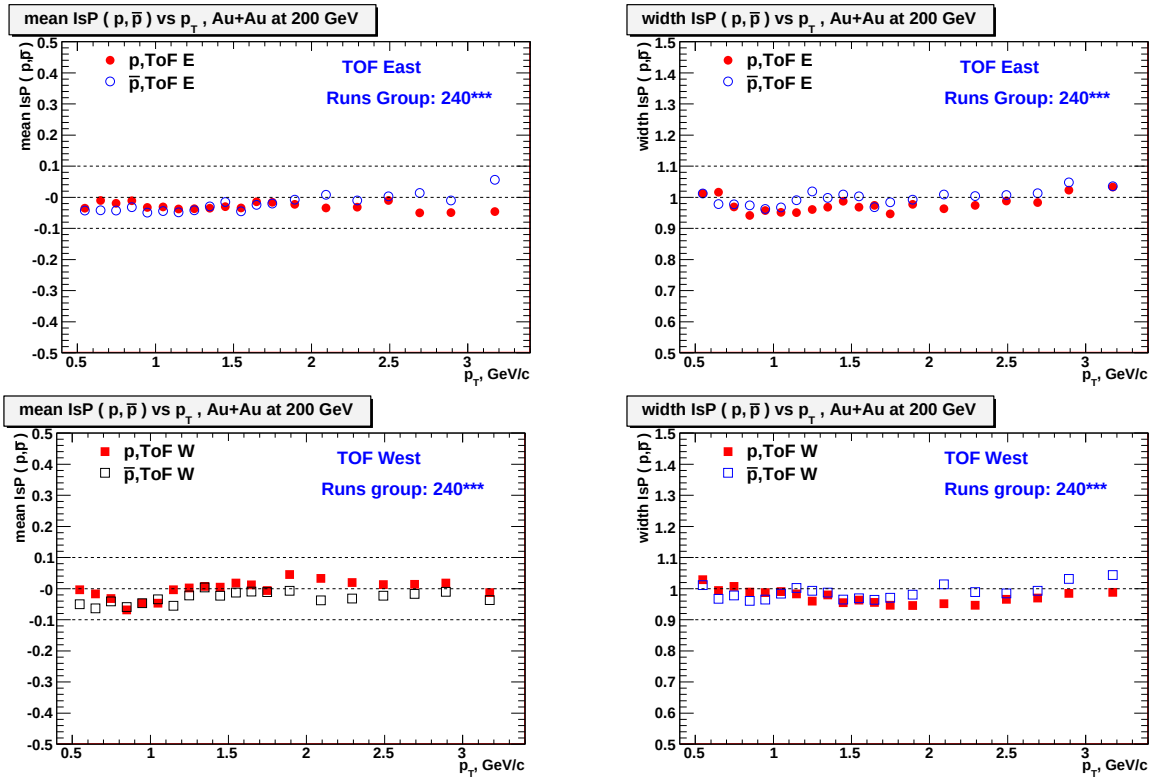


Figure 79: Mean/Sigma of IsProton as a function of p_T